Design and Development of a Mobile Climbing Robot for Wind Turbine Inspection

Anwar Magdy Mohamed Zaky Sahbel

https://orcid.org/0000-0001-7669-9549

A thesis submitted in partial fulfilment of the
requirements of London South Bank University
for the degree of Doctor of Philosophy by Publication

October 2019

Abstract

Wind turbines (WT) have become an essential renewable energy source as the contribution of WT farms has reached megawatts scale. However, wind turbine blades (WTB) are subjected to failure due to many loading effects such as aerodynamic, gravity and centrifugal loads and operation in harsh environments such as ultraviolet (UV) radiation, ice, hail, temperature variation, dirt, and salt. As a result, the blades suffer different types of damage. Consequently, a periodic inspection process is required to detect and repair defects before a catastrophic failure happens.

This thesis presents a literature review of wall climbing robots to identify the most appropriate locomotion and adhesion method to use for a WT climbing machine that can take a large payload of non-destructive testing (NDT) sensors up to a blade and deploy them with scanning arms. A review of wind turbine blade construction, various loading effects on blades and types of damage in blades is followed by a review of the NDT techniques used for inspecting WTB.

The above review determines the design requirements to achieve the aim of the current research which is to design a low-cost and reliable mobile robot which will be able to climb the WT tower and subsequently scan the blade surface to perform the inspection using various sensors to identify and classify damages. This robot system should be able to access all the critical areas of the blade structure in a stable and secure way. It should be stable enough to allow the various test sensors to scan the blade structure in the shortest possible time.

The thesis describes the development of a tower climbing robot that uses magnetic adhesion to adhere to the WT. As a preliminary study, a simulation model is developed using COMSOL Multiphysics to simulate the magnetic adhesion force while climbing the tower. A test rig is designed and fabricated to measure the magnetic adhesion force experimentally to validate the simulation model. The response surface methodology (RSM) using Box-Behnken design (BBD) is used to design and perform experiments to optimise different independent variables i.e. air gap, the distance between magnets in an array and backplate (yoke) thickness that affect the magnetic adhesion force.

A scaled-down prototype magnetic adhesion climbing robot has been designed and constructed for wind turbine blade inspection. The robot is 0.29 m long with two 1.0 m long arms, weighs 10.0 kg and can carry a maximum 2.0 kg payload of NDT sensors. Optimum design of a magnetic adhesion mechanism has been developed for the climbing robot prototype that

maximises the magnetic adhesion force. The robot is equipped with two arms that can be extended by one meter to come close to the blade for inspection. Each arm is equipped with a gripper that can hold an inspection tool of weight up to one kilogram. A scaled-down wind turbine has been modelled using SolidWorks and a portion of it constructed to experimentally test the scaled-down climbing robot.

To scale up the robot prototype for operation on a normal sized wind turbine, a 100 m tall wind turbine with three 76 m long blades has been modelled and the prototype robot scaled up based on these dimensions. The scaled-up robot is 3.0 m long, weighs 1135 kg and has two 10 m long arms. Static stress analysis and flow simulation have been carried out to check the durability of the scaled-up robot while climbing the wind turbine tower.

The procedure for scaling up the adhesion mechanism to achieve equilibrium of the robot has been introduced based on the reaction force concluded from the static stress and flow simulation study. As a result, the maximum payload that each arm can carry has been calculated for both the scaled-down prototype (1 kg) and the scaled-up design (50 kg). This concludes the utility and robustness of the wall climbing robot as a robotic solution for wind turbine blade inspection.

Acknowledgement

Table of Contents

List of Figures

List of Tables

List of Abbreviations

AE	Acoustic Emission
ANOVA	Analysis of Variance
BBD	Box-Behnken Design
CSP	Concentrating Solar Power
CT	Computed Tomography
DC	Direct Current
DOF	Degree of Freedom
GFRP	Glass Fibre Reinforced Plastics
GRP	Glass Reinforced Plastic
NDT	Non-Destructive Testing
RSM	Response Surface Methodology
UV	Ultraviolet
WT	Wind Turbine
WTB	Wind Turbine Blades

Chapter 1

Introduction

1.1. Introduction

This chapter introduces the energy demand and consumption problem. These problems are behind the escalating attention to the use of renewable energy resources for power generation. Wind energy resources are introduced taking into consideration the problem facing wind turbines such as blade failures. It also discusses the inspection concept of a wind turbine blade by using a robot. An overview of robot design regarding the locomotion and adhesion principle is demonstrated. Finally, the motivation for this work, aim, objectives, contributions to knowledge and the thesis outline are presented.

1.2. Energy demand

The global energy consumption has tremendously increased in recent times due to the rapid increase in population and enhanced modern living standards. According to statistics in 2016, it is expected that the world population will increase by 1 billion during the next ten years. It is worth mentioning that the world population in 2016 was 7.4 billion and it is expected to reach 9.6 billion by 2050 [1]. Not only are the developed countries depleting an enormous amount of energy but also the consumption of the developing countries is increasing. Energy services are critical in achieving sustainability that is economic, social, and environmental aspects. The energy consumption is expected to rise by 50% between 2005 and 2030 with most of the consumption coming from developing countries [2]. Global energy demand rose by 2.1% in 2017 compared with 0.9% in 2016 and was 0.9% on average over the past five years. Global energy-related CO_2 emissions increased by 1.4% in 2017, reaching a massive high of 32.5 gigatons (GT), a resumption of growth after three years of global emissions being constant [3]. However, energy consumption and greenhouse gases (GHG) emissions became a global issue. Accordingly, these aforementioned issues are urgent reasons for substantial attention and focus on the usage of renewable energy sources and the adoption of renewable energy technology.

1.3.   Renewable energy resources

1.3.1.   Biomass energy

All organic materials evolving from plants, trees and crops, together with the collection and storage of the sun's energy through photosynthesis are referred to by the term "Biomass". "Biomass energy" is the transformation of biomass into useful energy such as heat, electricity and as liquid fuels [4].

1.3.2.   Hydropower energy

Hydropower is developed from the energy of flowing water. Flowing water generates energy that can be captured and transformed into the form of electricity supply by using turbines. The most common form of hydropower is generated from dams, although newer forms harnessing wave and tidal power are becoming more widespread. Hydropower is generated from water flowing in the hydrological cycle which is affected by solar radiation. It is the water flow in rivers (affected by the gravity force) to flow from higher to lower elevations that can be used to generate hydropower [5].

1.3.3.   Solar energy

The generation of solar energy includes the utilisation of the sun's energy to supply hot water through solar thermal systems or electricity via solar photovoltaic (PV) and concentrating solar power (CSP) systems [6].

1.3.4.   Photovoltaic

Solar photovoltaic (PV) systems directly transform solar energy into electrical energy. The basic building block of a PV system is the PV cell which is a semiconductor device that transforms solar energy into direct electric current. PV cells are linked together to form a PV module. The PV modules merged with a set of additional application-dependent system components (e.g., inverters, batteries, electrical components, and mounting systems), form a PV system. PV systems are highly modular, i.e., modules can be interconnected together to provide power ranging from a few watts to tens of megawatts [7].

1.3.5.   Concentrating solar power

Concentrating solar power (CSP) technologies generate electricity by focusing direct beam

solar irradiance to heat a liquid, solid or gas that is then utilised in a downstream process for generation of electricity. Large-scale CSP plants most commonly focus sunlight by reflection, as opposed to refraction with lenses [8].

1.4. Wind energy

Wind power is defined as the transformation of wind energy by wind turbines into a useful form such as utilising wind turbines to generate electricity. The wind turbines for electricity generation were first developed at the beginning of the 20th century. This technology has gradually improved since the early of the 1970s. Wind energy has been labelled as the most leading sustainable energy resource by the end of the 1990s [9].

Generating electricity from wind energy needs the kinetic energy of moving air to be transformed into mechanical and then electrical energy, thus challenging the industry to design cost-effective wind turbines and power plants to carry out this transformation. The amount of kinetic energy in the wind that is theoretically available for extraction increases with the cube of the wind speed. However, a turbine is able to capture only a small portion of that available energy, so wind turbine design has focused on increasing energy capture over the range of wind speeds experienced by wind turbines while aiming to reduce the cost of wind energy taking all parameters into consideration. For the sake of cost reduction, wind turbine design is also driven by a willingness to minimise materials usage while continuing to maximise turbine size, maximise the reliability of components and systems, and enhance the operation of wind power plants.

1.4.1. Wind turbine types

There are two types of wind turbines: horizontal axis wind turbine (HAWT) and vertical axis wind turbine (VAWT). The axis of VAWT is perpendicular to the ground while the axis of HAWT is parallel to the ground and it includes more components to control the blade direction such as yaw and pitch mechanisms. There are two types of HAWT: the onshore and offshore types. Both types have the same components, which are the rotor (blade), gearbox and generator. The difference between these types is that the offshore wind turbine is much bigger than the onshore wind turbine which gives it the ability to generate more power especially with the high quality of wind available in the sea.

In spite of the increasing number of installed wind power plants in the world [10, 11], their reliability and sustainability are not guaranteed. There are a set of factors that affect the efficiency and performance of wind turbine blades (WTB) such as UV radiation, ice, hail, temperature variation, stress and fatigue in components, impact damages, dirt and salt [10] in addition to the flaws that might arise during manufacturing. All these factors might reduce the operating performance or lead to failure of a WTB.

To avoid WTB failure, the blades should be inspected regularly. However, the maintenance and inspection of wind blades are difficult especially for large blades and offshore WTs as it is costly to access the blades and needs skilled workers [12].

1.4.2. Inspection hazards and methods

The offshore wind industry has been tremendously developed over the last years. The turbines have become bigger [13]. The tools needed to install them also have become bigger and more complex which puts higher stress on the technicians and makes the inspection process more complicated. Also, it is very crucial to keep the turbines running and generating power as efficiently as possible. The requirements of inspection, such as higher skills, higher competencies, plus the time pressure and cost of the inspection, makes it critical to have highly qualified technicians with high skills and the right mind-set. The skilled workers should have necessary training to access the blade utilising ropes hanged from the nacelle or using cranes. Figure 1.1 illustrates the manual inspection process. Throughout the inspection, the wind speed must not exceed 12 m/s while the blade is locked in a vertical position parallel to the wind turbine tower. As the blade is locked in a static position, there is still a flap-wise and edgewise vibration especially for large blades which leads to more challenges for the worker as it unsettles the rope and increases the probability of crane collapse. All these hazards are the reasons that drive researchers to find rigorous solutions for wind turbine blade inspection.

Figure 1.1 Skilled worker climbing a wind turbine blade using ropes hung from the nacelle to inspect the leading and the trailing blade edge [14].

Many researchers have developed robotic solutions to inspect wind turbine blades. These robots do not look like the human in manifestation or even perform in a humanlike manner; however, they are inspired by nature. These types of robots are named "service robots". The service robots have more degree of freedom than industrial robots which provide them with the opportunity of overcoming any environmental changes. One of these types is the "climbing robot" which can efficiently climb three-dimensional constructions [15]. A survey of climbing robots is carried out in chapter 2.

1.5.   Potential and motivation for climbing robots

The increased risks, additional costs, and extended inspection time required for manual inspection could be reduced at an early stage if a robotic solution is recognised. A climbing robot could inspect the internal and external surface of the wind turbine blade without the usage of ropes and/or cranes. The risk of interfering with power lines could be reduced by eliminating the use of booms, climbers or rigging. The entire blade could be inspected efficiently, and the coordinates of the failure parts could be labelled with climbing robots. The data gathered from the inspection could be kept for any future inspection comparisons. Due to the constraints in the existing methods of inspection and maintenance, industrial stakeholders have realised the criticality of utilising robots to improve the inspection process. With the ability to overcome obstacles and climb surfaces irrespective of orientation, many benefits can be noticed with a

climbing robot, such as access to inspection sites previously inaccessible to humans, thereby reducing and removing the risk for workers. A mobile robotic solution will allow the usage of multiple non-destructive testing techniques, such as visual, hyper-spectral, electromagnetic, ultrasonic, and laser. These will provide a condition assessment of the structure by storing detailed records with organised inspection data detailing location and condition. Repairs can be carried out at the time of inspection. Regular, efficient and on-going inspection and maintenance can be carried out with minimal effort using coordinated teams of climbing robots.

1.6. Challenges faced in developing climbing robots

While the benefits of introducing robots into the inspection industry are widely noticed [16, 17], the practical adoption of robots has been largely limited to industrial users in very structured environments. In these structured environments, robots have little to no requirement of mobility as work is delivered to the robots. Industrial robots with mobility are restricted to operate within structured and sanctioned work zones with very few errors. These environments are carefully designed to maintain reliable, robust, and safe operations. The biggest challenge encountered by robots and their utilisation in real-world scenarios is related to their operating environment. The environment has a great effect on all aspects related to the robot including design, required intelligence, and operation. The successful utilisation of state-of-the-art climbing robots today is largely limited for operation in simple and semi-structured environments. These environments include large flat planar surfaces, ideal surface conditions, with simple and known barriers. These environments require simple mobility and little to no autonomy. Robots in these scenarios can be controlled by human operators with simple controllers.

On the other hand, real-world infrastructure includes complex structural geometry, surface irregularities, and unforeseen obstacles. This presents two challenges for the designers of such climbing robots; these being the requirement for an advanced robot intelligence and the requirement for advanced robot designs which can deal with the environment and achieve operational goals.

1.7. Robot intelligence

Climbing robots need a sense of environmental and situational awareness in order to overcome challenges and to eliminate uncertainties. This needs sensory information which must be

interpreted and acted upon in an accurate and timely manner. Therefore, these robots are expected to have advanced intelligence via sophisticated algorithms to tackle the challenges of autonomy. The fundamental principles for autonomous operation include exploration, mapping, localisation, planning, motion control, and task execution. This thesis does not focus on the fundamental research for these aspects of intelligence. Instead, it focuses on the design of the robot that provides access to remote structures and permits operation in real-world situations.

1.8.   Robot design

Assuming high-level autonomy is achieved; robots are also limited by constraints of their design. There are several aspects of the design which require crucial consideration; these are the task definition, locomotion and adhesion [18]. These aspects have a central role in the design of climbing robots, requiring careful consideration and selection to enable practical utilisation.

1.8.1.   The task definition

The identification of task definition is the first step in the design process. This states the scope and mission of the climbing robot, including the procedures which must be considered, the required application scenarios and environmental influences. This specifies the required payload capacity and equipment which must be integrated into the design process. The task definition greatly impacts the design of the locomotion and adhesion principles.

1.8.2.   Locomotion

Climbing robots need means of moving from one location to another, this is referred to as locomotion. Locomotion plays an important role in the mobility, dexterity, and manoeuvrability of a climbing robot in order to perform its task definition. Climbing robots may adopt locomotion such as wheeled, tanked, legged, limbless or rolling. Each type of locomotion has various forms of implementations with advantages and disadvantages defined by the task definition.

1.8.3.   Mobility

The mobility of a robot is a performance criterion which defines the effectiveness of the climbing robot in moving from one location to another. The implementation of locomotion can

result in greater mobility for a specific task, application scenario or environmental conditions. Accordingly, as the complexity of the task definition increases, the design of a climbing robot becomes increasingly more challenging.

1.8.4. Adhesion

The adhesion method is another challenging aspect of designing a climbing robot. There are many principles of adhesion, each largely dependent on the task definition, the intended operating environment and surface conditions. Adhesion mechanisms may embrace principles such as chemical, electrostatic, Van Der Waals, pneumatic, grasping, electromagnets or permanent magnets. Each method comes with advantages and disadvantages that are different for specific environmental conditions and operational goals.

1.9. Research context and background

A literature search has been carried out to discover existing or proposed robots to inspect WTs. A prototype robot for climbing the WT tower [19] has an irregular hexagon shape with three wheels on three sides. Each wheel is equipped with two motors one for the motion and the other for steering. The robot can climb the tower; however, it should be disassembled to be placed around the WT tower and be assembled again to attach it to the tower. There are many other types of robots for inspecting rotor blades [20-22]. However, all these robots are driven by ropes or wires which need pre-installation. The Micro Aerial Vehicle (MAV) [23] is a development which can fly by using four rotors and attaches itself to the blades of the WT to perform a macro inspection with a camera or thermographic camera. However, the power consumption of the four motors increases the discharging time of the batteries giving short operation and inspection times. There is an identified gap in the reported developments for a reliable system that can access wind blades quickly, carry power for long inspection times, reliably acquire NDT signals and data, control and communicate with the blade inspection robot and ground-based controllers via an umbilical cable.

1.10. Research aim and objectives

The aim of the proposed research is to develop a small mobile robot that can climb the WT tower carrying non-destructive sensors, reach across the blade for inspection. In addition to that, it should be easy to be transported to and deployed on a WT tower to reduce the time and cost of the inspection.

The objectives of the proposed study are:

- Review various nondestructive techniques used for inspecting WTBs to find suitable sensor regarding the size and weight so the climbing robot can hold it
- Review different types of wall climbing robots
- Develop a model of the WT components
- Simulate and optimise the magnetic adhesion force for WT tower climbing robot
- Design and build a WT wall climbing robot equipped with suitable sensors
- Experimentally test to evaluate the mobility effectiveness of the prototype design.

1.11. Research methodology

The SolidWorks software has been used to develop a wind turbine model where the initial design parameters have been captured from the literature. In order to check the utility of a scaled up climbing robot designed for real inspection, a wind turbine has been modelled. A configuration of permanent magnets has been selected to adhere the climbing robot to the steel tower of a WT. A finite element method (FEM) model using COMSOL Multiphysics software has been created to investigate the optimisation of adhesion forces generated by permanent magnets by studying the impact of the air gap, the distance between magnets and backplate (yoke) on the magnetic adhesion force utilised for the wall climbing robot. Additionally, statistical software has been used for the magnetic adhesion force optimisation. Moreover, a test rig has been fabricated for the experimental measurement and validation of the magnetic adhesion force. The SolidWorks software has been used to design a scaled-down prototype robot for wind turbine blade inspection. The wheeled motion has been selected as the method of locomotion for the robot with high torque motors. The robot has been designed with two arms with two degrees of freedom to be capable of tracking the wind turbine blade aerofoil. Subsequently, the robot has been scaled up to adapt to the dimensions of a real wind turbine. In order to investigate the effect of the inspecting tool load as well as the wind speed, static and flow simulations have been performed.

1.12. Contributions

The outcomes of the research presented in this thesis are the result of an extensive literature review, theoretical modelling, design optimisations, experimental results, testing and a reflection of research conducted. The work in this thesis has been conducted to seek a robust and durable robotic solution for wind turbine inspection.

The main contributions of the research presented in this thesis are:

- The response surface methodology (RSM) has been used to design experiments for the optimum magnetic adhesion force and to investigate the effect of independent variables such as distance between magnets, magnet/surface air gap and yoke thickness. A quadratic polynomial model has been obtained for the response variable function in all independent variables. Optimum conditions have been concluded from the quadratic polynomial model for the adhesion force. Experimental and statistical validation has been applied for the predicted model resulting in a high agreement between response values. The average relative error between the tested experimental values and predicted values using the quadratic polynomial model is 0.95%. This has been reported in a journal paper and chapter 3 in this thesis.

- A finite element method has been carried out to study the effect of the parameters affecting the magnetic adhesion force. Finally, a prototype climbing robot has been developed by employing the extracted design parameters from the quadratic polynomial model. This has been reported in a journal paper and chapter 3 in this thesis.

- A novel climbing robot has been developed equipped with two 2 DOF arms for wind turbine blade inspection. The climbing robot can climb on the wind turbine tower surface and extend its arms to perform the inspection of the blade. The superior mobility of the arms allows the climbing robot to follow the blade profile and carry out NDT inspection. This has been reported in a conference paper and chapter 4 in this thesis.

- The prototype robot has been developed to test the feasibility of carrying long deployment arms and inspection sensors to wind turbine blades. The study aimed to optimise the payload carrying capability of the robot by using permanent magnet adhesion to attach to the WT tower. This has been reported in a conference paper and chapter 4 in this thesis.

- A scaling-up study has been presented for the prototype robot to match a real medium-size wind turbine. The scaled-up robot arms can be extended to reach 10 meters and the robot weight is 1135 kg. The study has shown that the robot can carry a maximum payload of 50 kg inspection sensor on each arm. This has been reported in chapter 5 in this thesis.

All the major contributions of this research have been reported in the publications listed below:

Journal paper:

Anwar Sahbel, Ayman Abbas, and Tariq Sattar, "Experimental and Numerical Optimization of Magnetic Adhesion Force for Wall Climbing Robot Applications," International Journal of Mechanical Engineering and Robotics Research, Vol. 8, No. 1, pp. 18-24, January 2019. DOI: 10.18178/ijmerr.8.1.18-24

Conference paper:

A. Sahbel, A. Abbas and T. Sattar, "System Design and Implementation of Wall Climbing Robot for Wind Turbine Blade Inspection," 2019 International Conference on Innovative Trends in Computer Engineering (ITCE), Aswan, Egypt, 2019, pp. 242-247. DOI: 10.1109/ITCE.2019.8646326

1.13. Thesis outline

This thesis consists of six chapters including the introduction in this chapter. The remainder layout of the thesis is as follows:

In chapter two, a literature review summarises the research work performed on wall climbing robots based on the locomotion and adhesion principle after that research gap in the current climbing robots. The chapter also presents the pros and cons for currently developed robots for inspecting the wind turbine blade including funded projects at London South Bank University. Moreover, the different varying loads and harsh environment that affects the performance of the blade are presented followed by nondestructive techniques used to inspect WTB.

Chapter three presents modelling, simulation and optimisation of the magnetic adhesion force for wall climbing robot by focusing magnetic flux using a suitable configuration of iron yokes and rare earth permanent magnets. COMSOL Multiphysics has been performed to study different parameters affecting the magnetic adhesion force. A finite element analysis is performed to find an optimum design of a magnetic adhesion mechanism for ferrous surfaces. Experiments have been designed using the response surface methodology (RSM) to study the effect of identified independent parameters (namely the distance between magnets, air gap and yoke thickness) that affect the response variable i.e. the magnetic adhesion force. A quadratic regression model has been developed to represent an empirical relationship between the

response variable and the independent variables. A test rig has been developed for the experimental measurements of the magnetic adhesion force.

Chapter four describes the developmental stages of a prototype climbing robot for WTB inspection. Also, a design for a prototype WT has been presented for the testing of the climbing robot. Moreover, a static force analysis on the climbing robot is introduced.

Chapter five presents the procedure of scaling up the prototype climbing robot based on a real wind turbine model. A static and flow simulation study has been presented to test the durability of the climbing robot during the inspection. A scaling up of the magnetic adhesion system is presented for the scaled-up robot.

Chapter six concludes this thesis with a summary of key features achieved in this research. This chapter also formulates conclusions and recommendations for future work advance this research.

1.14. Chapter summary

This chapter has summarised the problem of energy demand and the role of renewable energy sources. It has demonstrated the hazards of wind turbine blade inspection and the advantages of developing robotic solutions to mitigate these hazards. Also, it has introduced the challenges in designing a climbing robot that can move up a wind turbine tower and deploy NDT sensors on a wind turbine blade. Furthermore, this chapter has highlighted the limitation of the currently developed robots in inspecting the wind turbine blades which leads to the motivation of this research. In addition, the aim, objectives and the thesis outline have been presented. Finally, this chapter has elaborated the contributions to knowledge as well as a defined scope of this thesis.

Chapter 2

Literature review

2.1. Introduction

This chapter introduces a literature review of the locomotion and adhesion principles for wall climbing robot to find an appropriate solution for inspecting wind turbine blades. This robot should use adequate adhesion force to adhere to the tower without consuming power and maintain the high payload of NDT equipment. Moreover, the gap in current climbing robots research has been identified. Furthermore, the impact of the environmental conditions on the wind turbine blade performance has been demonstrated. Then is followed by a review of the nondestructive techniques for inspecting WTBs.

2.2. Classification of wall climbing robot

The climbing robots are classified according to their locomotion types and adhesion principles. The types of locomotion and adhesion are chosen according to the application.

2.2.1. Locomotion

The movement of the robot from one place to another is named as locomotion. Locomotion is classified into four types: arms and legs, wheels, sliding frame, wires and rails.

2.2.1.1. Arms and legs

Arms and legs are well-known methods for robot locomotion that have been developed over the past two decades. A hexapod REST wall climbing robot using SCARA leg type was developed by [24] as shown in Figure 2.1 (a). The leg was built from three links with three degrees of freedom (two revolute and one prismatic) so that the robot centre of gravity can be close to the surface to avoid overturning at an obstacle. A ball joint at the end of the leg was attached to the feet which gave the feet rotation flexibility of 30º around the Z-axis. The robot used permanent magnets attached to the feet so the robot can climb ferromagnetic structures. Electromagnets were used to generate a force against the permanent magnets to release the feet during motion or in the same direction to enhance the adhesion force during an emergency. The advantage of this design was the ability to carry a high payload. However, it consumes high power to activate the electromagnet to detach the leg during motion. A robot with two

13

suction feet was developed [25], shown in Figure 2.1 (b), to have the ability to make plane transitions. Each foot has many suction cups that work with the vibration suction method. This robot could not carry a high payload and the suction cups need a smooth surface to attach reliably. The author in [26] presents a wall climbing robot with four legs capable of climbing vertical rough surface with claws attached to each leg as shown in Figure 2.1 (c).

(a) REST [24]
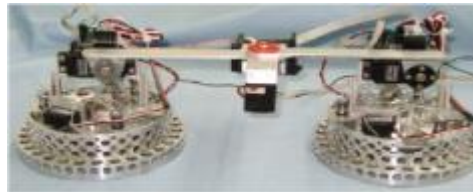
(b) Vibration Suction Foot [25]

(c) Claws robot [26]

Figure 2.1 Climbing robots using legs for locomotion.

2.2.1.2. Wheels

Wheels are a locomotion type that provides the robots with continuous and fast motion on any surface. A wall climbing robot was developed, see Figure 2.2 (a), with a magnetic wheel for inspecting an oil tank [27]. It uses a different type of wheel which provides the motion and the adhesion force at the same time. The wheel is constructed of four parts, with two steel rings at both sides of the wheel, and a middle nylon ring with twelve cylindrical holes around the circumference holding the magnets. An inspecting mobile robot was developed [28], see Figure 2.2 (b), with Omni wheels and a chassis which has the ability to adapt to any structure surface with high manoeuvrability. Another robot was developed that combines two types of locomotion arms and wheels [29]. Arms were used to make the plane transition as shown in Figure 2.2 (c).
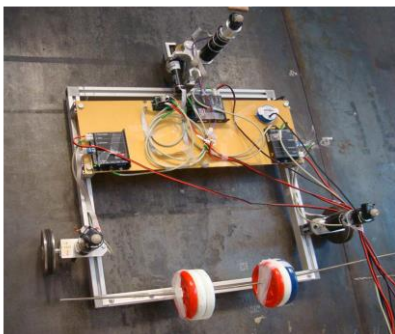
(a) Robot for tank Inspection [27]
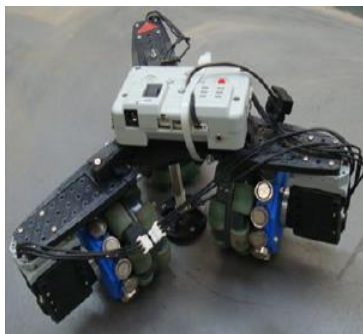
(b) Omni-climber robot [28]
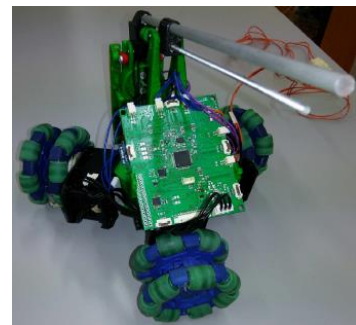
(c)Wheel based climbing, arm based plane transition [29]

Figure 2.2 Climbing robots using wheels for locomotion

2.2.1.3. Sliding frame

These types of robots are mainly used for glass cleaning. The robots consist of two frames that slide over each other. Several fulcrums are linked to each frame and suction cups. While one of the frames is attached to the surface, the second is lifted and slides over the first so that the robot can move in the horizontal and vertical directions [30-32], see Figure 2.3.
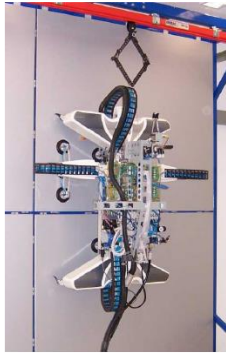
(a) Sky cleaner IV [30]
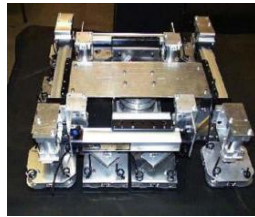
(b) Robot by [31]

(c) Robot by [32]

Figure 2.3 Climbing robots using sliding frames for locomotion

2.2.1.4. Wires and rails

Wires and rails are usually used for a permanent climbing application such as inspection of specific parts in a WT. A telerobot prototype was designed to remotely inspect the offshore WT components inside the nacelle [33], see Figure 2.4 (a). The telerobot moves on a rail consisting of two aluminium pipes and the electricity is supplied through the rails. The other two robots are used for cleaning the glass facades of high building [34] and an airport control tower [35] shown in Figure 2.4 (b, c). The robots are connected to wires or cables with a conveyor which is used for positioning the robot in the area need to be cleaned. Also, the cables are used for supplying the robot with power.
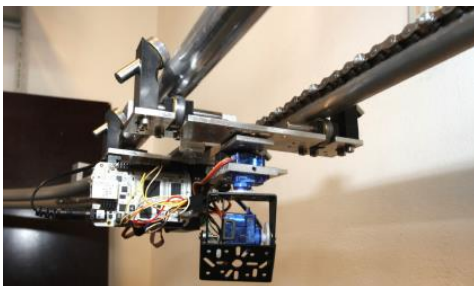
(a) Telerobot [33]

(b) Robot SIRIUSc [34]
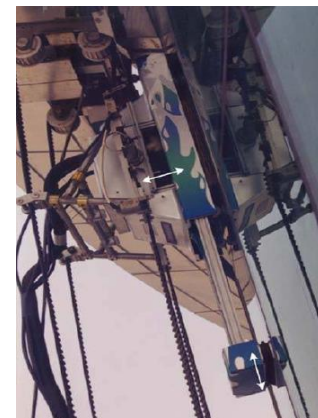
(c) Cleaning robot [35]

Figure 2.4 Climbing robots using wires and rails for locomotion

2.2.1.5. Comparison of locomotion techniques

A comparison of different locomotion types is illustrated in Table 2.1 showing the advantage and disadvantage of each type.

Table 2.1 Comparison between different locomotion techniques

Locomotion	Advantage	Disadvantage
Arms and legs	The ability to avoid obstacles while climbing.	Very slow as the robot moves only one leg at a time to maintain its balance.
Wheels	Fast and provide continuous motion.	Slippage on a smooth surface and cannot easily transfer from one plane to another. Also, wheels cannot move on discontinuous ground.
Sliding frame	During motion, it can check the availability of the surface before it lifts the other frames.	It is large with very slow motion since it is not continuous like wheels.
Wires and rails	Does not need adhesion force for holding the robot.	The construction of specific rail is costly, and the robot function will be limited to a certain task.

2.2.2. Adhesion principle

The adhesion force method is defined according to the material and roughness of the surface and the robot weight plus the payload. The adhesion principle is classified into five main types: pneumatic, mechanical, electrostatic, chemical and magnetic adhesion.

2.2.2.1. Pneumatic adhesion

Pneumatic adhesion is the most widely used technique for wall climbing robots. It is divided into two main types which are suction cups and vortex (or negative pressure thrust). The suction cups are classified as active and passive suction cups.

A. Passive suction cup

These suction cups are used without energy supply to attach to the surface. In [36] a legged wall climbing robot was developed using passive suction cups. The robot consists of six legs. Each leg is equipped with a suction cup connected to a four-bar mechanism to attach and detach from the wall. The robot motion is very slow as it uses legs for locomotion, and it cannot climb on rough surfaces as the suction cups work only on a smooth surface. Since the suction cups become widely used, a lot of analysis of the adhesion force of suction cups has been done over the last two decades [37, 38]. Moreover, there is a new method that utilises the vibrating suction method found in the literature in [25, 39].
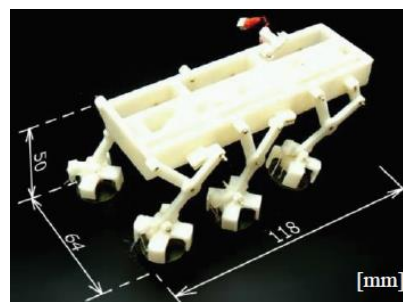
Figure 2.5 Small legged wall climbing robot [36]

B. Active suction cups and vacuum chamber

Active suction cups with a vacuum chamber requires a valve and a vacuum pump for attachment and detachment. A multi-track robot was developed in [40] as shown in Figure 2.6 (a) that can climb any wall regardless of the material of the surface. The robot has the ability to make plane transitions while carrying a high payload. The robot is composed of five modules. Each module is in the form of three parts connected with two links. Each module is equipped with caterpillar tracks with six suction cups that can be stuck and removed from the wall automatically. The robot has the advantage of climbing any surface. However, the design and control are very complex. Another robot which is based on two orthogonal shafts, like the motion of sliding frames, use suction cups [41] as illustrated in Figure 2.6 (b). The work in [42], shown in Figure 2.6 (c), presents a wall climbing robot with eight suction cups that are used for nondestructive inspection. The robot is the incorporation of two parts with each part having four suction cups. The internal part is responsible for linear motion and rotation while the external supports the robot when the internal part is adjusting its position. The author in [43] presents the Alicia prototype shown in Figure 2.6 (d) that works with the vacuum chamber principle. The main advantage of the vacuum chamber is that the robot can remain attached to the wall while moving. The author demonstrates two prototypes. The first has problems related

to the sealing and payload while these problems were solved in the second prototype. Three modules of the second prototype are connected by two links of pneumatic cylinders so that the robot can avoid obstacle up to 1 cm height. The robot can be held by two modules while rising the third to overcome the obstacle.

| (a) Multi-Track climbing robot [40] | (b) Robot by [41] | (c) SURFY robot [42] | (d) ALICIA robot [43] |
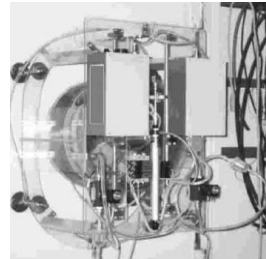
Figure 2.6 Climbing robots using active suction cups and vacuum chamber

C. Vortex or negative pressure thrust

The vortex is generated by a high-speed impeller resulting in negative pressure in the centre of the cup. This negative pressure produces adhesion force without the need for direct contact with the wall. In [44], a series of robots called LARVA I and LARVA II are reported. The differences between the two robots are the centre of gravity, weight and size. Both use impellers and two wheels for locomotion.
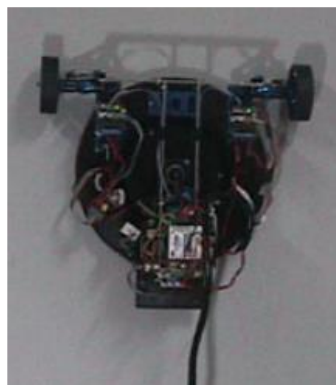
Figure 2.7 LARVA robot [44]

2.2.2.2. Mechanical

The mechanical adhesion method uses clamping mechanisms or claws for gripping. These methods are mainly utilised with surfaces which are rough so that the robot can find points for attachment. A quadrupedal robot in [45] called RiSE V3 was developed that is capable of climbing any cylindrical structure with complicated contour by using claws. Another robot described in [46] was able to climb cylindrical structures with different diameters but by using grippers. The robot can cope with sharp edges, T-junctions and flanges by detaching the gripper

from the surface and passing the obstacle. Alternatively, in [47], a climbing robot consists of two links where a dactyl claw is connected to the main link and the other link is tail engaged to the first with gears. The tail is equipped with batteries for supplying power to the robot and to act as a balancing weight. The locomotion principle is achieved when the tail and the batteries oscillate like a pendulum to let the robot climb a wall.

2.2.2.3. Electrostatic

This adhesion method is based on the electrostatic force between a surface, which acts as the substrate material, and electro-adhesive pads that consist of conductive electrodes. This adhesion principle is applied to wheeled or tracked robots in the literature. The work in [48] presents a wall climbing robot consisting of dual-tracks utilising electrostatic adhesion. The electrostatic adhesion force is generated by an electrode panel which is comprised of two parts with different potentials. The electrode panels are also used in a locomotion mechanism where the electrodes are installed on the front and back scrolls. The electrodes are covered by silicon rubber to enhance the friction with the scrolls. Two DC motors are engaged to the back scrolls to drive the robot while the front scrolls are free and connected to the back scrolls with carbon fibre. The electrode panels are connected to the power supply through two electric rings to keep them supplied with electricity during rotation. Furthermore, to avoid the overturning moment there are two tails joined to the end of the robot. The robot is controlled by remote control and a radio receiver based on the robot.

A quadruped wall climbing robot is introduced in [49]. Its motion is inspired by geckos. The adhesion principle is based on Van der Waals force between the surface and the robot. The robot locomotion is based on four legs. The front and back legs form two separated links attached to the centre body through a rotating joint, so the robot is like a four-bar mechanism. In addition to four links, a tail is utilised to avoid a peeling moment due to the centre of gravity offset. The robot is driven by three servo motors to provide the robot with motion. Two motors are connected to the front and rear links in the middle to swing the links during motion and one is responsible for waist motion during the rotation of robot.

2.2.2.4. Chemical adhesion

The authors in [50] have developed a wall climbing robot using a treadwheel made from flat sticky polymer. The robot can do three types of transition internally and externally. The robot

consists of two modules connected by passive directional compliant joints. Each module has V-10 sticky elastomer treads which provide the robot with the adhesion force.

2.2.2.5. Magnetic adhesion

Magnetic adhesion uses permanent magnets to adhere to ferrous metal surfaces. A wheeled robot has been developed [51] for inspecting long weld lines. The robot carries non-destructive equipment that weighs about 10 kg while at the same time maintaining a minimum air gap of 20 mm between the magnets and the climbing surface. Using a big magnet to achieve enough adhesion force will decrease the chance of carrying the required payload. As a result, a 1×4 neodymium grade N42 magnet array with different distances between the magnets is used. The adhesion force has been tested with and without a steel backplate and the result showed that steel a backplate drastically increases the attraction force.

A permanent magnet adhesion system has been designed for a wheeled wall climbing robot used for carrying a laser cutting system in [52]. The robot is required to carry the laser head which weighs about 12 kg in addition to the robot weight. Accordingly, five adhesion system configurations of neodymium N42 magnet have been considered to find the maximum adhesion force. Each magnet size was $50 \times 50 \times 12$ mm. Four configurations were constructed with the same air gap 25 mm and backplate dimension of $375 \times 50 \times 3$ mm. The fifth configuration used a backplate thickness of 15 mm instead of 3 mm. The first configuration was built using six magnets with a gap of 15 mm between each other. The second was created utilising three magnets with a gap between each magnet of 110 mm. The third arrangement was with four magnets, two in the middle of the yoke with a distance of 11 mm and two on each corner with a distance of 82 mm from the one in the middle. The fourth and fifth configurations were arranged with six magnets, two magnets were placed over each other with a distance of 110 mm between each other, but the difference is in the thickness of the backplate as mentioned above. The adhesion system was established with the last configuration as it shows the maximum adhesion force of 39.4 kg. Three yokes were positioned at a distance 30 mm from each other to give an overall adhesion force of 92 kg.

Magnetic adhesion has been used with other locomotion principles such as legs [24]. A magnetic attachment mechanism was proposed in [53] for a quadruped legged prototype robot. The design was based on many thin strips, forming the shape of a star with small circular

magnets, connected at the base of the leg by a locking nut and linear actuator working in the same direction as the peeling motion.

2.2.2.6. Comparison between adhesion principles

A comparison between different adhesion principles is illustrated in Table 2.2 showing the advantage and disadvantage of each type.

Table 2.2 Comparison between adhesion principles

Adhesion principle	Advantage	Disadvantage
Passive suction cup	Does not require energy supply or an actuator to stick to the surface. It has a strong adhesion force on smooth surfaces, and it can be easily removed by detaching the cup border.	Works only on a smooth surface.
Active suction cups and vacuum chamber	The robot can remain attached to the wall while moving. Can carry heavy payloads.	Require a compressed air supply and long supply ducts.
Vortex or negative pressure thrust	Produces adhesion force without the need for direct contact with the wall.	Can only carry small payloads of a few kilograms.
Mechanical	Utilised with rough surfaces and can stay in its place for a long time without energy supply and a low probability of falling.	Their motion is slow and cannot carry a high payload or climb smooth surfaces.
Electrostatic	The robot can climb any wall regardless of the material of the wall.	It has limited ability to cross obstacles and to carry a heavy payload.
Chemical adhesion	Can be attached to any surface.	Loss of adhesion force overtime due to dust.
Magnetic adhesion	Can be used with steel to provide an adhesion force without the need for energy supply and can carry a high payload.	It can be used only with ferrous surfaces.

2.3.   Gaps in the current climbing robots research

Many limitations have been highlighted in the literature review in both the locomotion mechanisms and the adhesion principles of climbing robots. Various robots have been developed with arms and legs as locomotion that provide flexibility in motion over uneven surfaces with high DOF. However, due to the high number of required joints to perform the complex motion, its control and mechanical design are difficult. In addition, low motion speeds make this technique not suitable for inspecting huge areas. Similarly, the sliding frames locomotion is not continuous due to the interchangeable motion between the two frames. Also, the system of sliding frames is usually large and allows only two DOF, so the mechanism has limited capability of manoeuvrability and plane transition.

Wire and rails are the simplest way of locomotion that requires a conveyor belt to be hanged from the top of the structure to be inspected to allow the robot movement. However, the robot can move only up and down without any ability to move sideways.

From the point of view of the adhesion principle, all types of pneumatic adhesion such as passive suction or active suction cups, vacuum chamber and vortex or negative pressure thrust were utilised in different applications and can achieve high adhesion force. However, a lot of components are required such as solenoid valves and regulating valves. Also, the higher the degree of freedom, the more components are required which reflects on the robot weight. In addition, if there is any leakage in the pneumatic system, failure of the climbing robot might happen.

Another adhesion principle which depends on mechanical mechanisms such as claws or gripping or clamping has been used in climbing robots. Most of the robots developed with this adhesion method use arms and legs as locomotion and are supported with claws for attachment [26, 45-47, 54-59]. Wheels have been used to grip the structure to be inspected [19, 60-63]. The robots that work with claws depend on the type of the surface to be climbed where it should be rough or with protrusions, so the robot can find attachment points for climbing. This can be considered as an advantage as the robot does not consume energy during climbing and even if the power is cut suddenly, the robot will not fall. However, these robots have limited capability of carrying heavy payload and their motion is slow.

An alternative adhesion method for wall climbing on different surfaces types uses the

electrostatic adhesion principle. This adhesion principle needs a very small amount of power [64]. However, it does not carry a high payload.

The chemical adhesion principle has been used with different locomotion techniques for wall climbing robots such as legs [65], wheels [66] and tracks [50]. This adhesion principle can be used with any surface. However, the adhesion is affected by environmental factors such as temperature, moisture and dust.

2.4.   Robots used to inspect WTB

Based on the explored literature, it has been indicated that there are several types of robots which are used for different inspection purposes. For instance, there are robots which are used to inspect the blades while others are used to inspect the towers. Accordingly, in order to give insights about different explored types of robots, the functions, advantages, disadvantages, and aims of inspection for some examples of the developed inspecting wind turbine blade robots are summarised in Table 2.3 to Table 2.7. Moreover, images of these robots are added to visualise their size and complexity.

Table 2.3 Climbing ring robot for inspection of offshore wind turbines [19]
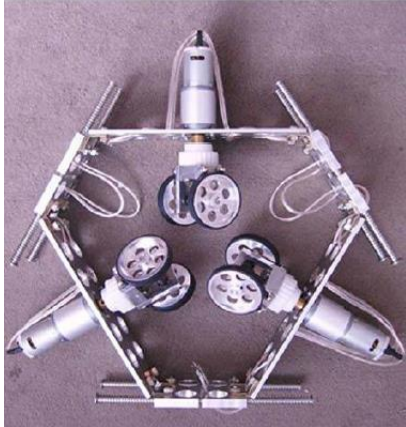
Inspecting Tower/blades	Tower
Description	The robot frame is an irregular hexagon shape with three wheels in three sides. Each wheel is equipped with two motors, one for the motion and the other for steering as illustrated in Figure 2.8. Figure 2.8 Climbing ring robot
Advantage	The robot is stable and flexible during climbing and the design of the wheels gives the robot the advantage of manoeuvrability. It can climb straight up/down a tower, climb with a spiralling motion, or rotate at the same spot.
Disadvantage	In order to be attached to the wind turbine, the robot needs to be disassembled.

Table 2.4 Robot for rotor blade inspection [20]

Inspecting Tower/blades	Blades
Description	The robot consists of a quadrangular frame structure where the blade is surrounded by the frame for inspection as shown in Figure 2.9. The frame comprises of five main parts: two side traverses, one front and one back traverse. The frame is hanged by four ropes for the movement along the blade during the inspection. Figure 2.9 Robot for rotor blade inspection
Advantage	The frame can adjust itself automatically according to the blade aerodynamic profile.
Disadvantage	The robot moves along the rotor blade by means of four ropes which means that the robot needs pre-installation before the inspection.

Table 2.5 The inchworm type blade inspection robot system [21]
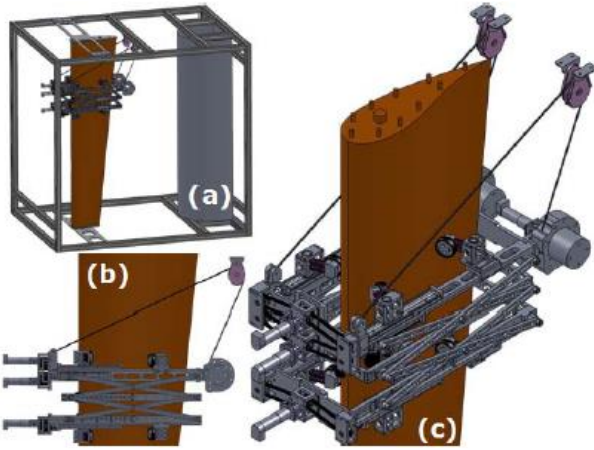
Inspecting Tower/blades	Blades
Description	The robot can move by itself on the blade surface by using an inchworm mechanism, which is constructed with two active wheels and two passive wheels that can fix the robot body on the blade, one extendable and contractible actuator as shown in Figure 2.10. Figure 2.10 The inchworm type blade inspection robot system
Advantage	The robot is designed to follow the curvature of the blade.
Disadvantage	The climbing of the robot depends on ropes from the nacelle.

Table 2.6 Maintenance robot [22]
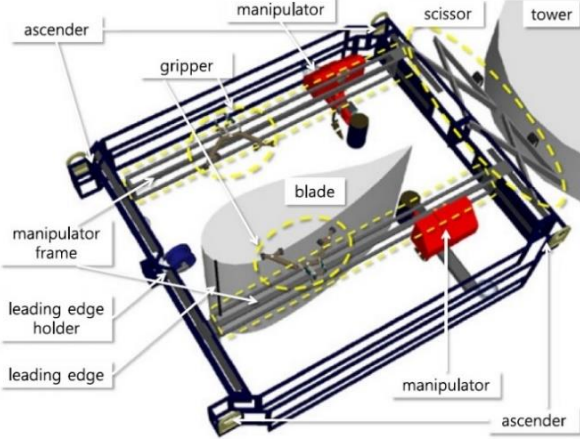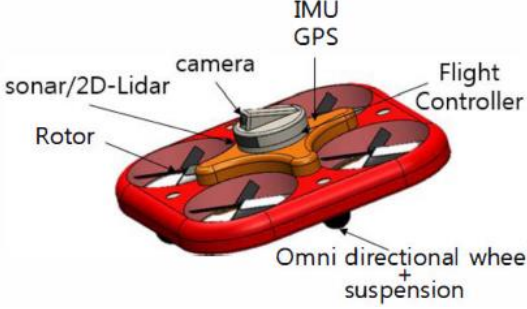
Inspecting Tower/blades	Blades
Description	The system consists of a mobile platform with two manipulators for cleaning and inspection. The robot climbs the tower and the blade using a wire driven parallel mechanism. The distance between the blade and the tower is adjusted using a scissor mechanism as shown in Figure 2.11. The inspection process is done using a phased array ultrasonic system. Figure 2.11 Maintenance robot
Advantage	The robot is equipped with two manipulators that can follow the trajectory of the blade while keeping the inspection sensor perpendicular to the blade.
Disadvantage	It requires pre-installation of the wire driven parallel mechanism before climbing the tower.

Table 2.7 Micro aerial vehicle [23]

Inspecting Tower/blades	blades
Description	The drone robot shown in Figure 2.12 consists of four rotors responsible for thrust force for flying and four wheels for wall-climbing and moving on vertical and non-flat surface. Figure 2.12 Micro aerial vehicle
Advantage	It can reach any part of the blade in a very short time and can move on a non-flat surface with an omnidirectional wheel.
Disadvantage	The power consumption of the four motors increases the discharging time of the batteries giving short operation and inspection times. Also, it is limited to surface defects only as it uses visual inspection techniques.

2.5. Current LSBU funded projects

This section is presenting different climbing robots projects that have developed and implemented to inspect the wind turbine blades. The climbing process of the robots is based on wires hanged from the WT nacelle. These projects have been presented to illustrate their design concepts, climbing methods and the NDT used for inspection. Moreover, images of these robots are added to visualise their size and complexity.

2.5.1. DashWin project

DashWin was a collaborative research project run by a group of European companies and funded by the research executive agency of the European Commission. The DashWin project aimed to develop an automated inspection system for in-situ inspection of WTB. The system consists of an agile robotic platform which can climb up the wind turbine tower as illustrated in Figure 2.13 and deploy an advanced digital shearography kit as shown in Figure 2.14. The inspection system was developed to inspect composite WTB for surface and sub-surface defects [67].
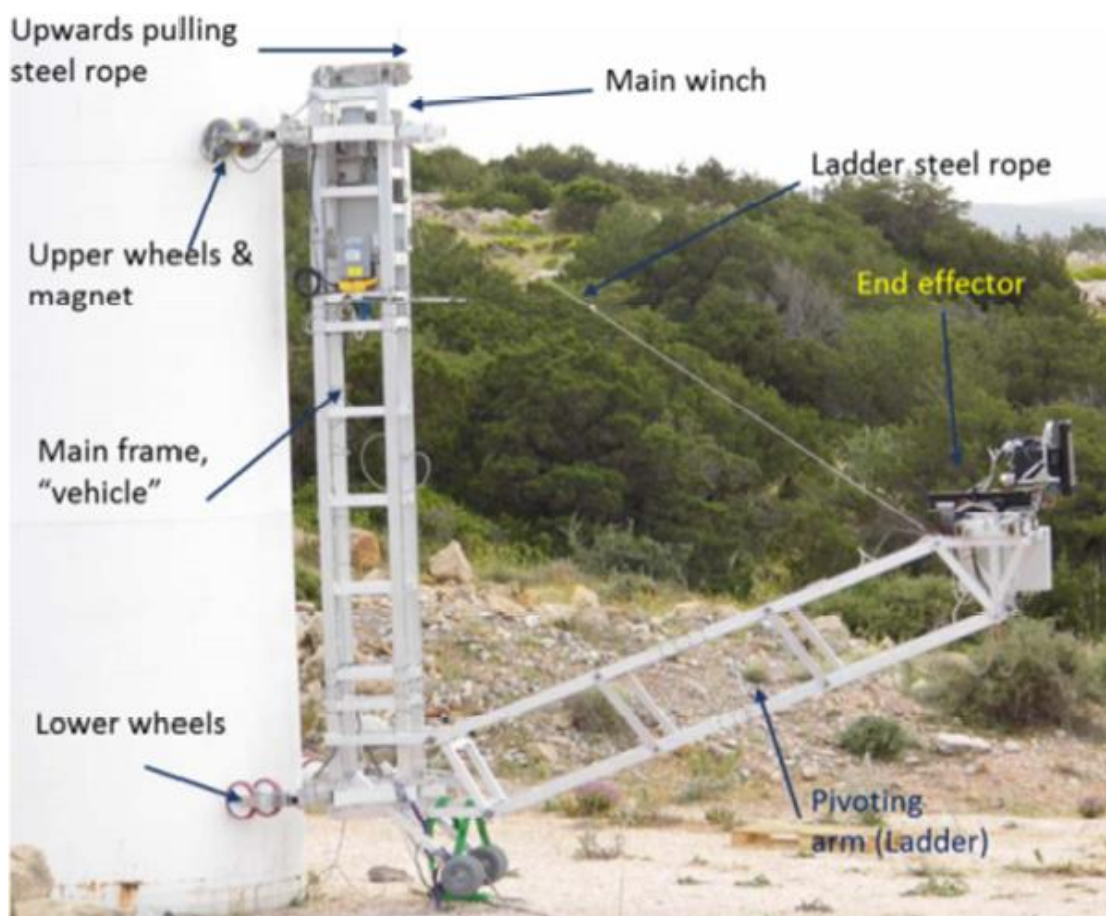
Figure 2.13 The arm of the robotic platform is fully opened to reach around 4m.
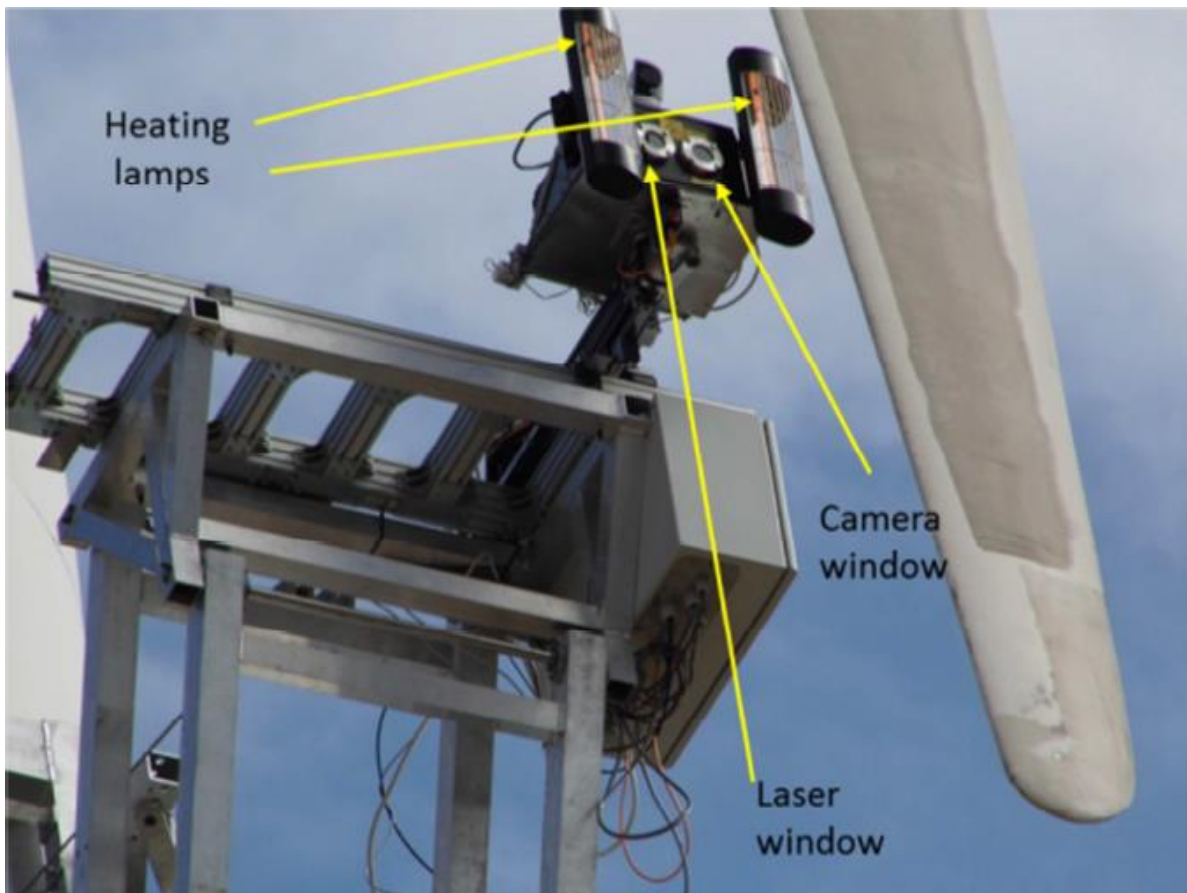
Figure 2.14 A close-up view of the NDT head (shearography) in operation.

2.5.2. WInspector

WInspector is a collaborative research project run by a group of European companies and funded by the European Commission Horizon 2020 FTI program. The program is a further development of the previous DashWin project. The project aims to develop a new deployment system which can carry the shearography system at a predefined working distance from the WTB surface. The project is mainly focusing on the development of the end-effector using vacuum suction cups. The vacuum suction pads are responsible for enabling the shearography system to attach to the WTB surface during the inspection. The shearography kit can carry out the inspection of a blade at depth of up to 50 mm. Figure 2.15 shows the concepts of the new robotic deployment strategy which is able to reach both sides of a WTB when it is positioned as a pitch angle of 90°. Figure 2.16 shows the integration of the shearography with a testing sucking robot [68].
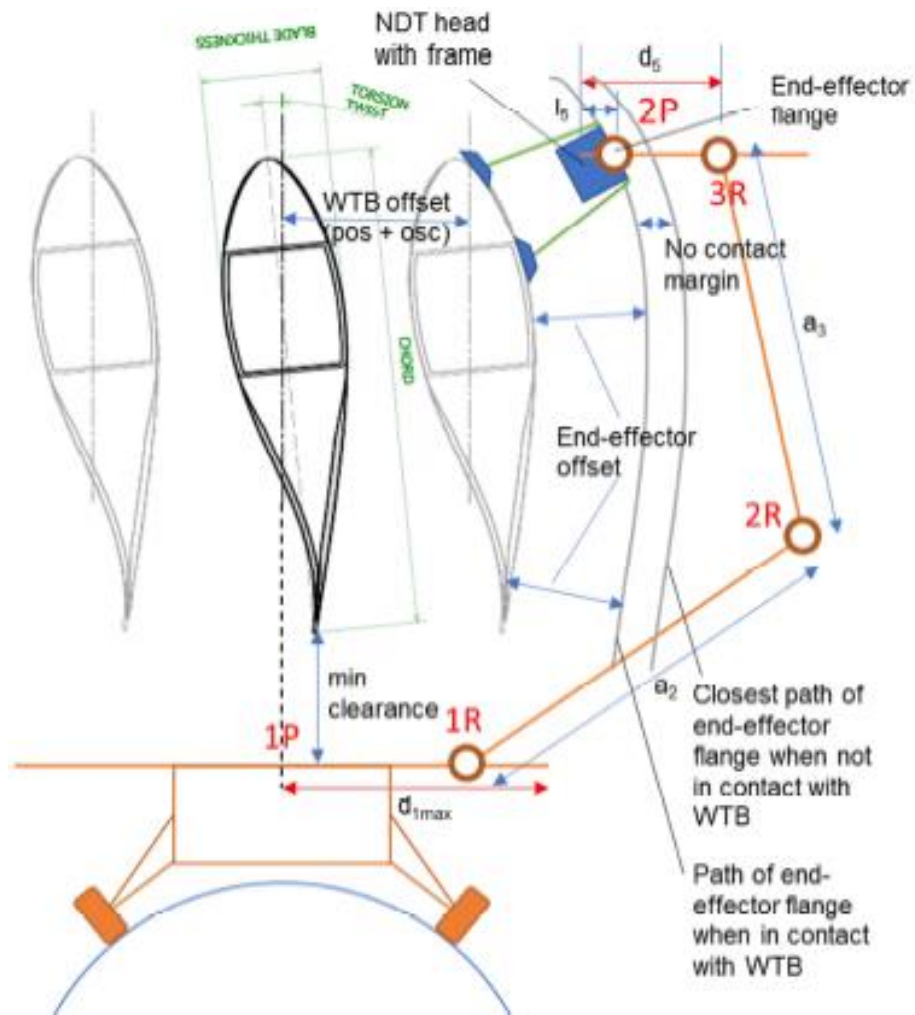
Figure 2.15 New robotic deployment strategy
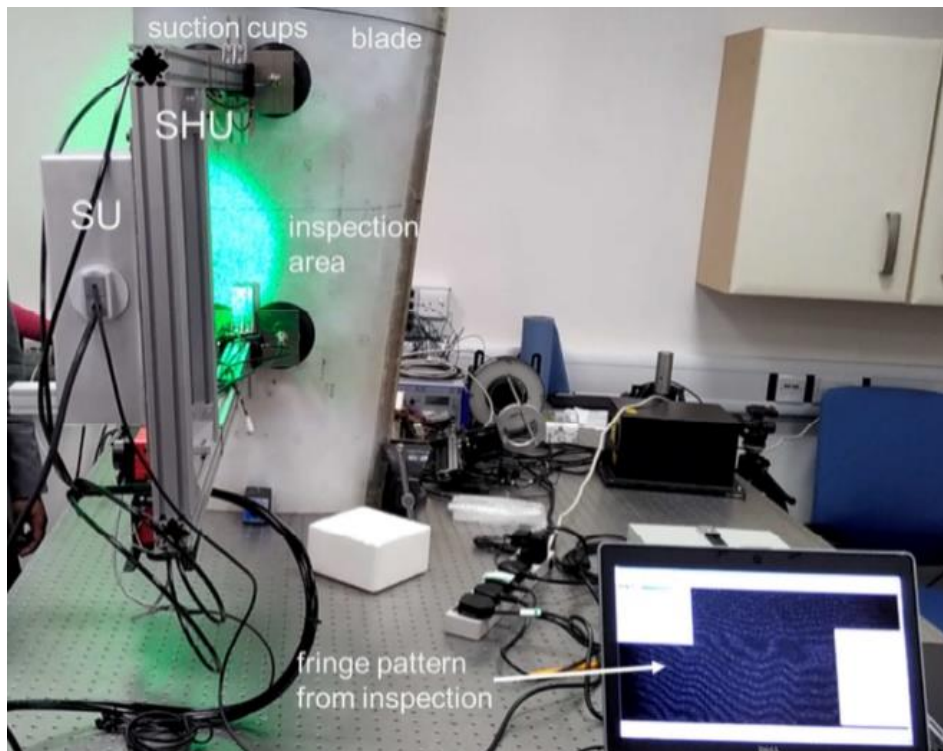
Figure 2.16 Actual integration of the shearography with a suction platform

2.5.3. RADBLAD

The RADBLAD project (funded by Innovate UK) aims to use X-ray radiography instead of the shearography as it is the best method for detecting internal defects in composite structures. It is a non-contact NDT technique and thus eliminates the need to put probes in contact and couple ultrasound with the surface of a blade. The innovation comes from the remote robotic deployment of X-ray radiography at great heights on large WT's to image the full thickness of a blade. Augmented with automated defect detection, classification and autonomous decision making, these advantages will improve the quality of inspection as compared to manual ultrasound NDT, reduce inspection times and hence reduce the cost of inspecting hundreds of blades. The RADBLAD robot system is shown in Figure 2.17. The system consists of a robot with a winch for holding an extendable scissor arm responsible for carrying the inspection tool [69].

Figure 2.17 Radblad

2.6. Wind turbine blade

The wind turbine blades are simply the most severely loaded components of the entire wind turbine structure and the components that are responsible for converting the kinetic energy of wind to beneficial mechanical energy. The blades are subjected to high loads due to the harsh and unpredictable operating conditions. The operational conditions of wind turbine blades are presented in the following sections.

2.6.1. Aerodynamic loads

The first and most important part of the blade operation is related to the working medium which is atmospheric air and its currents. These currents are characterised by their nonlinearity and chaotic behaviour. Turbulence, local vortices and boundary layers form a highly complicated and by no means uniform working volume, in which the turbine blades operate. The result of the interaction of unstable atmospheric currents with the aerodynamically shaped blades is the creation of aerodynamic loads of a nonlinear nature. These loads mechanically stress the blade structures and lead to severe bending moments. In modern large-scale wind turbines, the aerodynamic loading situation became more complex in which the big diameter of the rotor leads to strong deviations between the instantaneous blade loads. In other words, when the blades extend over the top of the wind turbine, they are exposed to more laminar and more powerful wind currents, while the lower angle of the blade rotation is done in the highly turbulent boundary layer of the earth. Additional compression effects between the blades and the tower result in a highly complicated loading situation [70].

The aerodynamic forces lead to cyclic loads on the blade structure, but these loads are abiding by the stochastic behaviour of the wind currents and their amplitude is not frequently constant. Additionally, unpredictable mechanical vibrations induced in the blade structures and the load situation becomes even more severe due to other aerodynamic effects. These are caused by local flow separation and stall buffeting. Finally, the blade structures are called upon to perform aerodynamically efficiently for a very long time and to resist both the regular and the extreme aerodynamic loads.

2.6.2. Gravitational loads

The Earth's gravitational field is considered to be a significant source of the mechanical load. The extremely long length of modern wind turbine blades combined with significant weight

leads to significant cantilever effects, which stresses the whole blade structure and especially around the area of blade roots. Very high loads and stresses are formed in this area, while the amplitude and the direction of these loads change continuously with the rotation of the wind turbine rotor. The rotor blades should be able to resist the gravitational cantilevering loads merged with the aerodynamic loads during the whole operational time span of the WT [71].

2.6.3. Centrifugal loads and momentum

The rotation of the wind turbine rotor is usually characterised by a constant angular velocity of 9-19 rpm. Although this rotational speed is low, the rotating parts form a multi-ton rotating unit with a diameter around 80 m. It is obvious that the loads from the centrifugal forces and the angular momentum are very large. The centrifugal forces significantly stress the blade root and especially the connection area between the blade and the nose cone. Nevertheless, stress caused by centrifugal forces can be detected throughout the whole blade structure and although the root area is the most intensely stressed, the blade tip area is also subjected to very high loads [72].

The mechanical brake, which is installed at the high-speed shaft of the drive train, is engaged during emergency braking conditions. The brake conveys braking torque through the gearbox to the wind turbine rotor in order to decelerate it during this extremely stressing situation. It is obvious that the whole drive train, as well as the turbine blades, suffer from these extreme loads, and critical failures can happen due to the momentum of the rotor structure. Fortunately, this kind of braking actions is almost never used. Therefore, the braking momentum of the rotor is not a usual factor which leads to blade fatigue and stress.

2.6.4. UV, water, ice and hail

Atmospheric and weather conditions play a very significant role in determining the performance characteristics of wind turbine blades and their variation with time, as well as their fatigue characteristics. This is because the wind turbine blades are operating in an unprotected mode. The continuous exposure of these structures to solar UV radiation is considered a very critical factor that highly affects the operational life of the blades. The UV rays may lead to changes in the structure of the composite materials of the blade and change them to weaker and more brittle forms. Based on that, special coatings must be applied, but the structure of these coatings should be able to get along with the blade's deformations and thermal expansions.

Rainwater is considered another environmental factor which has a high impact on the blade structure. The anti-UV coatings can protect the blade surfaces against water, and that indicates that the water itself is not so critical for the composite blade structure. However, water is highly diffusive; therefore, it can penetrate through small surface cracks into the blade structure. Consequently, due to icing effects caused by low temperatures and high wind speed, the water will expand and create cracks in the blade structure. Additionally, if the diffusion of water occurs at a bonding area, which also includes some sort of steel, the corrosion and the formation of oxides will also lead to damage to the blade structure and diminish its operational life.

Finally, the impact on the blade structure is significant in the case of water in a solid-state (hail). Hail leads to many problems on several structures just because of the impact of the free-falling ice particles. This situation is much worse in the case of the wind turbine blades because the blades are moving with high speed and especially their tips can reach very high speeds. The worst situation occurs when a blade is moving from the bottom to the top position and is impacted by hail. The impact in these cases is very crucial and leads to damage to the leading edge of the blade which significantly decreases its aerodynamic performance and hence the total energy yield of the turbine [73].

2.6.5. Temperature variations

The characteristics of wind turbine blades are greatly affected by atmospheric temperature differences. Internal stress in the blade structure and slight changes in the mechanical behaviour of the blade are triggered by the continuous expansions and contractions of the blade material. Although the blades can withstand the temperature variations under normal conditions; however, the blade construction needs special design considerations under some extreme conditions which exist at extreme north latitude locations.

2.6.6. Dirt and salt

The blade surface erosion is another significant factor which leads to blade fatigue and yield reduction. The salinity of the air current that engages the blades is one major factor for erosion. This problem is mostly noticed when wind turbines are installed near the seashore or even offshore. The seawater particles, which reach the turbine blades due to strong winds, deposit salt on every exposed surface and leads to its strong corrosion. It is worth mentioning that the most severe impact of the seawater is on steel surfaces where it is literally devastating; however, composite structures (GRP) also suffer from the negative corrosive impact of

seawater.

Dirt and sand particles negatively affect the blade performance and they also need some sort of protection. However, the impact of these parameters is not based on a chemical corrosion mechanism like seawater, but mostly on mechanical surface micro-impacts. The protection of the wind turbine blade structures is a crucial need regardless of which is the exact mechanism of blade erosion and what is the exact source of erosion. The operational lifetime of the blades and the whole wind turbine can be guaranteed to be extended only through effective protective means.

2.7.   Blade structures

Various manufacturing techniques have been developed for the construction of wind turbine blade structures. One of the most common techniques is the hollow shell, in which the shell is created by multiple glass fibre laminations of a precise outer mould. The blade is manufactured in two halves which are then to form the complete blade shape. The outer shell structure carries the loads; however, internal reinforcements are installed to blades for the sake of increasing the stiffness of the whole structure [74, 75]. GRP layers are bonded with epoxy raisin creating a very stiff and complex fibrous composite structure leading to the formation of a laminated structure. Some manufacturers also combine other materials in the composite blade structure, such as wood strips and aluminium mesh, for lightning protection. The process also includes the manual or mechanical pressing of the laminates and many other special techniques, whose aim is to guarantee the constant high quality of the final structure. The final half blade structure dries out and gains its final mechanical properties. It is then combined with the other half in order to form the final blade structure. Special weather and impact resistant gel coating are used to produce the outer smooth surface. This type of coating performs like a hybrid between the surface coating and laminate unit, thus ensuring the ability of the coating to securely stick to the blade structure for an extremely long period of time and under the most severe operational conditions [76].

2.8.   Types of damages in blades

It is obvious that the wind turbine blades are negatively impacted by various loads and stresses in addition to strong corrosion effects due to environmental reasons. The blade manufacturers exert high efforts in order to maintain the reliable and long-lasting operation of their blades

under the most severe environmental conditions on the planet. However, most of the blades are negatively affected by some insignificant or more serious problems during their service time. In the following paragraph, some of the most common blade defects will be investigated.

There are two types of damages that occur to WTBs, both on the inside and outside. Damage inside blades are cracks at the bonding resin, missing adhesive, discontinuities on the sandwich, delamination within the glass fibre reinforced plastics (GFRP) or the sandwich, crack on the web, an excess of bonding resin, problems in the bonding, waves, air inclusions, etc. [77]. Figure 2.18 illustrates the type of damage that might occur to the WTBs.
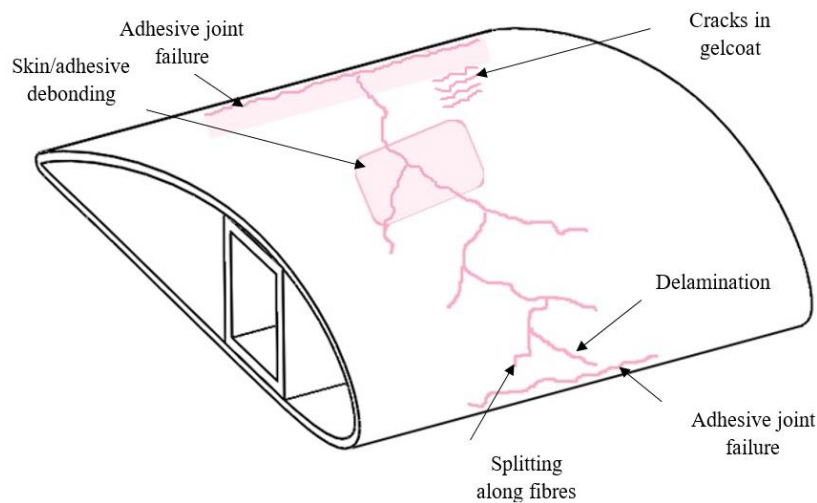
Figure 2.18 Types of damage in WTB

Damage outside the blade is on the surface such as erosion, impact, deficient bond at the bonding surfaces, and cracks [78, 79].

Any minor damage that happens to wind blades leads to an unbalanced rotating mass. This affects the performance of WT due to the generated vibration force which can affect the whole WT or might damage another WT in the wind farm [80]. Therefore, a periodic inspection should take place to avoid any failure that might happen.

2.9. Non-destructive testing for inspecting WTB

There are several non-contact nondestructive testing techniques suitable for inspecting WTBs fabricated from carbon fibre reinforced polymer (CFRP) and/or glass fibre reinforced polymer (GFRP) [81]. These nondestructive techniques include sonic [82], ultrasonic [83], electromagnetic, shearography [84], thermography, optical [85] and radiography testing as shown in Figure 2.19. Each of these techniques is reviewed below.
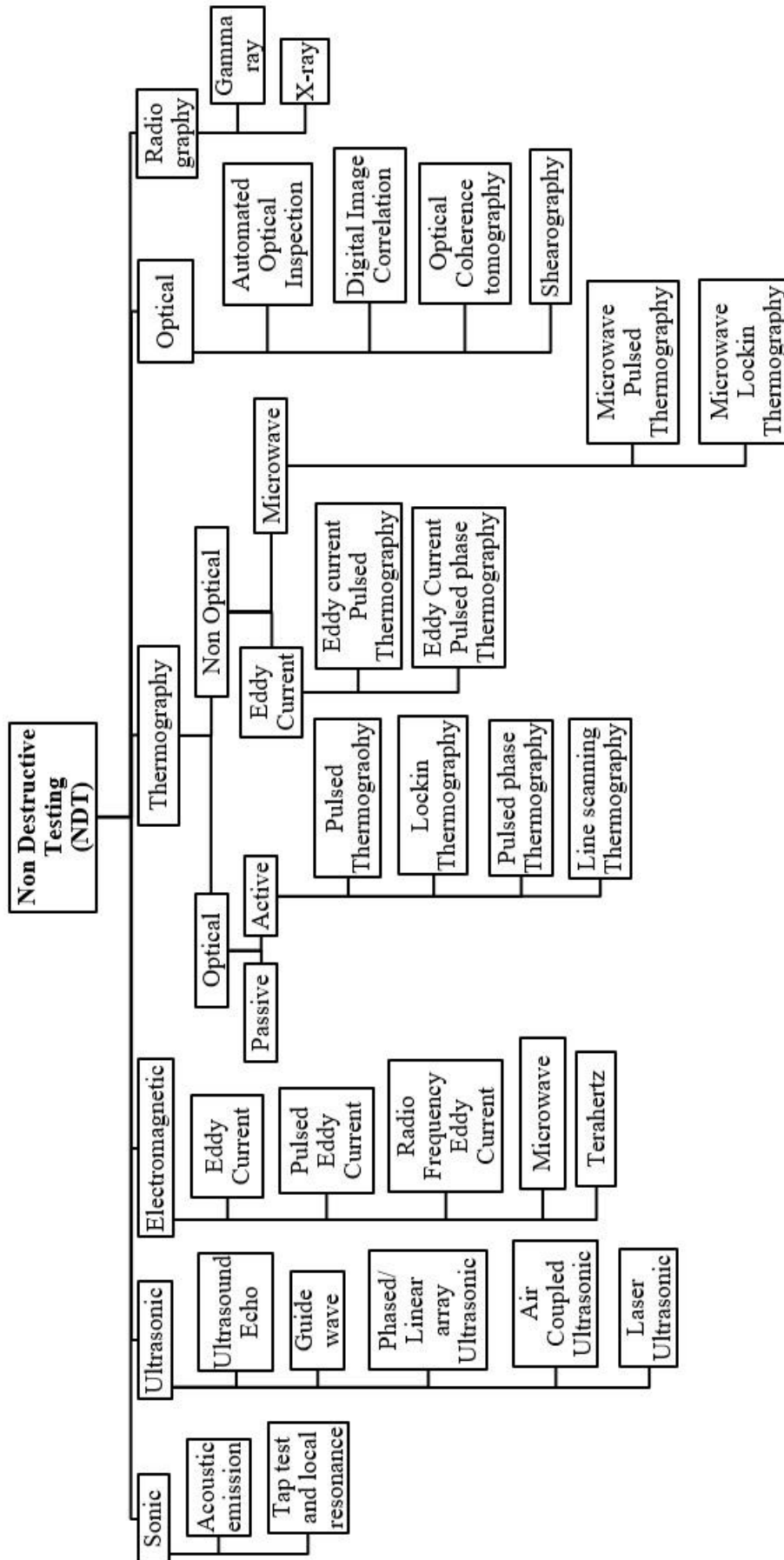
Figure 2.19 NDT types

2.9.1. Sonic NDT

Sonic NDT is a nondestructive technique used for WTB inspection and includes acoustic emission, tap test and local resonance.

2.9.1.1. Acoustic emission

Acoustic emission (AE) is mainly used for nondestructive testing and structural health monitoring. The AE wave is a non-stationary signal that can detect and monitor cracks in a failing part. This technique can be used for in-situ inspection of the materials or structures. However, its major disadvantage is that there are a lot of acoustic sources other than the crack which swamp the acoustic emission from a propagating crack [86].

2.9.1.2. Tap test and local resonance spectroscopy

Local resonance spectroscopy can be used to detect shallow delamination or air trapped near the surface. The technique is a progression of tapping tests which are done in periodic inspections of WTBs. It uses an impulse hammer to generate an impact on the surface of a WTB as illustrated in Figure 2.20. Vibration is produced in the area of excitation and a sound is generated which is recorded by a microphone and then analysed according to contact stiffness of the surface. The contact stiffness is related to the structural properties and affects the contact time of hammer and material. Extra data can be collected on the internal surface by the hammer tip. The defect types and sizes are difficult to be recognised due to the presence of ambient noise and the difficulty of controlling the impulse force [14].
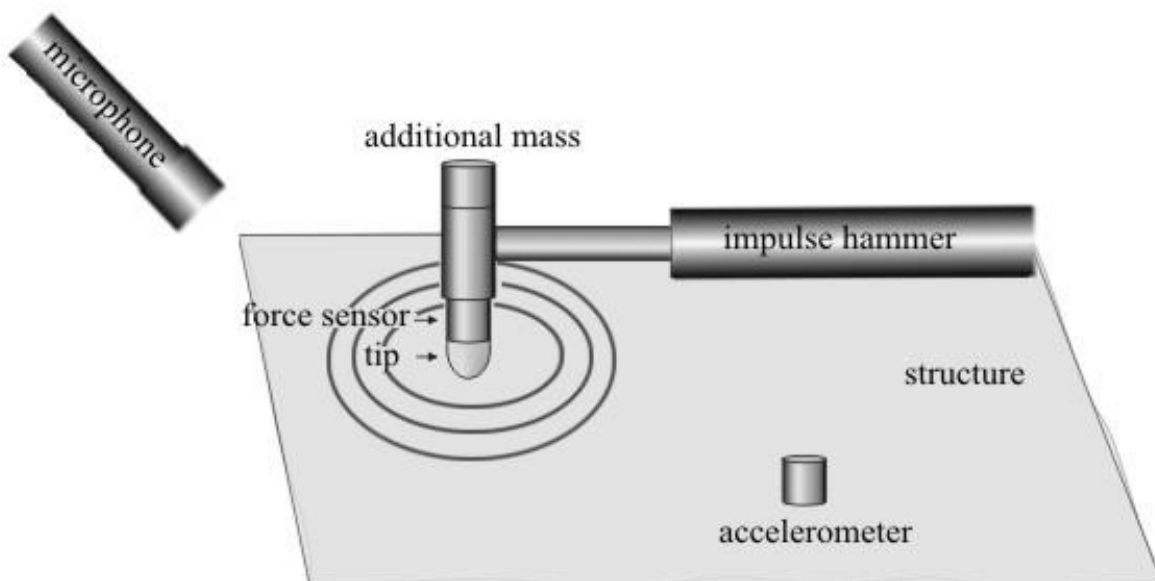
Figure 2.20 Measurement principle of the local resonance spectroscopy [14].

2.9.2.   Ultrasonic NDT

An ultrasonic technique is based on ultrasonic wave propagation in the material to inspect the internal surface structure and is considered as one of the types suitable for inspecting composite materials [77, 87]. Types of ultrasonic techniques are pulse-echo, guided wave, phased linear array, air-coupled and laser ultrasonic [88, 89].

2.9.2.1.   Ultrasound-Echo Technique

The principle of the ultrasound-echo technique is based on the delay-line of the reflected wave from the multilayer GFRP as shown in Figure 2.21. The pulse is sent through the material and reflected by variation in material or the rear side. The echo can be used to characterise the internal multilayer structure.
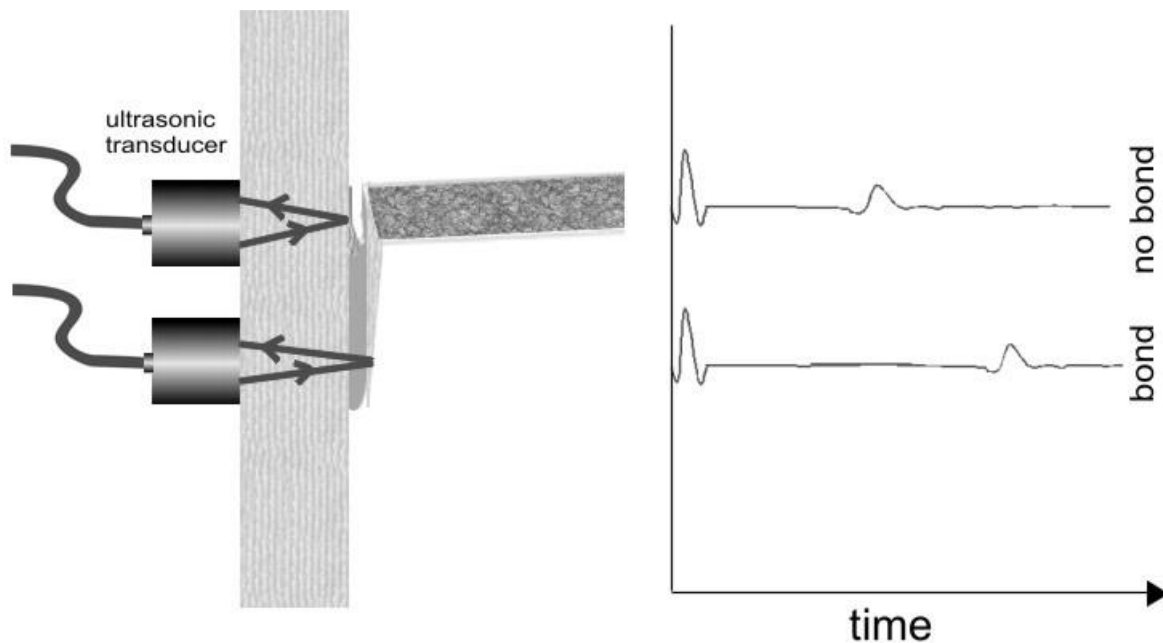
Figure 2.21 Ultrasound echo at a bonding area of WTB [89]

The GFRP requires a high voltage pulse as it is a high damping material. So, low-frequency waves are better for such highly damping materials since high-frequency waves are strongly damped. However, the acoustic waves are sensitive to defects that lie within the scope of the utilised wavelength. A practical trade-off between damping and delamination must be found. Ultrasound techniques require wet coupling to the test surface which is a disadvantage for remote and automated NDT. A dry coupling of ultrasonic transducers can be accomplished by the utilisation of silicon layers [89].

2.9.2.2. Air-coupled guided wave

The principle of the air-coupled guided wave technique is illustrated in Figure 2.22 [90]. A pair of air-coupled transducers are used for non-contact scanning of the WT sample.
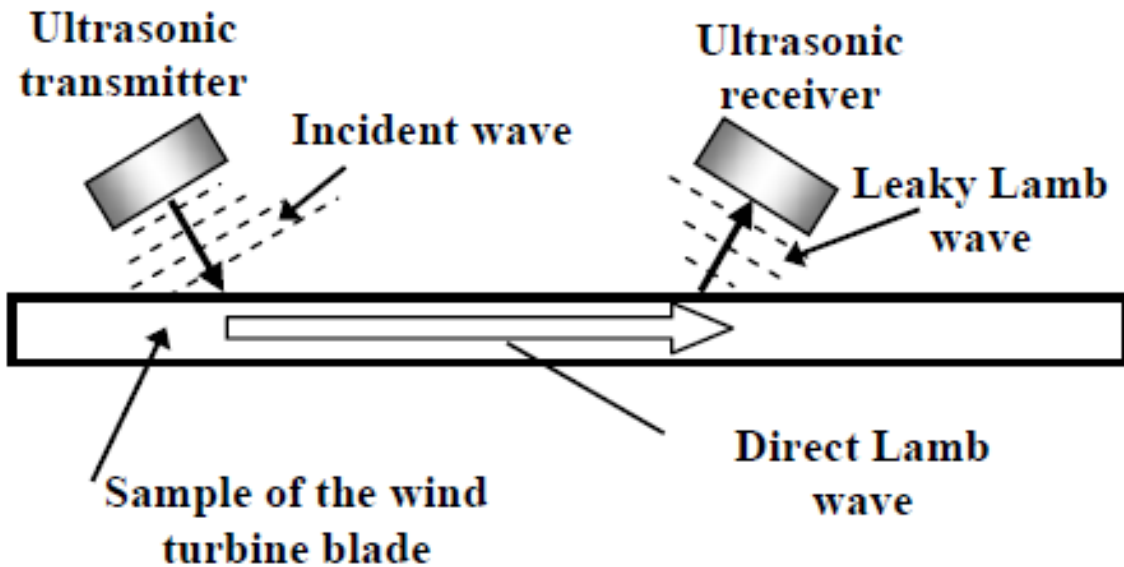
Figure 2.22 The principle of the air-coupled guided wave [90]

In [91] two different ultrasonic transducers planner and focused were used in pulse-echo immersion testing with moving water container for inspection of WTBs. The two transducers were utilised in inspecting three circular defects with a different diameter. The contact pulse-echo immersion technique with moving water container was used to inspect the defects. The air-coupled technique using guided waves is also used to inspect the artificial defects. The results show that the shape and size of the internal defects are clearer using the contact pulse-echo immersion testing technique using a moving water container. The delamination defects close to the external face of the WTB should be inspected by a higher frequency focused transducer. While delamination and thickness changes in deeper layers are detected with the low-frequency planar transducer.

2.9.3. Optical thermography

Thermography measures the propagation of heat using a camera with many infrared sensors that can detect small variation in temperature. The temperature variation can be traced as a contour and presented on a computer.

There are two basic types of optical thermography; passive thermography and active thermography. In passive thermography, the camera is projected at the inspection area and a

temperature map is constructed from the thermal image. For active thermography, heat is induced through the surface by using an external source and by recording the surface temperature. An image is constructed showing the internal structure of the part with defects.

The advantage of thermography is that the inspection process is relatively fast, contactless, suitable for inspecting composite material and can easily detect delamination. The disadvantage is a limitation in inspecting high thickness [92].

2.9.4. Optical shearography

The technique uses the optical wave to detect any deformation in the material surface in non-destructive testing, strain measurement, and vibration analysis. Advantages of shearography are an inspection of large-area per time, environmental disturbance does not affect the inspection, it is a contactless method and it is suitable for inspecting non-homogenous materials [93].

The technique has been improved tremendously in recent years with significant developments in charge-coupled device (CCD) cameras, lasers, and computing hardware. The technique uses the coherent, monochromatic properties of laser light to develop speckle patterns on the testing surface. Common loading techniques, which include thermal loading (e.g., high power flashlamps), pressure loading (e.g., vacuum), or vibrational excitation, are adopted. The speckle patterns on the test surface are recorded as one image when the specimen is unstressed and one with applied stress. The technique requires an image shearing device (e.g., Michelson interferometer) in front of the CCD camera [94].

2.9.5. Radiography x-ray

X-ray computed tomography (CT) technology is an extensively used technology in the medical field that also can be used for industrial nondestructive material inspection. The basic principle of radiography is based on the variation of absorption of X-ray photons as they go across the material [78, 90]. A three attenuation image can be constructed using complex algorithms from a series of X-ray two-dimensional attenuation images are taken from different projection angles [92]. It is the best technique to use on blades constructed of composite materials.

2.10. Chapter summary

In this chapter, a survey of climbing machines reported in the literature has been conducted to determine the design requirements of climbing robots in order to select the most appropriate locomotion and adhesion method for a robot platform that can operate on wind turbine towers and carry the required NDT payload. The construction of wind turbine blades such as their aerodynamic shape and composite structure have been noted since inspection methods will have to cater to these shapes. Loading and environmental conditions that stress blades and cause different types of damage have been identified. A survey of various NDT methods used to inspect blades has been carried out. As a conclusion, since wind turbine towers are of steel construction, climbing robots that use permanent magnet adhesion and wheeled locomotion will provide the necessary energy-free adhesion and speed to carry the large payload constituted by scanning arms and NDT sensors such as X-ray radiography generator and detector units. The best NDT techniques for composite blade inspection are ultrasound and X-ray radiography. Ultrasonic and X-ray NDT can detect the defects in composite materials and determine the size of the damage. Ultrasonic inspection can recognise delamination flaws and give detailed results, even in thick parts. However, sophisticated signal processing, long acquisition time and the need for contact and ultrasound coupling decrease dramatically its potential for huge parts inspection like WTBs. Also, the ultrasonic resolution is relatively low to give a precise position of the crack tip. Computed X-ray radiography is an excellent technique to examine composite materials but is used to NDT blades that have been removed from a wind turbine tower and brought to an X-ray facility. The use of in-situ inspection of WTBs with X-ray radiography is very limited in the literature. A limitation to applying X-ray radiography is that a detector is required on the other side of the blade and the weight of the X-ray generator is relatively high with attendant problems of carrying the NDT payload and deploying it around a blade. A robot that can carry X-ray equipment up a tower and present it to a blade would, therefore, be a game-changer innovation.

Chapter 3

Adhesion force

3.1. Introduction

The aim of the research reported in this thesis was to develop a tower climbing robot that can carry a payload of NDT sensors (X-ray radiography) up to a WTB to perform blade inspection. It was, therefore, important to design a robot with sufficient adhesion forces to prevent the overturning and sliding of the robot both during motion and when stationary with inspection arms deployed to reach blade surfaces. Permanent magnet adhesion to a steel tower was the best method to allow wheeled motion and to provide large adhesion forces. This chapter presents modelling, simulation and optimisation of the magnetic adhesion force for wall climbing robot by focusing magnetic flux using a suitable configuration of iron yokes and rare earth permanent magnets. A finite element analysis is performed to find an optimum design of a magnetic adhesion mechanism for ferrous surfaces that maximises the magnetic adhesion force. This, in turn, maximises the payload that can be carried by the climbing robot. Experiments have been designed using the response surface methodology (RSM) to study the effect of identified independent parameters (namely the distance between magnets, air gap and yoke thickness) that affect the response variable i.e. the magnetic adhesion force. A quadratic regression model has been developed to represent an empirical relationship between the response variable and the independent variables. Statistical analysis of the predicted model has been investigated using analysis of variance (ANOVA). To inspect the adequacy of the predicted quadratic model, validating experiments have been carried out at different conditions where the experimental results showed similar response values to the predicted model responses. Numerical optimisation using COMSOL Multiphysics has been performed to predict the optimum variable conditions.

3.2. Theoretical background

In a magnetic field, there is no current hence in an electric current free region, thus

$$\nabla \times H = 0 \qquad\qquad (3.1)$$

Where:

H   : Is the magnetic field intensity (A/m)

$\nabla \times$: (curl)   : Represents the rotational component in a vector.

Based on equation (3.1) it can be observed that there is no rotational component, this is because magnetic fields are propagating in the form of closed loops as shown in Figure 3.1.
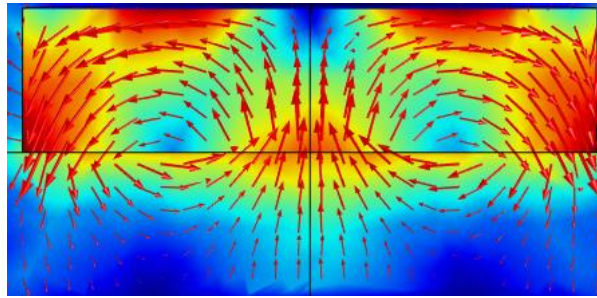
Figure 3.1 Magnetic flux density.

It is possible to define the scalar magnetic potential, V_m, from the relation.

$$H = -\nabla V_m \qquad (3.2)$$

This is analogous to the definition of the electric potential for static electric fields. Using the constitutive relation between the magnetic flux density (B) and the magnetic field.

$$B = \mu_0(H + M) \qquad (3.3)$$

Where:

M   : Is the magnetization

Using the fact that magnetic fields are propagating in the form of closed-loop, the diversions of the magnetic flux density can be given by:

$$\nabla . B = 0 \qquad (3.4)$$

By substituting equation (3.2) and (3.3) in equation (3.4) we can get an equation for V_m,

$$-\nabla . (\mu_0 \nabla V_m - \mu_0 M_0) = 0 \qquad (3.5)$$

3.3. COMSOL model description and boundary condition

In order to model the magnetic adhesion force generated from a permanent magnet, COMSOL Multiphysics was adapted. The AC/DC module was utilised.

Two boundary condition planes are considered in the current COMSOL Multiphysics model. A normal XY-plane is considered as a symmetric boundary condition where the norm of the magnetic flux density can be expressed by:

$$n.(\mu_0 \nabla V_m - \mu_0 M_0) = \text{n} . \text{B} = 0 \qquad (3.6)$$

Where:

n : Represents the normal vector

On the other hand, a tangential boundary condition is found at the XZ-plane where an antisymmetric boundary condition is considered as a result the tangential magnetic flux density vanishes and the scalar magnetic potential can be calculated.

The model is surrounded by an adequate simulation volume where the dimensions are chosen large enough, with respect to the simulated volume, to minimise the impact of the extreme boundary condition presented at the edges on the region around the magnet.

For the finite element method implementation, a tetrahedral mesh was chosen. The dimension of the mesh was selected to be 375 µm to adapt the minimum feature length in the proposed models.

3.4. COMSOL model validation

In order to validate the COMSOL model proposed to simulate the magnetic adhesion force effect in the wall climbing robot, a pre-defined permanent magnet COMSOL model is demonstrated in this section.

3.4.1. Model geometry

The permanent magnet model consists of two parts. A horseshoe part of length 0.1 m acts as a magnet and a rod with length 0.1 m represents the surface to be attracted. The dimensions are shown in Figure 3.2. There is a distance between the horseshoe and the rod which is called the air gap.
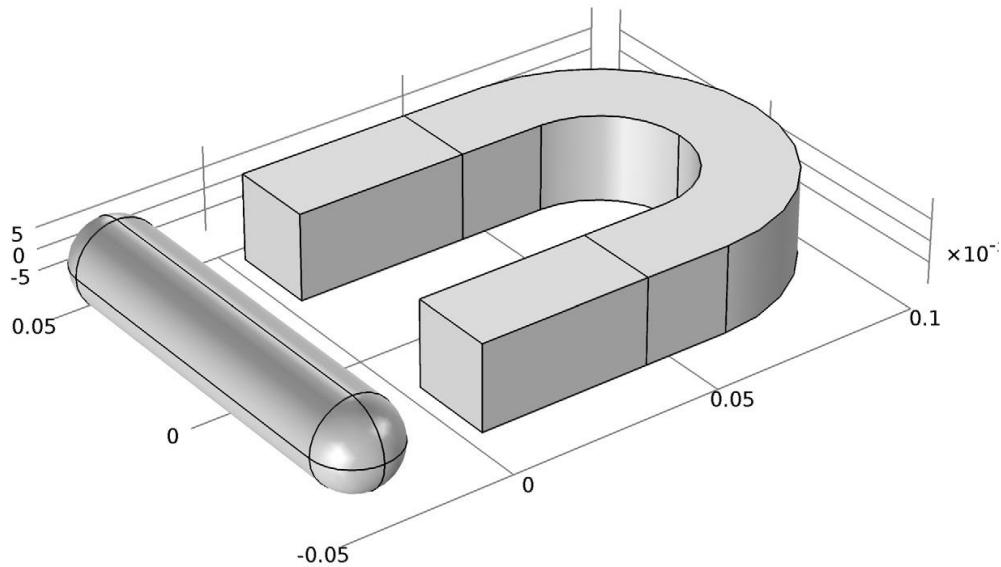
Figure 3.2 Permanent magnet model 3D view of the geometry

3.4.2. Defining the material for the geometry

The horseshoe is divided into two parts, a half-circle and two rectangular parts. Due to the symmetry of the geometry, only one fourth has been modelled as shown in Figure 3.3. The material assigned to the half-circle and the rod is iron. While the material assigned to the simulation volume is air. The properties of the air and iron are listed in Table 3.1.
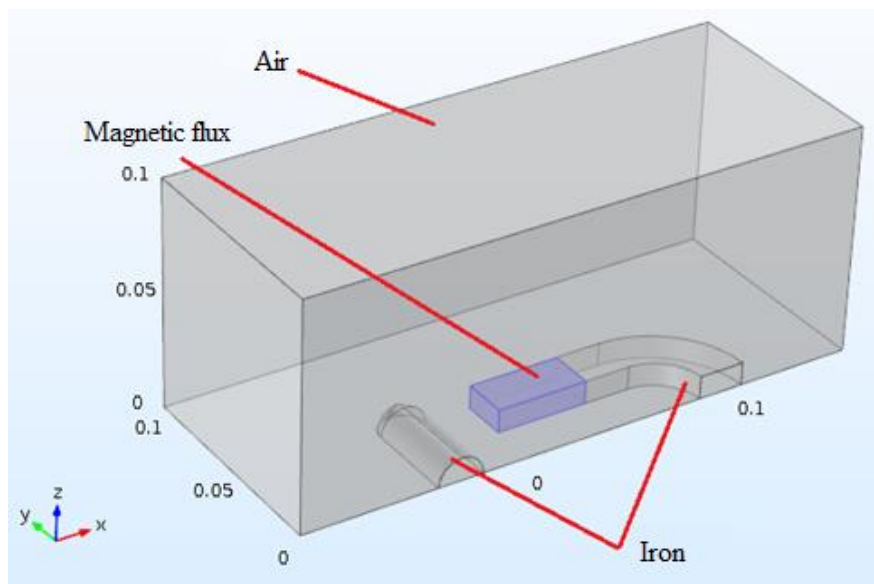
Figure 3.3 One fourth of the model

Table 3.1 Material properties

Property of Material	Relative permeability
Iron	4000
Air	1

3.4.3. Applying physics

A magnetic flux conversion has been applied to the rectangular part of the horseshoe shown in Figure 3.3. Where the magnetization **(M)** is assigned in the x-direction as the values listed in Table 3.2. The magnetization is used to distinguish between the magnetic adhesion and the surface to be attracted.

Table 3.2 Permanent magnet magnetization across the 3 axes

Magnetization [kA/m]	**Direction**
750	X
0	Y
0	Z

3.4.4. Model results

Figure 3.4 shows the norm of the magnetic flux density across the XY-plane. A minimum magnetic flux density is observed across the air gap as well as the non-magnetized rod. On the other hand, the magnetic flux density through the rectangular box of the horseshoe records its peak. The simulation result showed a perfect agreement with a predefined COMSOL model published in [95].
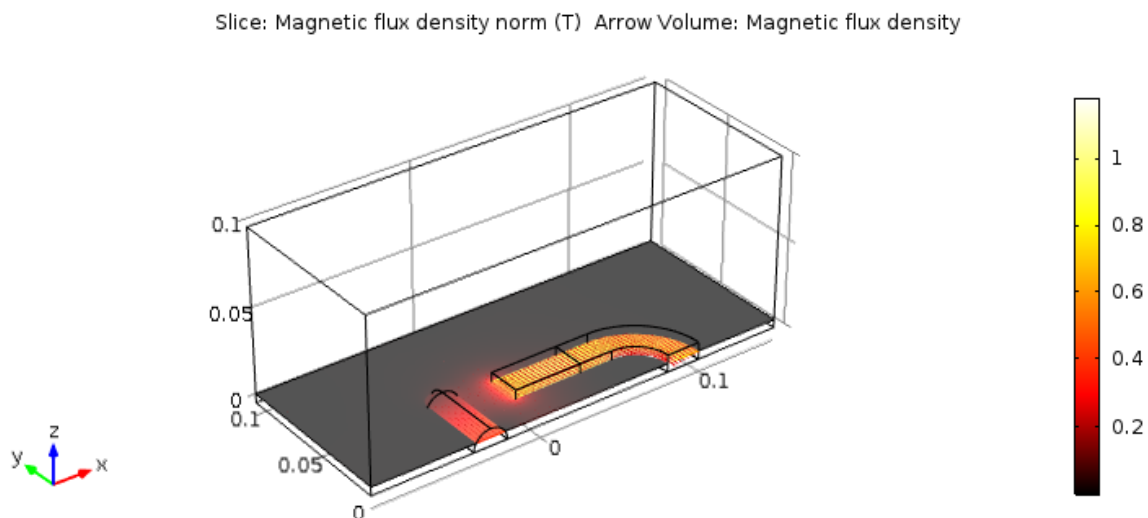
Figure 3.4 The norm of the magnetic flux density across the XY-plane

3.5. Simulating the magnetic adhesion force of wall climbing robot

In this section, a finite element model for the magnetic adhesion force of a wall climbing robot is demonstrated. A portion of the wind turbine tower is modelled as the surface to be attracted.

3.5.1. Model geometry

The magnetic adhesion force of the wall climbing robot model consists of five parts. The first part is the wind turbine tower which is modelled with dimension 1 m in diameter and 1.5 m height as shown in Figure 3.5. The tower represents the surface to be attracted similar to the rod in the previously described model. The other four parts are three neodymium magnets N35 with dimension $50 \times 50 \times 12.5$ mm and a backplate called the yoke with length 250 mm, width 50 mm and thickness 11 mm, as illustrated in Figure 3.6. There is a distance between the tower and the magnets for the air gap.
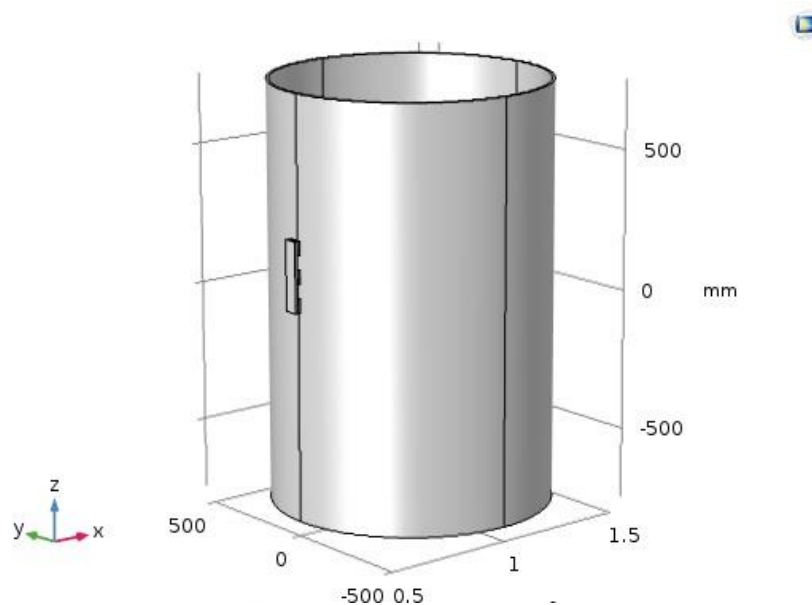
Figure 3.5 3D model for the wind turbine tower prototype
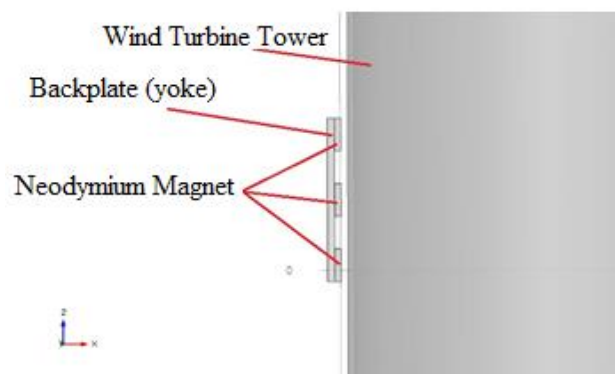
Figure 3.6 Arrangement of the neodymium magnet with the yoke

The model is enclosed by a simulation box volume where the dimensions are chosen large enough, with respect to the model volume. The dimension of the box is 2 m for each side as shown in Figure 3.7.
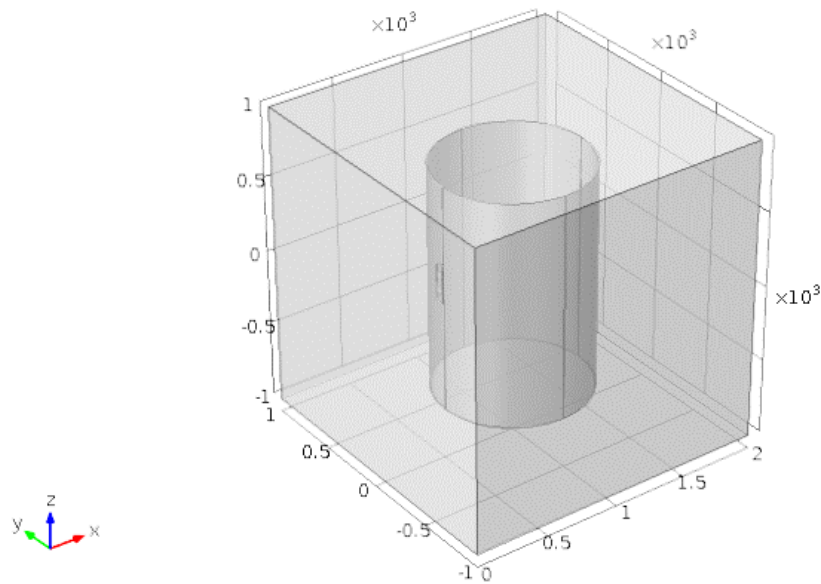
Figure 3.7 The airbox simulation volume

3.5.2. Defining the material for the geometry

The material assigned to the tower and the backplate (yoke) is iron and the material assigned to the simulation volume is air.

3.5.3. Applying physics

A magnetic flux conversion has been applied to the three rectangular parts attached to the yoke representing the magnets as shown in Figure 3.6. Where the residual flux density (**B$_r$**) is given by:

$$B_r = \mu_0 \mu_r M \qquad (3.7)$$

Where:

μ_r is the relative permeability of the neodymium magnet which is equal to 1.05 [96, 97]

The residual flux density (**B$_r$**) is assigned in the x-direction as the values listed in Table 3.3.

Table 3.3 Residual flux density across the 3 axes

Residual Flux Density (Br) [T]	Direction
1.21	X
0	Y
0	Z

The polarity of the neodymium magnet is chosen to be alternating by rows through assigning a positive and negative residual flux density respectively. Reflecting this on the current model, the middle magnet shown in Figure 3.6 has been assigned a different polarity, negative residual flux density, with respect to the other two magnets.

3.6. Magnetic adhesion force model results

A set of simulations were investigated using COMSOL Multiphysics to study the different parameters affecting the magnetic adhesion force such as distance between magnets, the air gap between the magnet and the adhesion surface, magnet dimensions, and multi yoke with different intermediate gap and dimensions. The target is to achieve the maximum adhesion force that can carry the climbing robot with the nondestructive testing equipment during the inspection of the WTB.

3.6.1. Varying the distance between magnets

To investigate the effects of distance between magnets, a model was built using three magnets attached to a yoke in opposite polarity as shown in Figure 3.8. The dimensions of the magnets used are $50 \times 50 \times 12.5$ mm. The distance between the magnets is varied from 10 mm to 150 mm and the magnetic flux density norms are observed from the simulations.
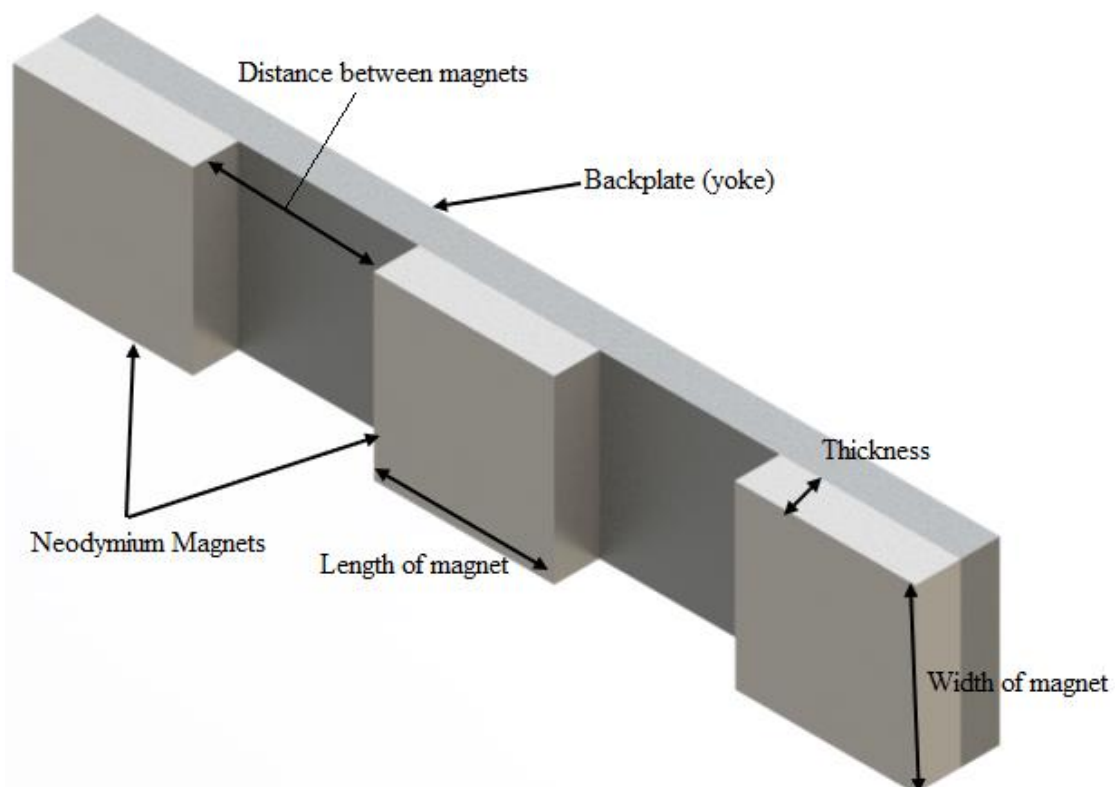
Figure 3.8 Magnetic adhesion system

3.6.2. Effect of the air gap between magnets and surface

A simulation was carried out to study the effect of varying the air gap between the magnets and the surface. To evaluate this scenario, three neodymium magnets are attached to a cast-iron backplate (yoke) by two magnets on each corner with the same polarity and the middle one reversed polarity. Dimensions of the magnet used are length 50 mm, width 50 mm, thickness 12.5 mm, yoke thickness 20 mm, length 260 mm and width 50 mm. The distance between every two magnets is 55 mm. The results show that as the air gap increases the magnetic adhesion force decreases exponentially as shown in Figure 3.9 where the air gap is varying from zero to 20 mm. The magnetic adhesion force without air gap was about 5300 N and at 20 mm air gap reaches to about 230 N.
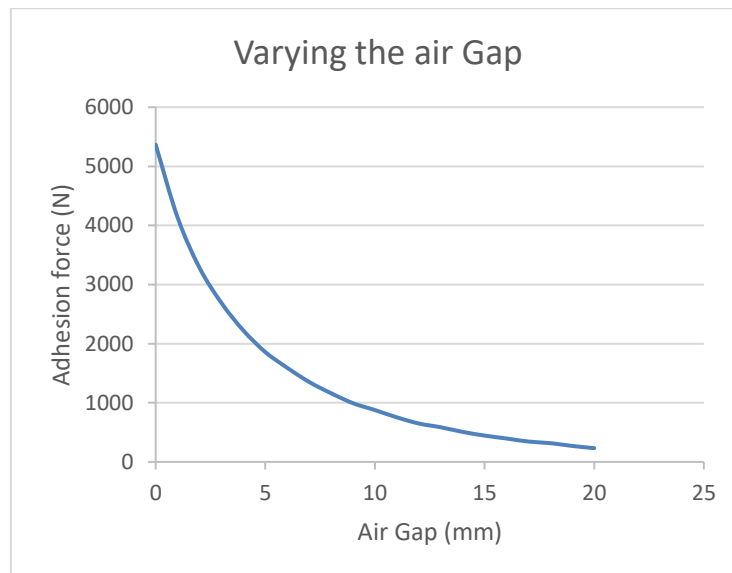
Figure 3.9 Varying air gap, for yoke dimensions 260 × 50 × 20 mm distance between magnets 55 mm.

3.6.3. Varying the length of the magnet

Another simulation was to study the effect of varying the length of magnets from 10 mm to 150 mm and length of the yoke from 140 to 560 mm with keeping the same distance of 55 mm between magnets. The air gap between the magnets and the surface is 10 mm and the arrangement of the magnet is the same as the previous simulation. The length of the yoke was calculated to be the length of one magnet multiplied by three plus the distance between each magnet. As the length of a magnet increases, the magnetic adhesion force increases linearly as shown in Figure 3.10. The magnetic adhesion force with magnet length 10 mm and yoke length 140 mm was about 72 N, then it continued to increase until it reached 2930 N with magnet length 150 mm and with yoke length 560 mm.
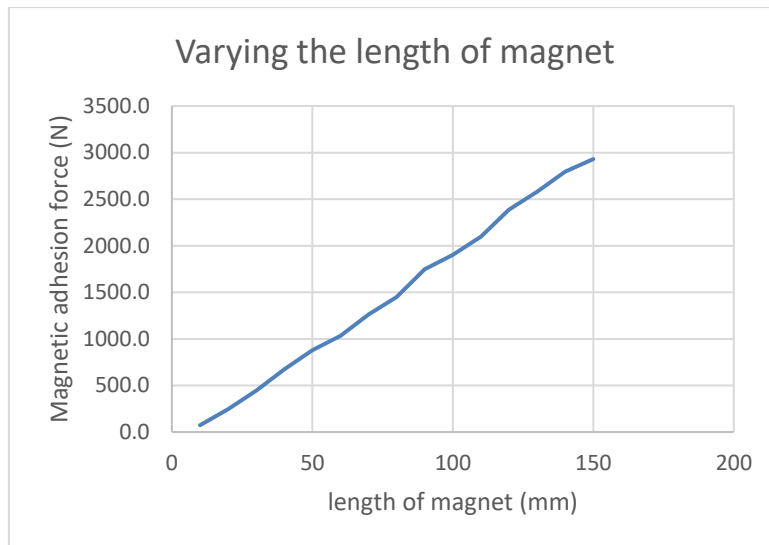
Figure 3.10 Varying magnet and yoke length at air gap 10 mm

3.6.4. Varying the magnet width

A simulation was carried out to study the effect of varying the width of magnets from 10 mm to 150 mm and width of the yoke from 10 to 150 mm with the same specification of magnet, yoke and air gap as mentioned in the above simulation. The results show that as the width of a magnet increase, the magnetic adhesion force increases linearly as shown in Figure 3.11. The magnetic adhesion force with magnets and yoke width 10 mm was about 81 N, then it continued to increase until it reached 2587 N with magnet and yoke width 150 mm.
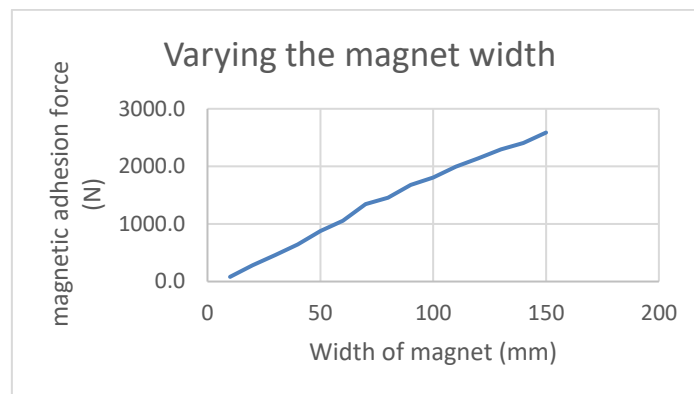
Figure 3.11 Varying the magnet and yoke width at air gap 10 mm

3.6.5. Varying the magnet thickness

The fourth simulation was to study the effect of varying the thickness of magnets from 1 mm to 50 mm with the same specification of magnets, yoke and air gap as described in the above simulation. The results show that the magnetic adhesion force increased sharply as the thickness of magnet increased from 1 to 23 mm while from 23 to 50 mm it increased steadily as shown in Figure 3.12. The magnetic adhesion force with magnet thickness varying from 1

to 23 mm increased from 31.5 to 1555 N while from 23 to 50 mm it increased from 1562 to 1876 N. Another simulation was investigated by increasing the magnet thickness by placing two magnets over each other and which gave the same results. Increasing the parameter values further in all the above simulations, will result in the same trend except this simulation which showed a levelling of adhesion force.
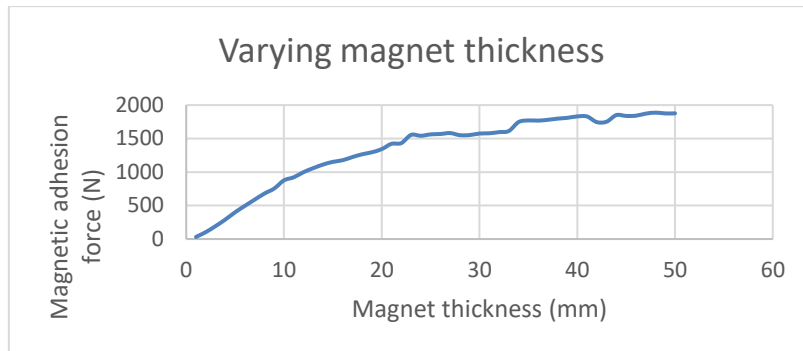
Figure 3.12 Varying magnet thickness, magnet dimensions 50×50, yoke dimensions $260 \times 50 \times 20$ mm at air gap 10 mm

3.6.6.   Increasing the number of yokes horizontally and vertically

A set of simulations were carried out by increasing the number of yokes in a plane in the horizontal and vertical direction. The yoke dimensions were 260 mm in length, 50 mm in width and 20 mm in thickness. Three magnets are used in each yoke with dimensions of 50 mm in length, 50 mm in width and 10 mm in thickness and the distance between magnets is 55 mm. The yokes were distributed around the centre axis with two different distances 50 mm and 30 mm between each yoke as shown in Figure 3.13.
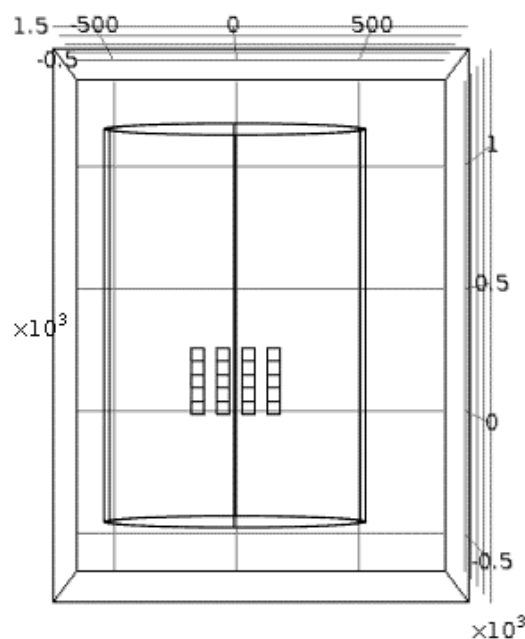
Figure 3.13 Yoke configuration in the horizontal direction

51

The simulation was carried out with one, two, three and four yokes. Figure 3.14 illustrates the magnetic adhesion force by changing the number of yokes in the horizontal direction. It is clear from the graph that increasing the number of yokes by more than two in the horizontal direction with a distance of 50 mm between yokes does not affect the magnetic adhesion significantly, as the air gap increases between the magnets and the surface due to the curvature of the cylinder. The magnetic adhesion force with one yoke was 876 N and with two yokes was 1265 N. while with distance 30 mm between yokes the adhesion force with two yokes was 1629 N.
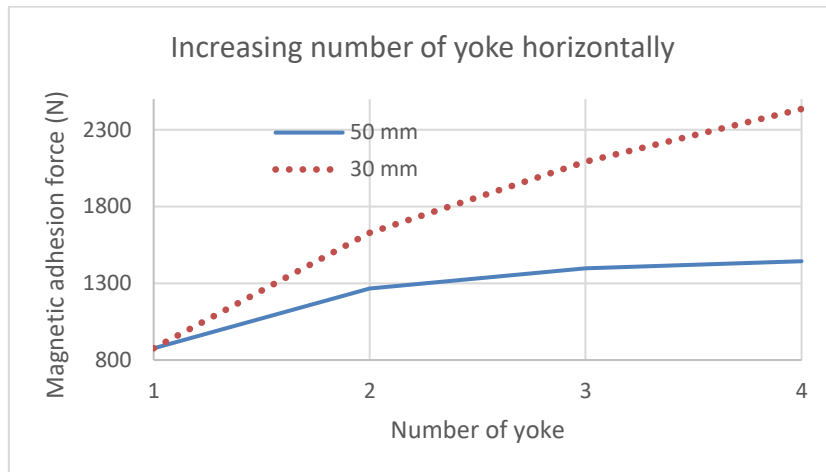
Figure 3.14 Yokes in the horizontal direction with a different intermediate gap 50 mm and 30 mm

The last simulation was carried out by increasing the number of yokes in the vertical direction as shown in Figure 3.15.
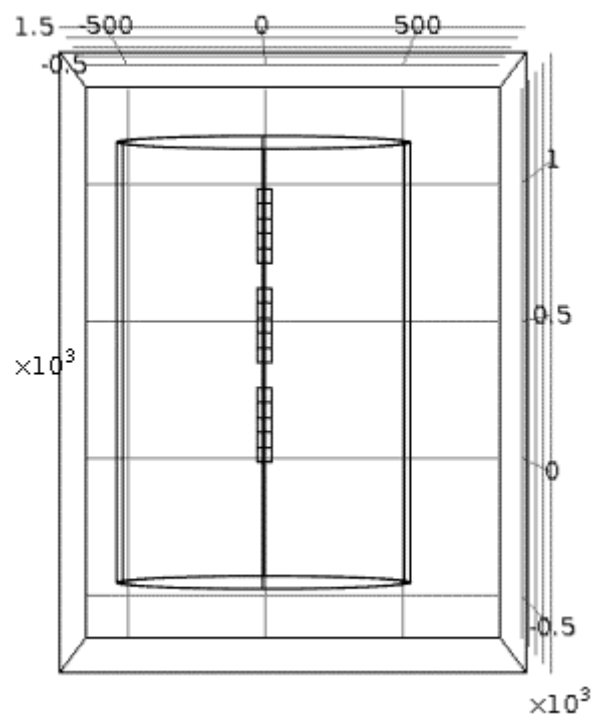
Figure 3.15 Yoke configuration in the vertical direction

The simulation was carried out with one, two and three yokes. The distance between each yoke was 50 mm. Figure 3.16 illustrates the magnetic adhesion force with increasing the number of yokes in the vertical direction where the magnetic adhesion force increases linearly as the number of yokes increase. As a conclusion from the graph shown in Figure 3.14 the adhesion force did not increase linearly as the air gap was not the same for all yokes as Figure 3.16. Consequently, the configuration implemented in Figure 3.16 is better than the configuration in Figure 3.14 regarding the magnet adhesion force. However, only one yoke has been used with the implemented prototype robot (described in chapter 4) as it is small in size and one yoke is sufficient for providing the magnetic adhesion force required.
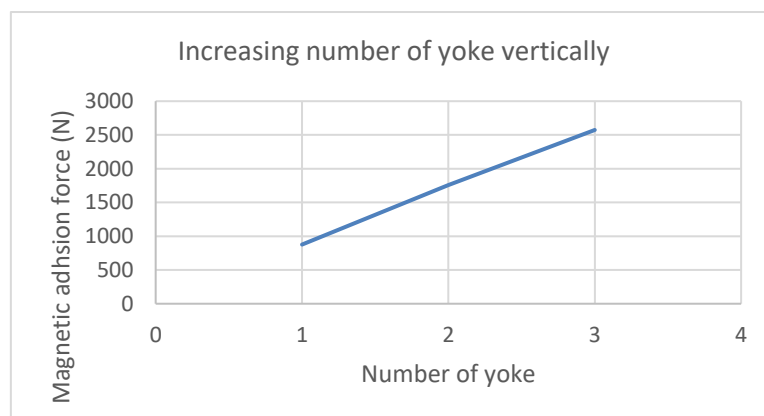
Figure 3.16 Increasing the yokes in the vertical direction

3.7. Test rig

3.7.1. Initial design

A test rig was created to measure the magnetic adhesion force experimentally. The test rig consists of five main parts which are the outer frame, inner frame, aluminium bars, aluminium strips to hold the disc load cells sensors. Figure 3.17 illustrates views of the assembly and rendered image of the test rig. These parts are described in detail in the following sections.
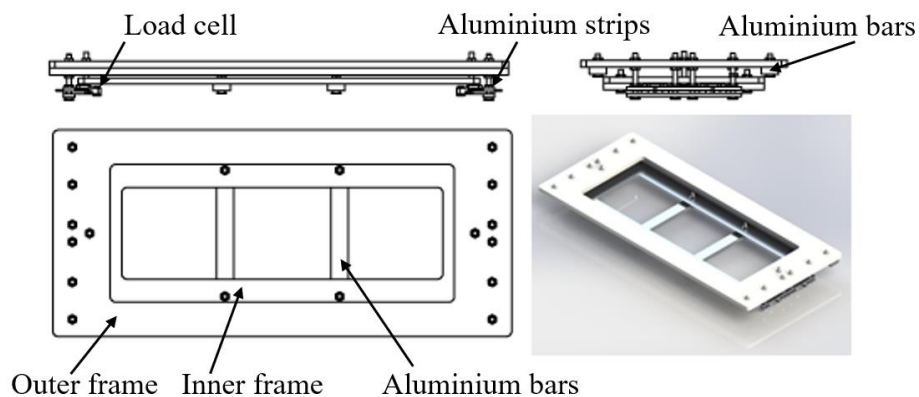
Figure 3.17 Test rig

53

3.7.1.1. The outer frame

The purpose of the outer frame is to hold all components of the test rig. The frame dimensions are 400 × 180 mm. The frame is hollow in the middle to leave space for the magnet to be placed. There are eight holes, four on each side for holding the four load cells (two on each side) as shown in Figure 3.18. In addition, four holes in one each corner are used for fixing two aluminium bars to strengthen the outer frame. Furthermore, there are two holes in the middle of the frame to hold the inner frame.
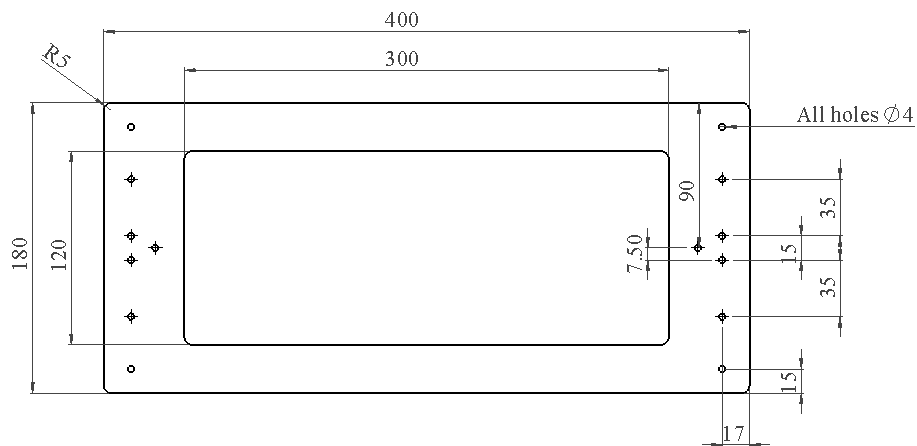
Figure 3.18 Test rig outer frame

3.7.1.2. The inner frame

The inner frame is aluminium and smaller than the outer frame. The inner frame dimensions are 350 × 140 mm to fit under the outer frame to exert a load on the load cells to measure the magnetic adhesion force. The two holes in the left and right border illustrated in Figure 3.19 are used to assemble the inner and outer frame together with two screws. While the other four holes in the top and bottom are utilised for fixing two aluminium bars, so they can carry the yoke.
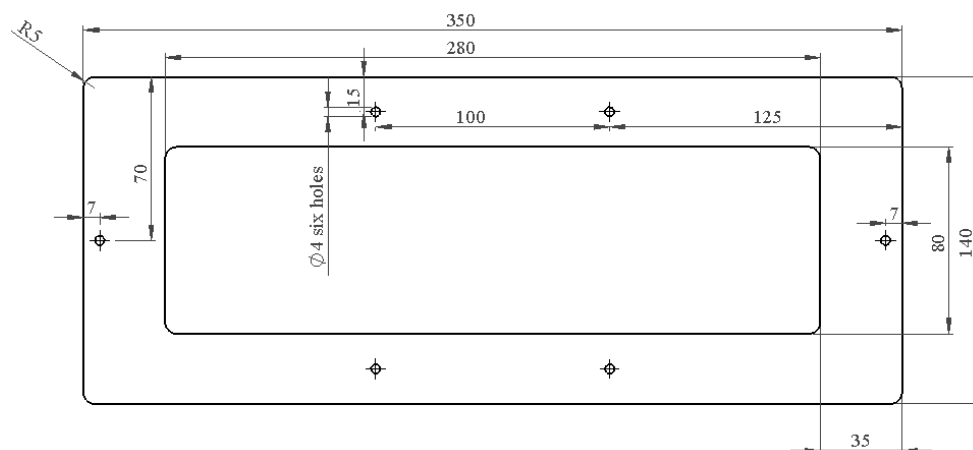
Figure 3.19 The inner frame

3.7.1.3. The aluminium bars

Four aluminium bars with thickness 6 mm are used in the test rig as shown in Figure 3.20. Two identical aluminium bars as shown in Figure 3.20 (a) are assembled with the inner frame to hold the backplate with the magnets to keep a defined air gap between the magnet and the metal sheet placed under the test rig. The other two aluminium bars illustrated in Figure 3.20 (b) are assembled with the outer frame to strengthen it.
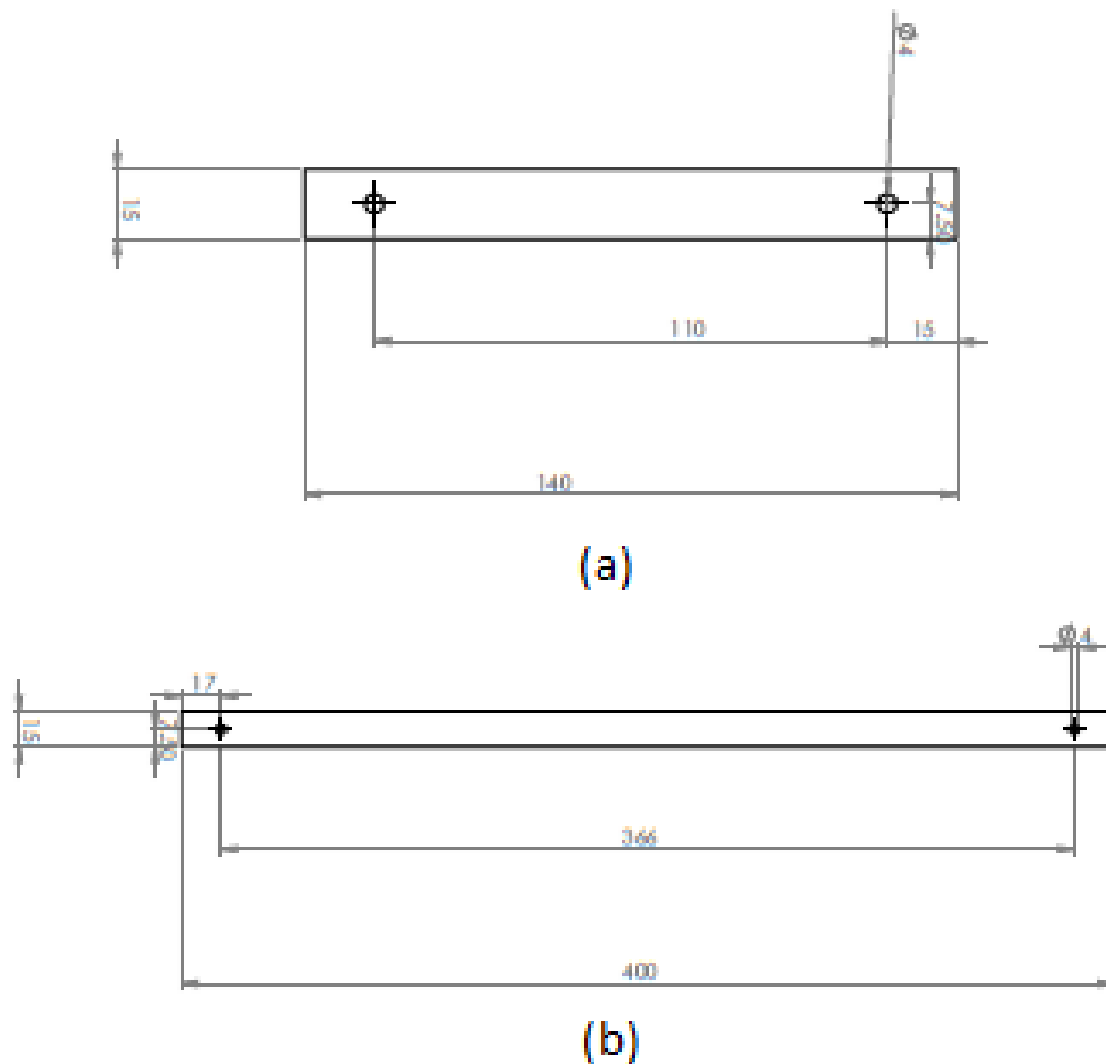
Figure 3.20 The aluminium bars

3.7.1.4. Aluminium strips

Four aluminium strips with thickness 3 mm are used for fixing the load cells as shown in Figure 3.21. Two load cells are placed between two aluminium stripes. Each load cell is placed in the centre between the two holes that the distance between them is 35 mm.
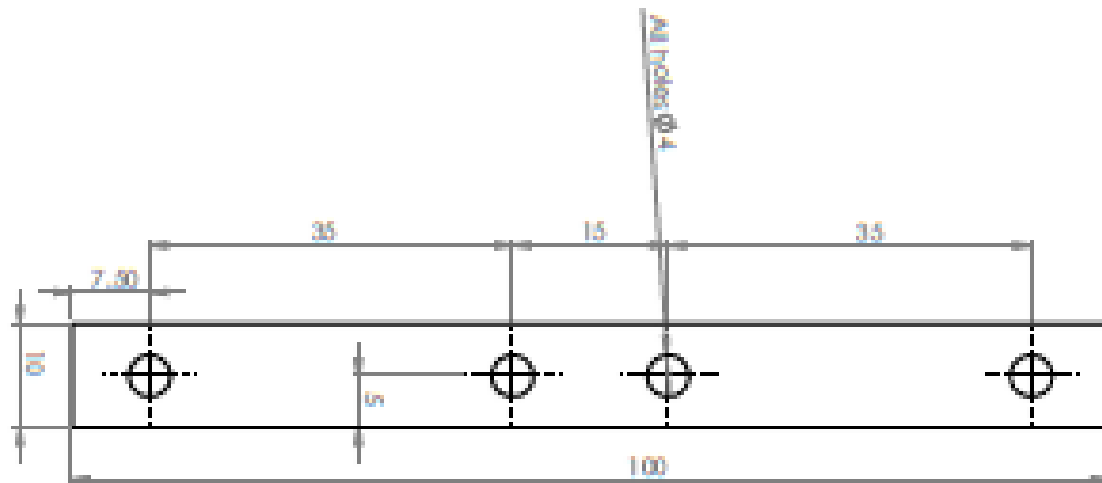
Figure 3.21 Aluminium strips

3.7.1.5. Disc load cell

The disc load cell is a sensor that converts force into an electrical signal. Figure 3.22 illustrates a rendered image of the disc load cell. Four load cells are used for the measurement of the force exerted by a magnet system.

Figure 3.22 Disc load cell

3.7.2. Implementation of initial test rig design

The test rig shown in Figure 3.23 is implemented according to the model described above. The test rig is tested and calibrated with a known weight where it gives acceptable results with a maximum 1% error.

The test rig is operated by placing it on a ferrous metal surface while the magnets with their yoke are placed on the internal frame. The magnets attract the metal surface, so the internal frame exerts force on the load cells. Each load cell creates a signal which is directly proportional to the applied force. The output signal is connected to a weighing scale analogue to digital converter and amplifier module. An Arduino UNO is used to display the average of the four load cell signals on a computer which illustrates the adhesion force in kilograms.

The test rig is used to test the magnetic adhesion force for the available magnets and yoke in the laboratory. The experiment is performed with three magnets with dimensions $50 \times 50 \times 12.5$ mm, yoke with dimensions $5 \times 244 \times 48$ mm and 47 mm distance between magnets. The magnetic adhesion force observed was 138.8 N after deducting the weight of the inner frame and the magnets and yoke.
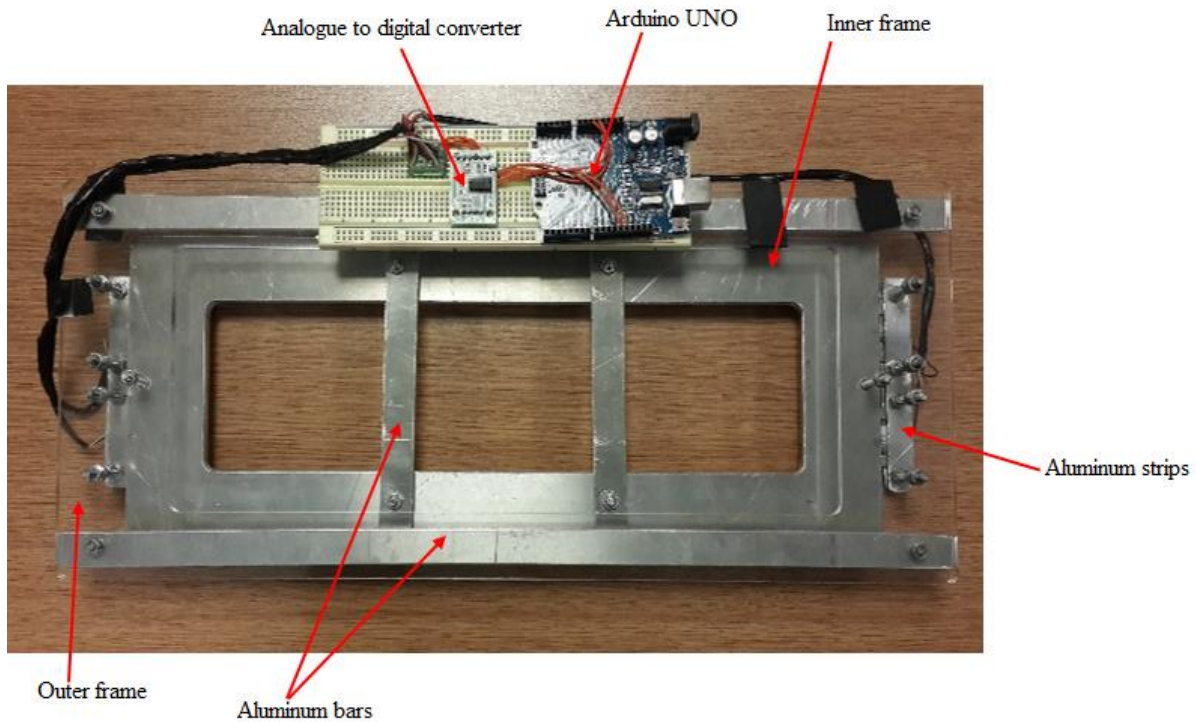
Figure 3.23 Test rig

3.7.3. Initial test rig design observations

While performing the magnetic adhesion force test, it was observed that the internal frame of the test rig bent towards the metal surface due to the strong applied force when the air gap is less than 12 mm. Moreover, this bending is inversely proportional to the air gap between the magnet and the metal surface. Accordingly, a modified test rig was designed to avoid the problems in the old test rig.

3.7.4. Modified design

A modified test rig was designed with stiffer material stainless steel 304 to resist bending. The stainless steel 304 was chosen as it contains chromium and nickel metals and the main non-iron constituents are essentially non-magnetic. Therefore, the stainless steel does not affect the measuring of magnetic adhesion force. The test rig consists of four main parts which are the

outer frame, inner frame, two bars to support the yoke with the magnets and the load cell. Figure 3.24 illustrates views of the assembly and rendered image of the test rig.
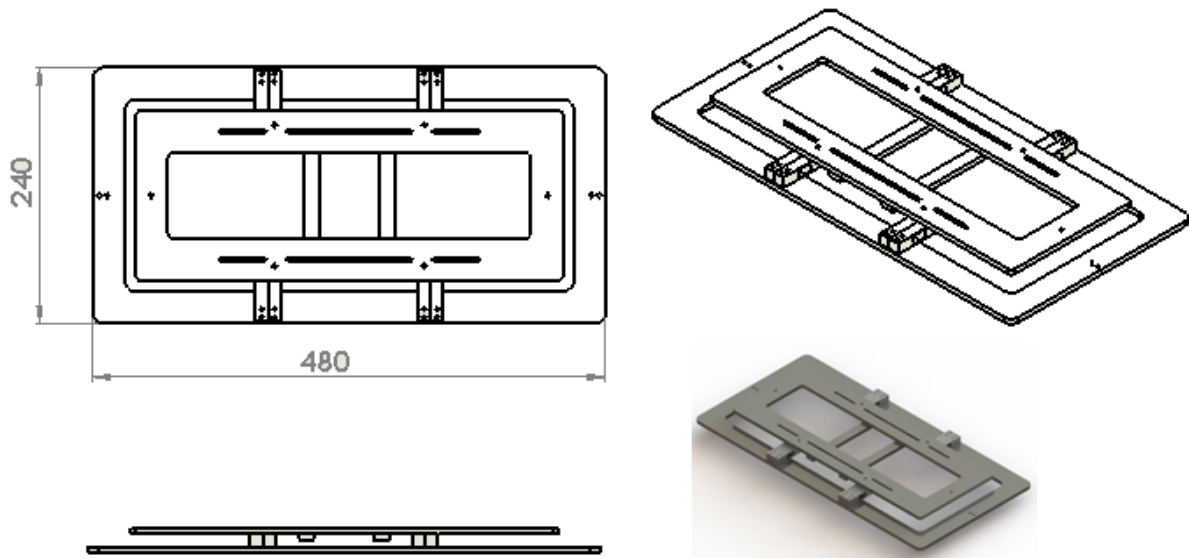
Figure 3.24 New test rig

3.7.4.1. The outer frame

The outer frame is placed directly over the steel carrying all the other components of the test rig. The load cells are fixed in the outer frame and the internal frame with the two bars responsible for holding the yoke and magnets. The frame is hollow in the middle to leave space for the magnets to be placed. The length of the outer frame of the new test rig is longer than the old test rig so it can be used with longer yokes. There are six holes on each side (480 mm side) used for holding the four load cells on each side as shown in Figure 3.25. In addition to four holes (240 mm) on each side can be used for adding more load cells.
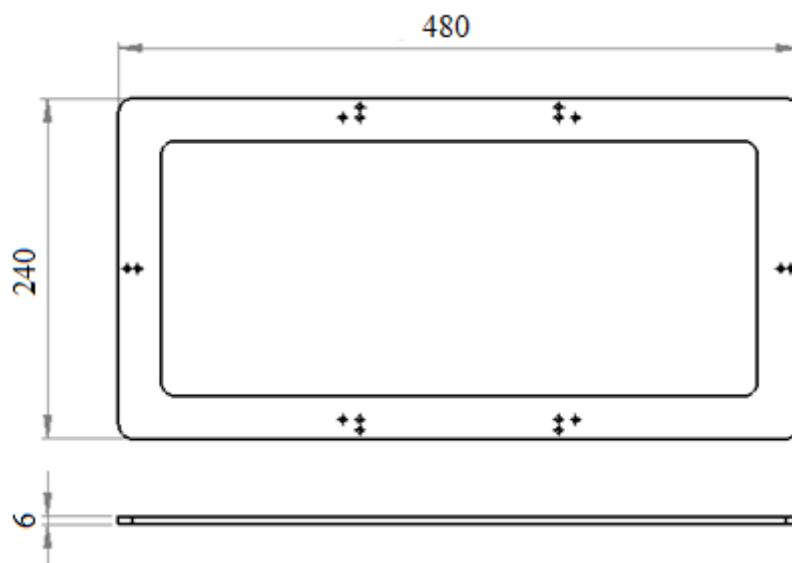
Figure 3.25 New test rig outer frame

3.7.4.2. The inner frame

The inner frame of the new test rig has dimensions 400×160 mm and is smaller than the outer frame. The inner frame is placed over the load cells which are fixed in the outer frame to exert a force on it to measure the magnetic adhesion force. The holes on each side of the inner frame are used to adjust the inner frame with the outer frame together with screws as illustrated in Figure 3.26. The six slots are used to hold the two bars responsible for carrying the yoke with their magnets. Also, the distance between the two bars can be adjusted according to the length of the yoke and distance between magnets where different yoke length and magnet size can be investigated using the same test rig.
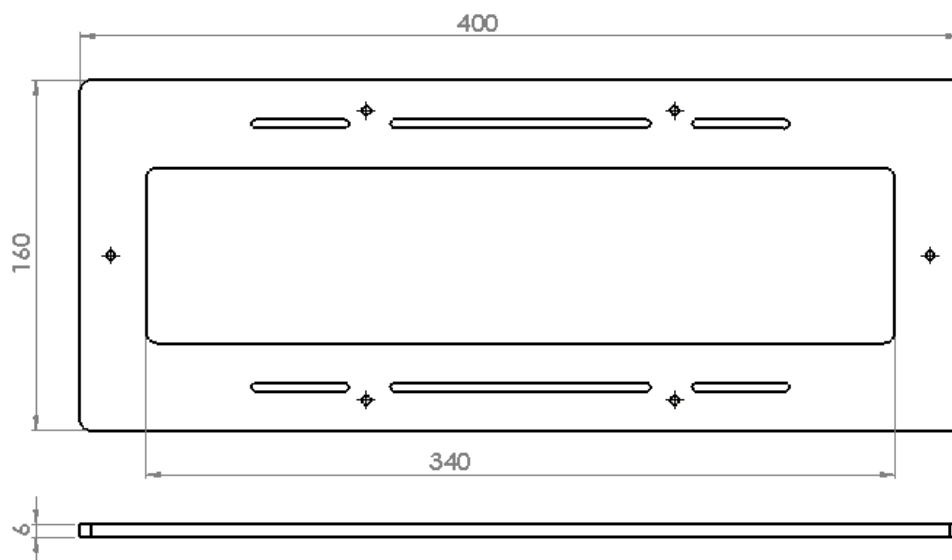
Figure 3.26 The inner frame

3.7.4.3. The stainless steel bars

Two stainless steel bars with dimension 160×15 mm and thickness 6 mm are used in the new test rig as shown in Figure 3.27. Two bars are assembled with the inner frame to hold the backplate with the magnets to keep a defined air gap between the magnet and the metal sheet under the test rig.
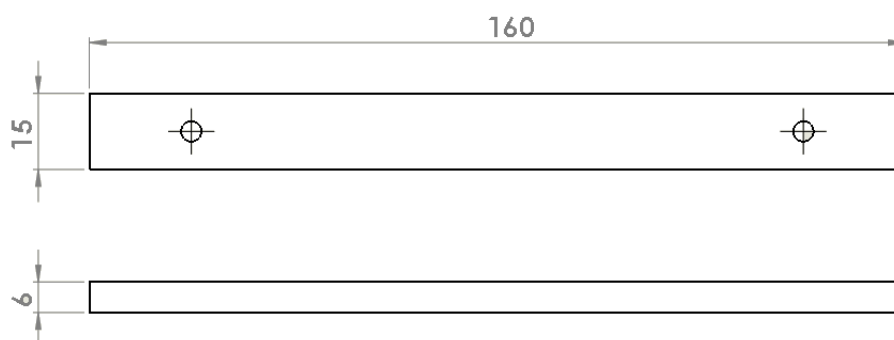
Figure 3.27 The aluminium bars

3.7.4.4. Bending beam load cell

A bending beam load cell sensor is used to convert the force into an electrical signal and to fit with the new test rig design. Figure 3.28 illustrates a rendered image of the load cell.
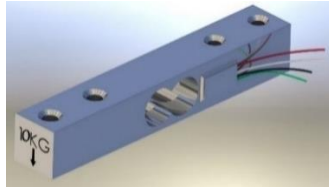
Figure 3.28 Bending beam load cell

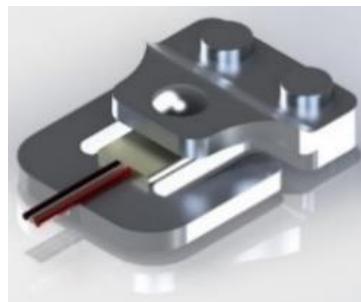### 3.7.5. Implementation of modified test rig design

The new test rig shown in Figure 3.29 is implemented according to the model described in the previous section. The test rig is tested and calibrated with a known weight where it gives acceptable results with a maximum 1% error.

The principle of operation of the test rig is similar to the previous test rig. The measured force is displayed on an LCD screen illustrating the adhesion force in kilograms.

The new test rig has been tested under the same conditions as the old test rig. An experiment was performed with three magnets with dimensions $50 \times 50 \times 12.5$ mm, yoke with dimensions $5 \times 244 \times 48$ mm and 47 mm distance between magnets. The magnetic adhesion force observed was the same as the old test rig results in 138.8 N after deducting the weight of the inner frame and the magnets with the yoke.
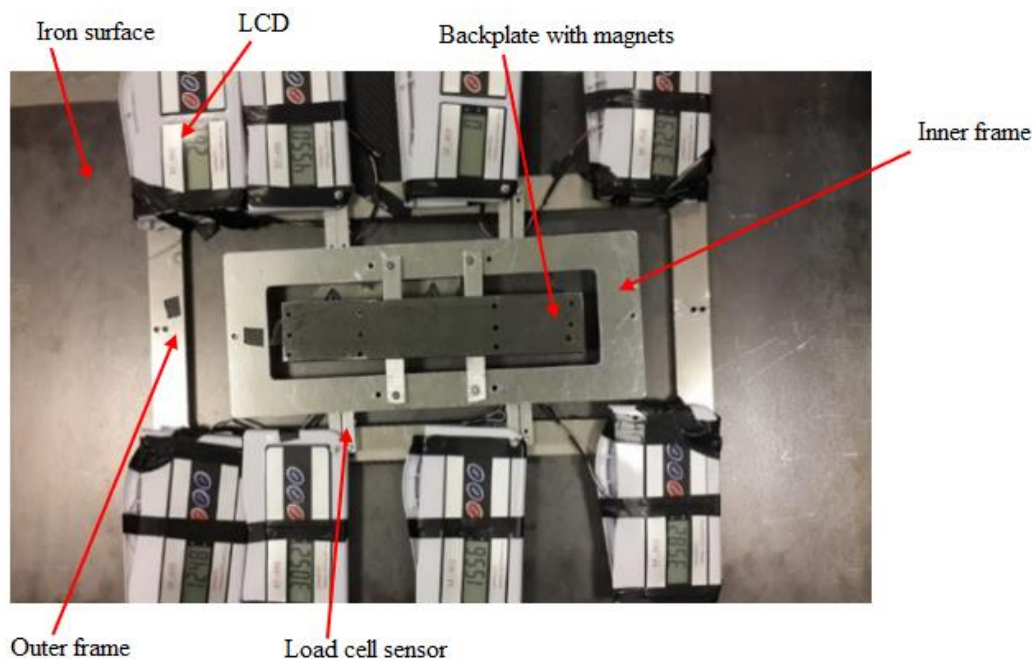
Figure 3.29 New test rig

3.8. Experimental design

The design of experiments using the RSM technique has been implemented to study the different independent parameters affecting the magnetic adhesion force. These parameters are the air gap between the magnet and the adhesion surface, the distance between magnets and yoke thickness.

RSM is a combination of mathematical and statistical techniques for experimental data analysis. It is used to develop a regression model representing the response variable function in specific studied independent parameters. The aim of this model is to represent an empirical relationship between response variables and the independent variables. In addition, it is used to conclude the optimal values of the independent parameters for the specified target of the response variable.

The process of model development using RSM is performed by testing a number of variables in a finite number of experiments. Accordingly, it requires relatively less experimental runs than the conventional methods and hence it decreases the consumption of time and effort.

RSM was used to set up a mathematical relationship between the responses (the magnetic adhesion force) and the factors influencing the adhesion force (air gap, the distance between magnets and yoke thickness). A set of experiments were conducted using the Box-Behnken design (BBD). Each independent parameter is varying between three levels. The three levels are equally spaced and coded as -1, 0, 1 as shown in Table 3.4 and the experiments runs are illustrated in Table 3.5.

Table 3.4 Variables code

Factor	Code	Levels		
		-1	0	+1
Air Gap	A	18	21	24
Distance between magnets	B	20	35	50
Yoke thickness	C	5	10	15

The number of experiments (N) required for the development of BBD is defined as:

$$N = 2k(k-1) + C_o \qquad (3.8)$$

where k is the number of factors and C_o is the number of central points. In this design, three factors have been studied (k=3) and 5 replicates of the centre points have been considered (default number of centre points recommended for BBD) [98].

Table 3.5 Design of experiments matrix coded variables and experimental responses

No. of exp.	Std order	Run order	Factor 1	Factor 2	Factor 3	Response 1	
			A: Air Gap (mm)	B: Distance between Magnets (mm)	C: Yoke Thickness (mm)	Actual Force (kg)	Predicted Force (kg)
1	4	1	24	50	10	17.035	16.21
2	7	2	18	35	15	29.426	29.08
3	14	3	21	35	10	19.936	21.15
4	15	4	21	35	10	22.063	21.15
5	16	5	21	35	10	22.169	21.15
6	5	6	18	35	5	22.575	22.59
7	8	7	24	35	15	16.675	16.66
8	1	8	18	20	10	24.525	25.35
9	17	9	21	35	10	20.542	21.15
10	2	10	24	20	10	14.633	15.12
11	10	11	21	50	5	17.072	17.54
12	3	12	18	50	10	29.227	28.74
13	9	13	21	20	5	16.872	16.03
14	11	14	21	20	15	21.212	20.74
15	13	15	21	35	10	21.062	21.15
16	12	16	21	50	15	22.872	23.71
17	6	17	24	35	5	11.915	12.26

3.8.1. Statistical analysis

The three independent variables can be approximated by the second-order polynomial model as shown below:

$$Y = b_o + \sum_{i=1}^{n} b_i x_i + \sum_{i=1}^{n} b_{ii} x_i^2 + \sum_{i=1}^{j-1}\sum_{j=2}^{n} b_{ij} x_i x_j + \varepsilon \qquad (3.9)$$

Where Y is the corresponding response, b_i, b_{ii} and b_{ij} represent the linear, quadratic and interactive coefficients, respectively. b_o represent the constant coefficient and ε is the residual experimental error and X_i, X_j are coded values of the input parameters.

The model adequacy has been checked by the coefficient of correlation (R^2), adjusted coefficient of determination (R^2_{adj}) and the predicted coefficient of determination (R^2_{pred}). Investigation of the statistical significance has been analysed using Analysis of Variance (ANOVA) by calculating the Fisher's F-test at 95% confidence level.

F-tests are named after its test statistic, F, which was named in honour of Sir Ronald Fisher. The F-statistic is simply a ratio of two variances. Variances are a measure of dispersion, or how far the data are scattered from the mean. Larger values represent greater dispersion [99].

Lack of fit analysis has been used to measure the failure of the developed model to fit the experimental data. The non-significance of the lack of fit value concludes the successful fitting of the model for the experimental data.

The design of expert software has been used for the optimisation, regression analysis and graphical representation. Statistical significance of the results has been presented by p-value where the result is significant when $p < 0.05$.

P-value is defined as the probability of obtaining the observed results of a test, assuming that the null hypothesis is correct. A smaller p-value means that there is stronger evidence in favour of the alternative hypothesis. A smaller p-value means that there is stronger evidence in favour of the alternative hypothesis. P-values are calculated using p-value tables or spreadsheets/statistical software [100].

3.8.2. Model validation and adequacy checking

Using the experimental results concluded for the 17 runs as shown in Table 3.5, a quadratic regression equation has been developed representing an empirical relationship between the response variable and all the independent variables.

$$Y = 21.15 - 5.69\,A + 1.12\,B + 2.72\,C - 0.57\,AB - 0.52\,AC + 0.36\,BC + 0.42\,A^2 - 0.22\,B^2 - 1.43\,C^2 \tag{3.10}$$

Where Y represents the magnetic adhesion force, A, B and C represent air gap, distance between magnets and yoke thickness, respectively.

ANOVA has been applied to validate the developed model where it concluded an F-value of 34.59 and p-value of <0.0001, as shown in Table 3.6. These results indicate that the model is highly statistically significant with 95% confidence level. In addition, the lack of fit analysis concluded p-value of 0.363, which indicates the non-significance of the test. These results conclude that the model successfully represents the experimental data. The determination coefficients, R^2 and R^2_{adj}, have been calculated as 0.978 and 0.950, respectively. Accordingly, these values illustrate that only 0.022 of the total variation is not well explained by the developed model. The similarity between the predicted and experimental values are shown in Table 3.5 which demonstrates the adequacy of the model. Figure 3.30 illustrates the agreement between actual data versus predicted values by the model.
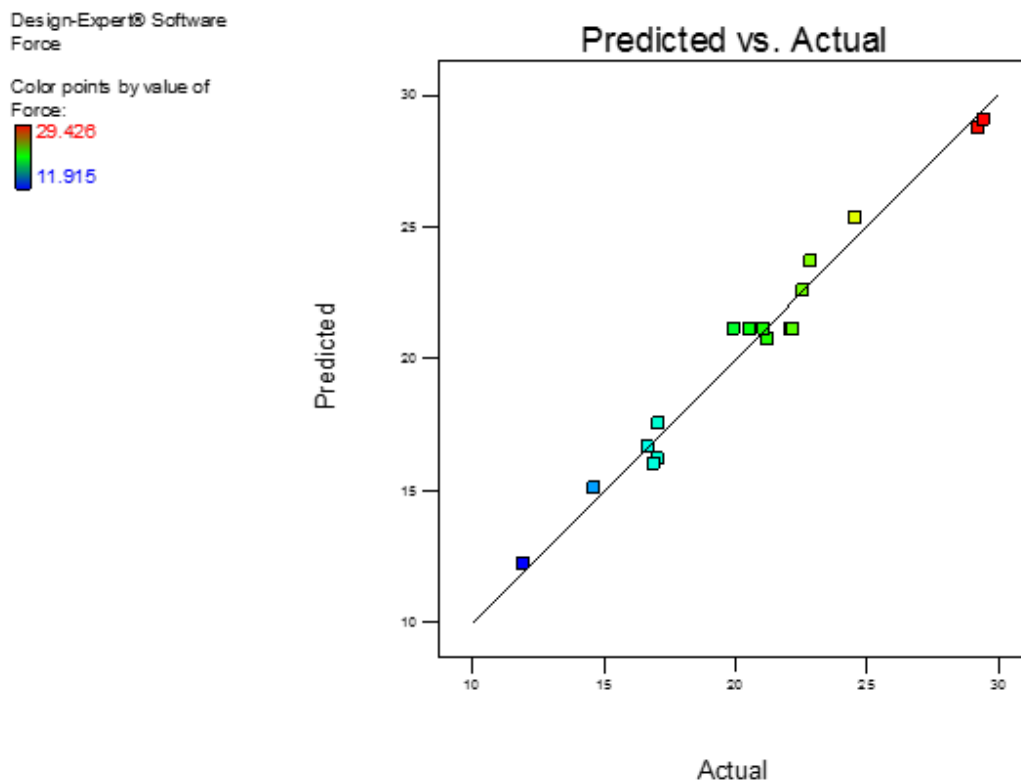
Figure 3.30 Predicted values developed by the model versus actual experimental data

3.8.3. Effect of Process Variables

The 3D-surface and contour plots of the adhesion force versus interaction of two independent variables are shown in Figure 3.31–Figure 3.34. In each plot, the remaining independent variables are kept constant in their centre points. Table 3.6 represents the analysis of variance (ANOVA) determined from the developed model.

3.8.3.1. Effect of Air Gap

Experimental runs were carried out at air gap range from 18 to 24 to study its effect on the adhesion force. Based on the ANOVA results shown in Table 3.6, air gap parameter shows the highly significant effect on the process response with p-value <0.0001 and F-value 236.71. Figure 3.31 and Figure 3.32 illustrates the effect of air gap and distance between magnets versus magnetic adhesion force where while increasing the air gap, the adhesion force decreases.

Table 3.6 Analysis of variance (ANOVA) for response surface developed model

Source	Sum of Squares	df	Mean Square	F Value	p-value Prob > F	
Model	340.26	9	37.81	34.59	< 0.0001	significant
A-Air Gap	258.72	1	258.72	236.71	< 0.0001	
B-Distance between Magnets	10.04	1	10.04	9.19	0.0191	
C-Yoke Thickness	59.14	1	59.14	54.11	0.0002	
AB	1.32	1	1.32	1.21	0.3077	
AC	1.09	1	1.09	1	0.3506	
BC	0.53	1	0.53	0.49	0.5075	
A^2	0.75	1	0.75	0.68	0.4362	
B^2	0.2	1	0.2	0.19	0.6788	
C^2	8.58	1	8.58	7.85	0.0265	
Residual	7.65	7	1.09			
Lack of Fit	3.93	3	1.31	1.41	0.3636	not significant
Pure Error	3.72	4	0.93			
Cor Total	347.91	16				

3.8.3.2. Effect of Distance between Magnets

It is clearly shown in Figure 3.31 and Figure 3.32 that while increasing the distance between magnets, the adhesion force increases. The figures show that the effect of distance between magnets on adhesion forces varies according to the value of the air gap which confirms the insignificance effect of interaction between different independent variables on the process

response. These results have been confirmed. The distance between magnets showed a highly significant effect on the response with a p-value of 0.0191 and F-value of 9.19 using ANOVA as illustrated in Table 3.6.
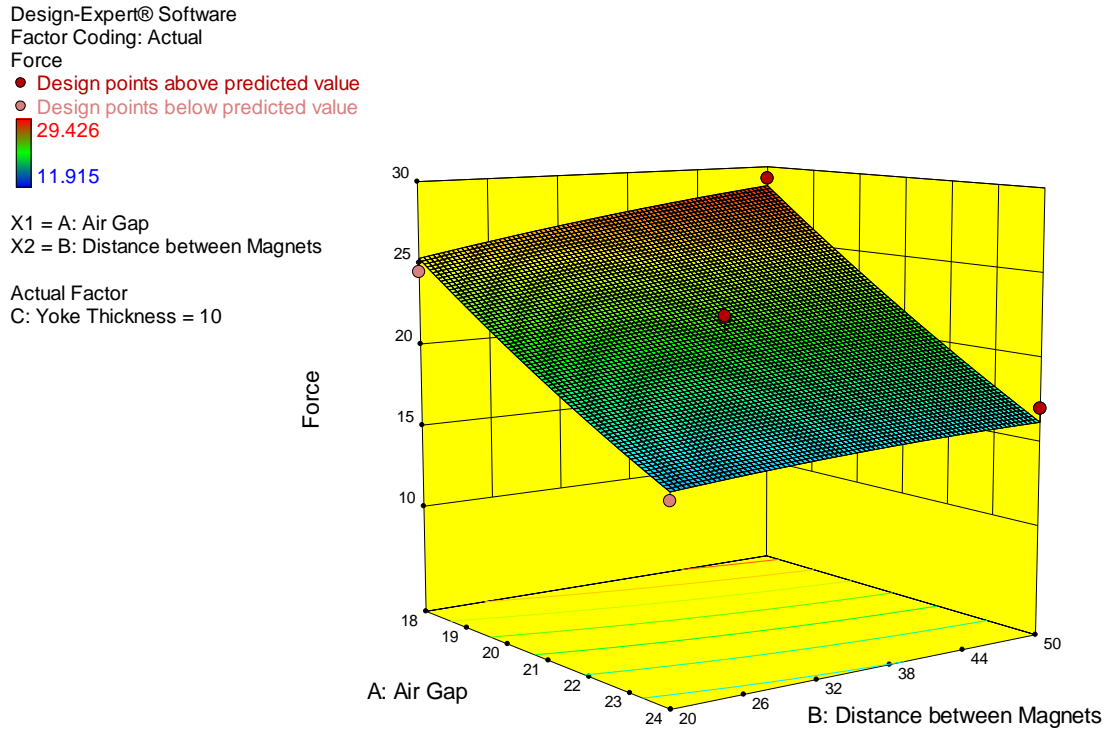
Figure 3.31 3D surface plot for air gap and distance between magnets versus magnetic adhesion force
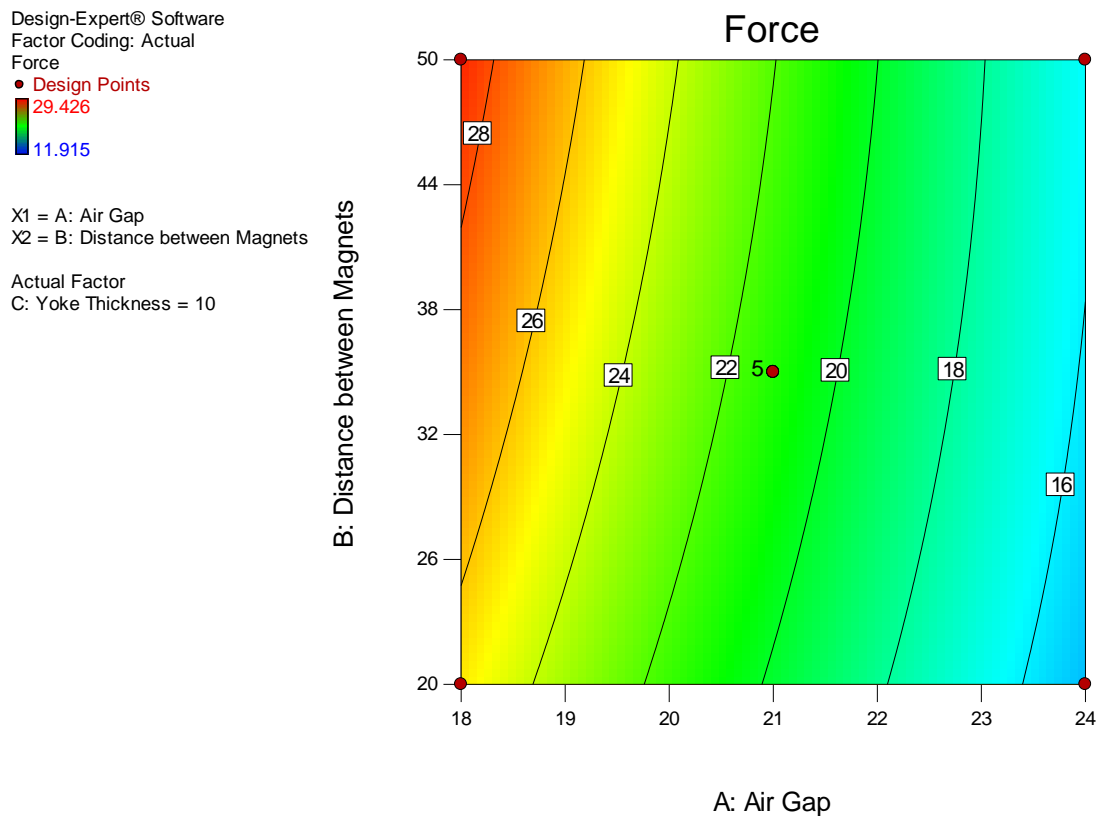
Figure 3.32 Contour graph for air gap and distance between magnets versus magnetic adhesion force

3.8.3.3. Effect of Yoke Thickness

The thickness of a yoke attached to the magnets has a considerable effect on the adhesion force. ANOVA results in Table 3.6 showed the highly significant effect on the response variable where it has concluded p-value and F-value of 0.0002 and 54.11, respectively. Figure 3.33 and Figure 3.34 represents the single and interaction effects of yoke thickness and distance between magnets on the process response. It is clearly shown in the figure that the adhesion force has an increasing effect with increasing yoke thickness where the relationship has been concluded.

3.8.4. Optimisation of process variables

The optimisation process of the independent parameters has been performed to conclude the maximum adhesion force at the minimal affecting variables i.e. air gap, the distance between magnets, yoke thickness.

Numerical optimisation has been performed by combining the desirability of process variables into a single value to find the optimal values at the specified targeted goals. Specific targets have been inserted into the software to guide the optimisation process. The response variable i.e. adhesion force has been set to a maximum. The yoke thickness has been targeted to be minimised to reduce the weight of the climbing robot. Air gap variable has been set to be minimum as it has the most significant effect on the adhesion force also to avoid the turnover of the robot. Finally, the distance between magnets has been minimised with lower importance as it has a reflection on the length of the yoke.

The maximum adhesion force that can be concluded from the optimisation process according to the constraints mentioned above was 24 kg at air gap, the distance between magnets and yoke thickness of 18 mm, 21.7 mm and 7.79 mm, respectively.
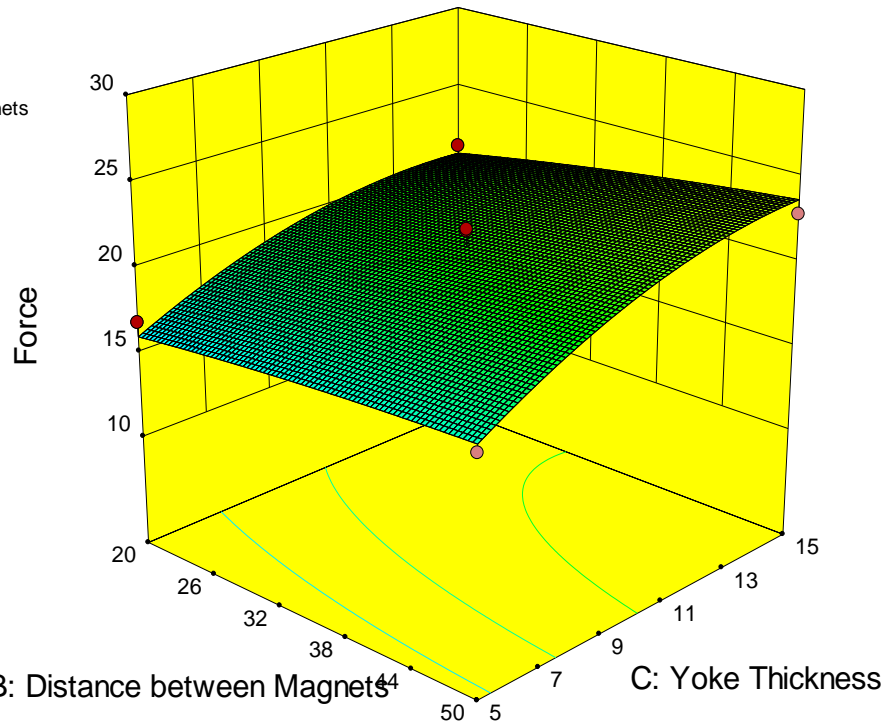
Figure 3.33 3D surface plot for yoke thickness and distance between magnets versus magnetic adhesion force
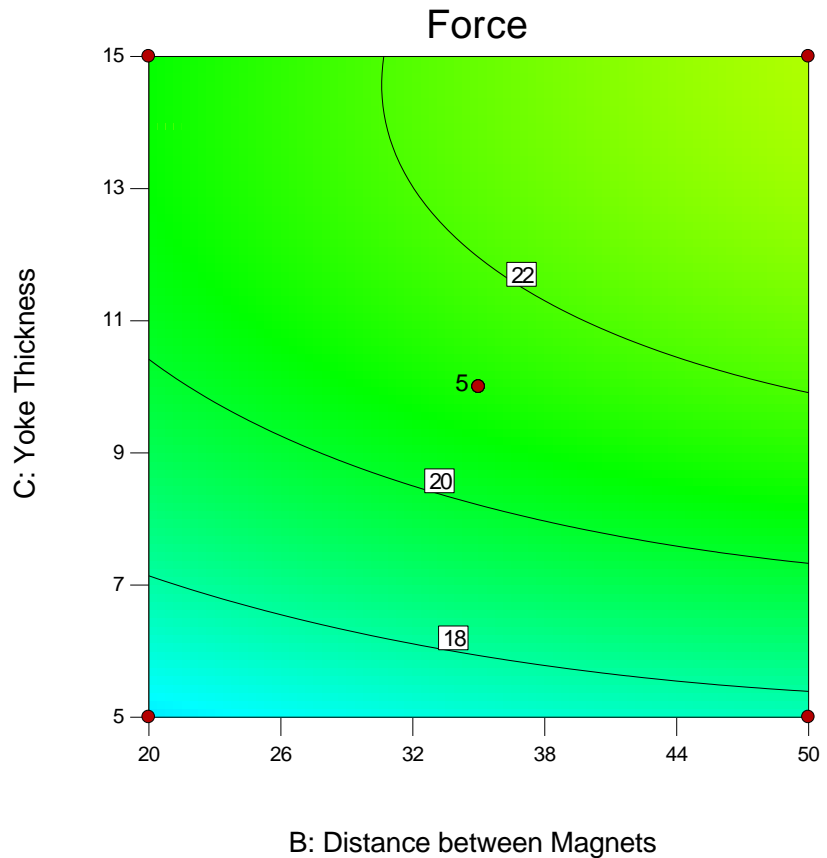
Figure 3.34 Contour graph for yoke thickness and distance between magnets versus magnetic adhesion force

3.9.   Chapter summary

RSM has been used to design experiments and investigate the effect of independent variables (air gap, the distance between magnets, yoke thickness), on the process response (magnetic adhesion force). A quadratic polynomial model has been obtained for the response variable function in all independent variables. Optimum conditions have been concluded from the quadratic polynomial model for adhesion force. The maximum adhesion force observed was 24 kg at an air gap of 18 mm, the distance between magnets of 21.7 mm and yoke thickness of 7.79 mm.

Seventeen experiments were conducted for air gaps between 18-24 mm, yoke thickness between 5-15 mm and distance between magnets of 20-50 mm. Experimental and statistical validation has been applied for the predicted model resulting in a high agreement between response values. The average relative error between the tested experimental values and predicted values using the quadratic polynomial model was 0.95%.

Chapter 4

Design of a prototype climbing robot

4.1. Introduction

In this chapter, the design and implementation of a scaled-down prototype magnetic climbing robot are developed that can be used for WT blade inspection. The robot is equipped with two arms that can be extended to one-meter length to come close to the blade for inspection. Each arm is equipped with a gripper that can hold an NDT inspection tool of weight up to one kilogram.

4.2. Design requirements

The scope of this research is the design, manufacture and development of a mobile robot for NDT inspection of wind turbine blades. The challenges to be met are many and complicated therefore the development process is long. The most important design considerations, which had to be met, were:

1. The robot should have the ability to work for an extended time. The robot must be capable of completing the inspection of wind turbine blades in one working day.
2. One of the most important issues is the inspection tools that the robot can carry. The robot should have the ability to carry a payload of 50 kg at the end of the inspecting arm allowing the use of radiography i.e. X-ray source and detector. The design requirement for the prototype payload is 1 kg in each arm.
3. The design and development of a secure and stable robot should avoid any hazard possibility for the personnel and the wind turbine structure.
4. The robot should have sufficient degrees of freedom to enable compound motion patterns.
5. Achieve the design of a lightweight structure so that the robot can perform the whole inspection without the need to be hanged from the nacelle of the wind turbine.
6. The robot arm should be able to move on strongly curved surfaces and perform NDT inspection. Additionally, these curved surfaces could be of positive or negative curvature.

7. The robot should have the ability to reach close to the leading and trailing edges in order to inspect them.

8. Maximum possible coverage of the blade surface.

9. Implementation of a positioning system in order to enable position monitoring during the inspection process.

10. There is no product commercially available in the market, but the design here attempts to develop a low-cost product that is affordable for wind turbine operators.

In this chapter, the detailed description of the design will be presented taking into consideration all the above-mentioned points.

4.3. Preliminary development of the wall climbing robot

The wall climbing robot was designed with wheels as a locomotion technique to provide the robot with continuous motion and the permanent magnet adhesion principle to adhere to the WT tower. The robot consists of seven parts which are the chassis, wheels, motors, motor coupler, motor bracket, yoke and magnets. Figure 4.1 illustrates the drawing of the wall climbing robot.
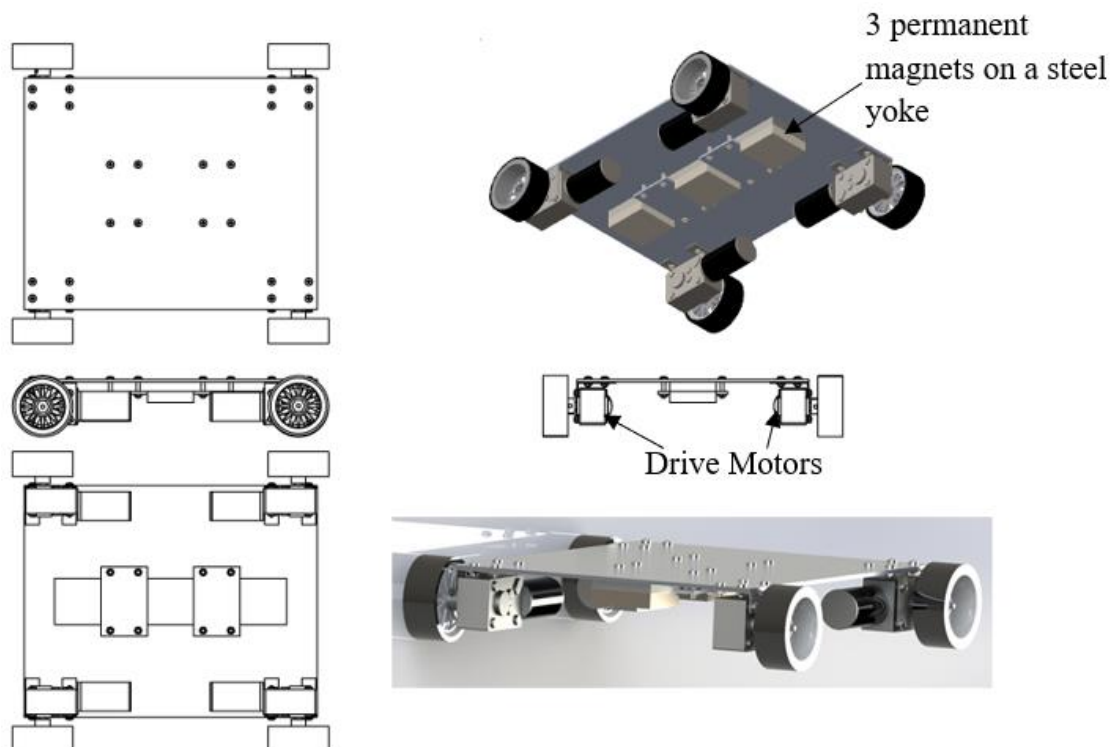
Figure 4.1 Wall climbing robot

4.3.1. Robot chassis

The robot chassis is an aluminium plate with dimension 316 × 240 mm and thickness 3 mm. The length of the chassis dimension has been chosen according to the length of the motor in addition to a proper distance for motor connections. While the width is chosen to keep the motor away from the magnetic flux region in order not to affect the operation of the motor taking into consideration the curvature of the tower. The material of the robot is aluminium to have a lightweight structure. The four holes in each corner of the chassis shown in Figure 4.2 are for fixing the motor bracket. In addition, the eight holes in the middle are used to fix the yoke.
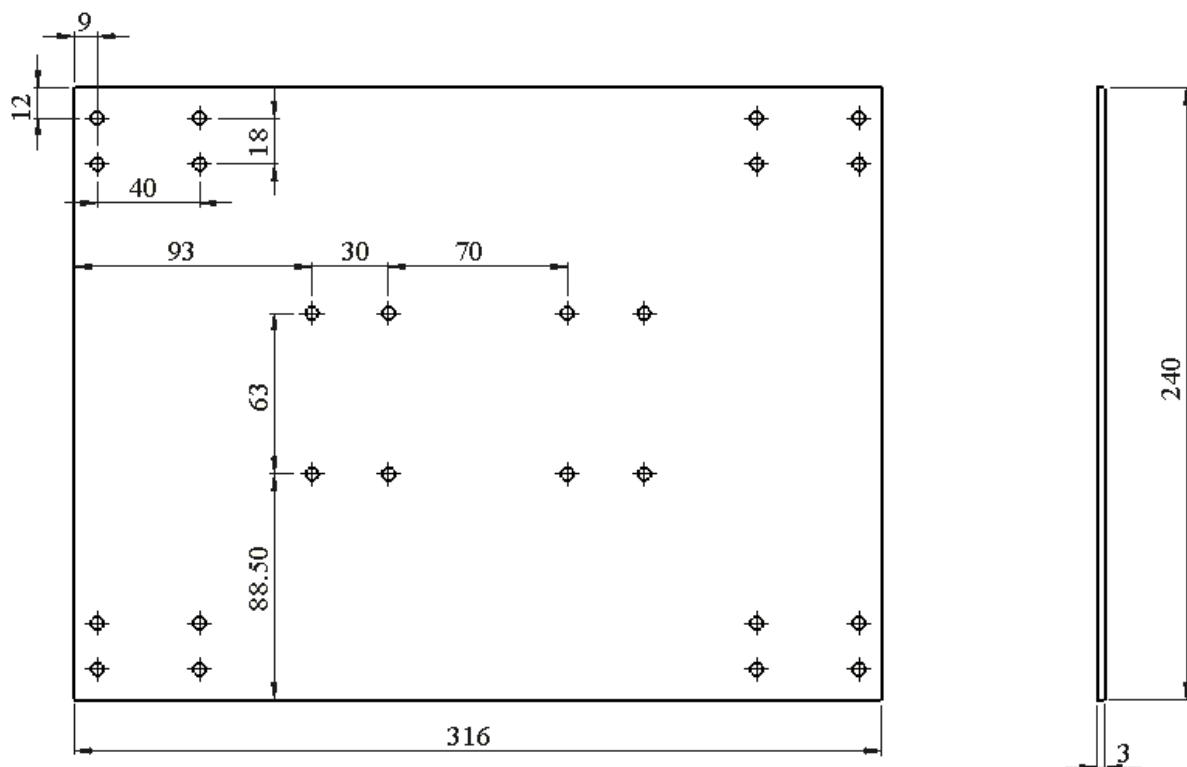
Figure 4.2 Robot chassis

4.3.2. Driving wheels

The mechanical system utilises four wheels of the same type rim ANSMANN as shown in Figure 4.3. The wheels are made of plastic and 2.3″ diameter with rubber as traction material.
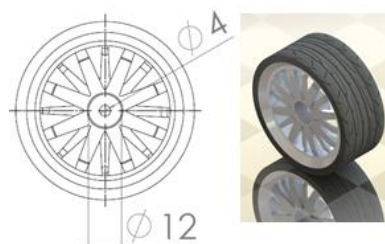
Figure 4.3 Wheel

4.3.3. Motors

The robot is equipped with four DC motors with worm gearboxes shown in Figure 4.4. The motors are fixed in line with the corner of the chassis to give the robot the ability to transfer from one plane to another.
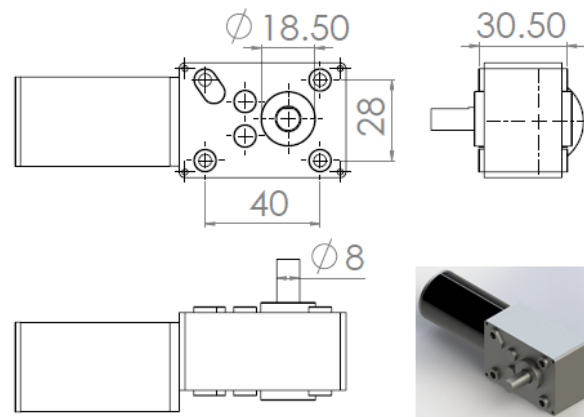
Figure 4.4 Motor

4.3.4. Motor coupler

To transfer the power of the motor to the wheel a motor coupler is designed to connect the shaft of the motor to the wheel as shown in Figure 4.5. The motor coupler is designed with three different diameters. The M4 bolt is to fit inside the hole of the wheel to be tied by hex nut from the other side. The 11.9 mm diameter protrusion fits inside the 12 mm hole shown in Figure 4.3. The 16 mm diameter shaft gives enough thickness for the threading of the grub screw M4 to attach the coupler to the 8 mm motor shaft shown in Figure 4.4.
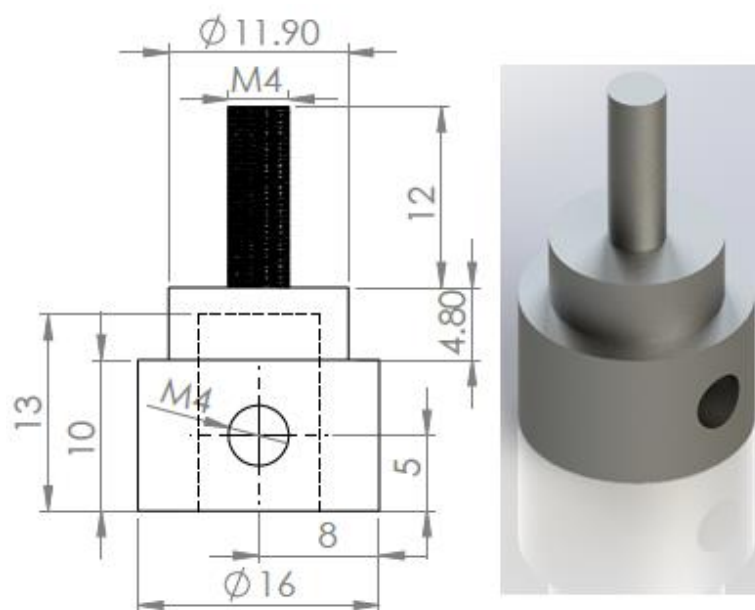
Figure 4.5 Motor coupler

4.3.5.   Motor bracket

The motors are attached to the chassis with L-shape steel brackets. Each motor is attached with two L-shaped steel brackets different in length as shown in Figure 4.6. The long L-shape motor bracket is used to fix the motor from the left side while the short L-shape from right in order not to interfere with the 18.5 mm diameter as shown in Figure 4.4.
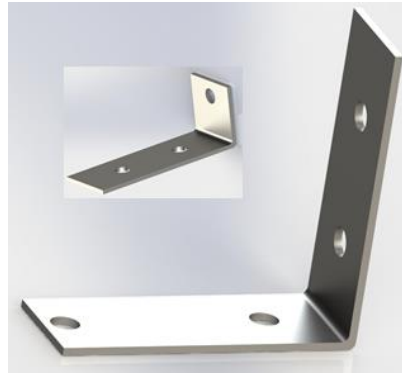
Figure 4.6 Motor bracket

4.3.6.   Yoke and magnets

The yoke and magnets are attached to the robot chassis in the middle by eight machine screws fastened with the aluminium plate placed in the region between magnets. The backplate is iron with dimension $50 \times 250 \times 11$ mm as shown in Figure 4.7. Three neodymium magnets are attached to the yoke. The dimension of each magnet is $50 \times 50 \times 12.5$ mm and the distance between magnets is 50 mm.
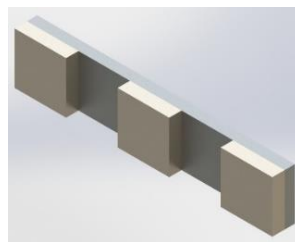
Figure 4.7 Yoke with magnets

4.4.   Robot implementation and test of preliminary design

The robot is implemented according to the model described in the previous section 4.3 and tested in the laboratory on a cylindrical barrel with a diameter 1 m as shown in Figure 4.8. The air gap between the magnets and the barrel was found to be 11 mm.
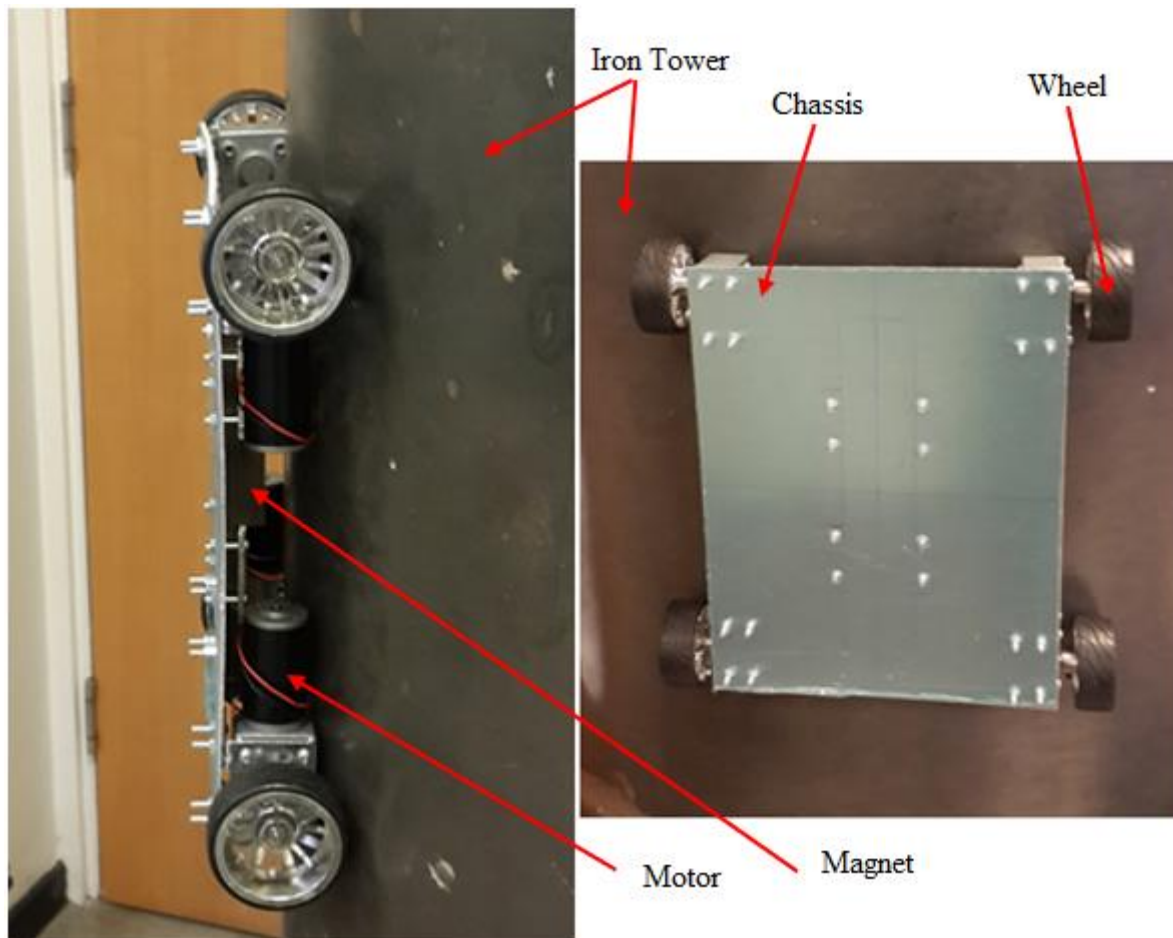
Figure 4.8 Robot implementation

4.5.   Preliminary robot design observations

During testing the wall climbing robot on the barrel some technical issues were observed in the robot design in the following components: wheel, coupler and chassis.

4.5.1.   Wheels

It has been observed that the four wheels are not fully touching the surface of the barrel due to its curvature. Consequently, the design of the motor bracket (L-shape), used in fixing the motor with the chassis, should be modified to be with a certain angle to make the wheel perpendicular to the surface according to the diameter of the turbine tower.

4.5.2.   Motor Coupler

Two problems have been observed in the motor coupler design. The first one is that the length of the coupler is not long enough to leave a distance between the wheel and the machine screw fixing the motor to the motor bracket. This problem was tackled by connecting the coupler

from the other face of the wheel as shown in Figure 4.9 left side. The second problem is that the torque of the motor does not transfer to the wheels as the coupler has a circular end which is in contact with the wheel. Accordingly, the coupler slips inside the wheel obstructing the probability of motion. As a result, the design of the coupler was modified to be with a hexagonal end, based on the internal shape of the wheel as shown in Figure 4.9 right side.
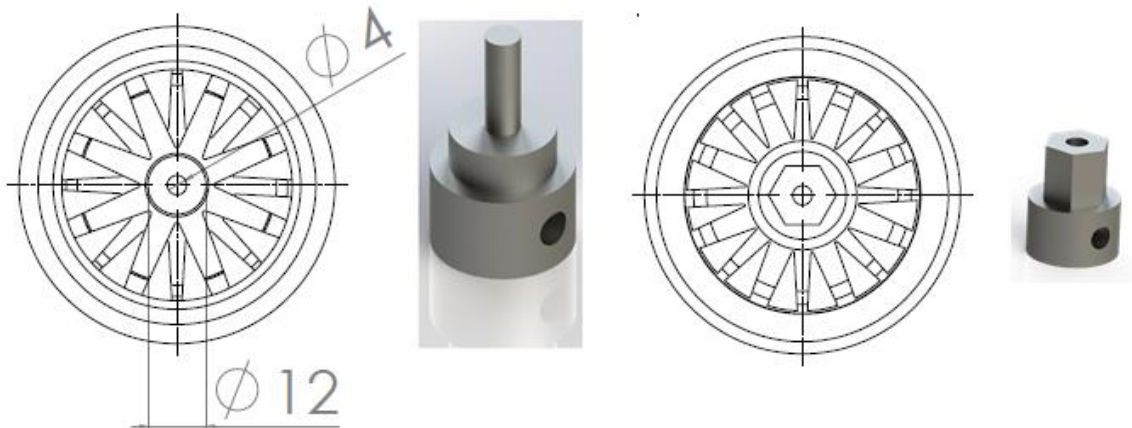
Figure 4.9 Coupler design

4.5.3. Chassis

Due to the strong adhesion force of the magnet system, a slight bending has been observed on the robot chassis towards the barrel. This bend is due to using an aluminium sheet of thickness 3 mm which is not capable of withstanding the adhesion force. So, the thickness of the chassis should be more than 3 mm.

4.6. The final design of the wall climbing robot

The final design of wall climbing robot has been modelled by taking into consideration the problems that arose in the first version. The robot was designed to provide the robot with continuous motion while using permanent magnets for the adhesion principle to adhere to the WT tower. The chassis of the robot is now based on aluminium profile 2020 as illustrated in Figure 4.10 instead of aluminium plate 316×240 mm with thickness 3 mm. The reason for using this type of aluminium extrusion is that it enables fast design and manufacturing of structural frames.
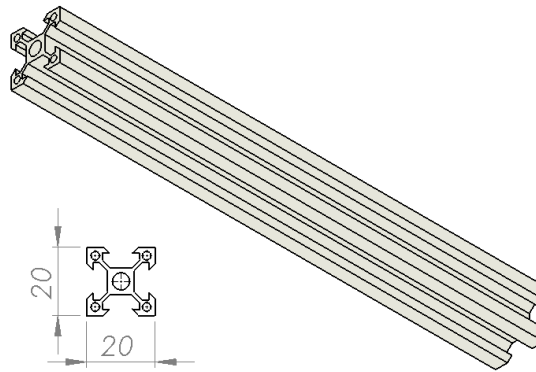
Figure 4.10 Aluminium profile 2020

The robot comprises of seven parts; which are the chassis, wheels, motors, motor coupler, motor bracket, yoke and magnets.

The robot rectangular chassis base consists of four bars of aluminium profile 2020 with dimension 290 × 110 mm as shown in Figure 4.11. The length of the chassis dimension has been chosen according to the length of the motor in addition to a proper distance for motor connections. The width is chosen to keep the motor away from the magnetic flux region in order not to affect the operation of the motor. Each of the two aluminium profile bars in the base of the chassis is connected using one aluminium external 3D joint 2020 as shown in Figure 4.12 and one aluminium internal joint 2020 as shown in Figure 4.13.

Figure 4.11 Robot chassis

Figure 4.12 3D joint 2020

Figure 4.13 Internal joint 2020

The chassis has been supported with two aluminium profile 2040 bars for holding the magnet. A low permeability iron yoke and rare-earth permanent magnets are attached to the robot

chassis in the middle by two aluminium plates and eight machine screws and T-nuts with aluminium profile 2040 as shown in Figure 4.14. The yoke (backplate) is iron with dimension $50\times250\times11$ mm. Three rare earth neodymium N35 magnets are attached to the yoke in an optimum configuration to give maximum adhesion force. The dimension of each magnet is $50\times50\times12.5$ mm and the distance between magnets is 50 mm.
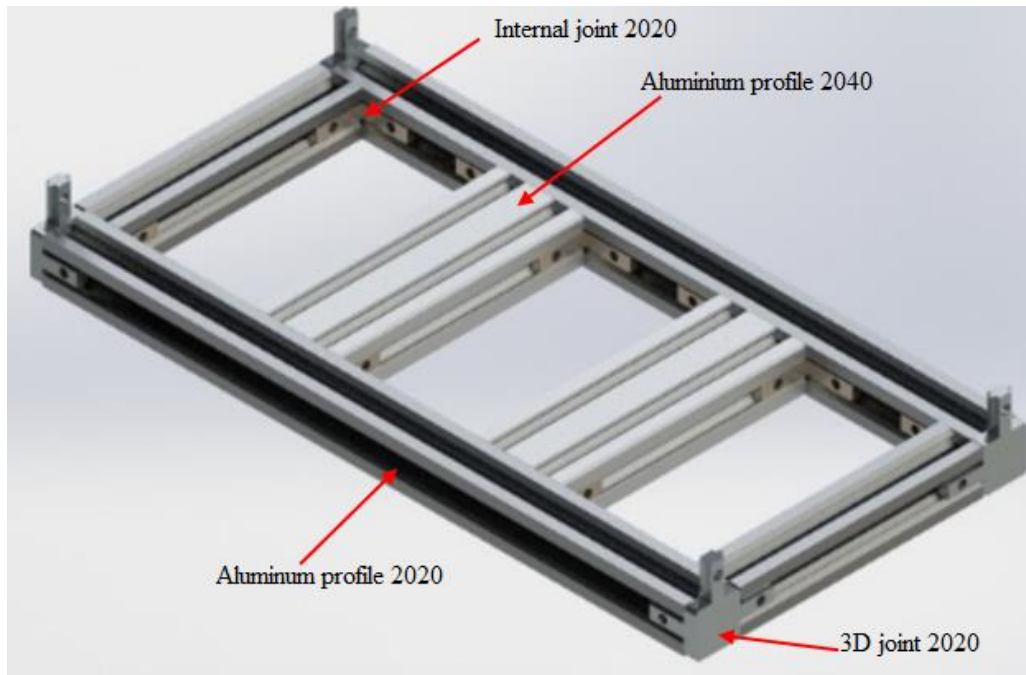
Figure 4.14 Robot base

The wheel of the robot has been installed using the same aluminium profile. Each wheel is driven by a DC motor. The motor is fixed in an aluminium profile 2040 bar of length 70 mm with a steel bracket as shown in Figure 4.15. The aluminium profile 2040 with motor is fixed using a hinge 2020 with the chassis base. The hinge is fixed at the bottom of the base to give the wheel the freedom of adjusting itself over the wind turbine tower curvature.
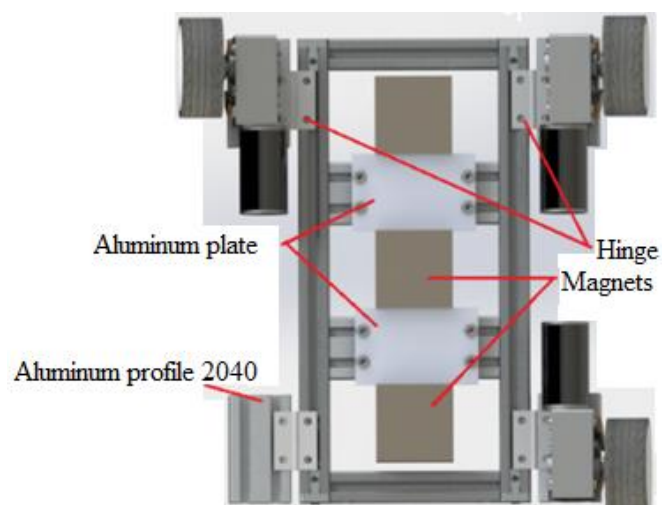
Figure 4.15 Chassis base

In order to limit the motion of the hinge holding the motor with the wheel two vertical columns of aluminium profile 2020 has been fixed from the other side of the base with one horizontal aluminium profile of length 50 mm between the two vertical columns as shown in Figure 4.16. Two internal joints are placed in the horizontal aluminium profile (50 mm) and two internal joints are placed in the aluminium profile 2040. Between the internal joint, a shock absorber is fixed at one end to the horizontal aluminium profile while the other end is attached to the aluminium profile 2040 which is fixed by a hinge with the base to give the wheel the freedom of rotation. The shock absorbers are adjusted at a certain height with the vertical column so that the wheels remain perpendicular to the tower surface.
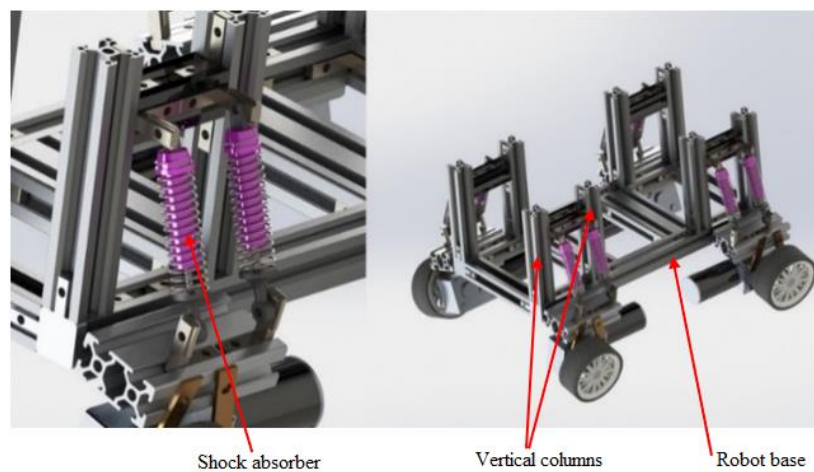
Figure 4.16 Two vertical columns holding shock absorber

After testing the robot experimentally, it was observed that due to the strong adhesion force of the magnets the vertical columns bend. Therefore, the design has been modified by adding a bar between every two vertical columns at the other end to support the vertical column as shown in Figure 4.17.
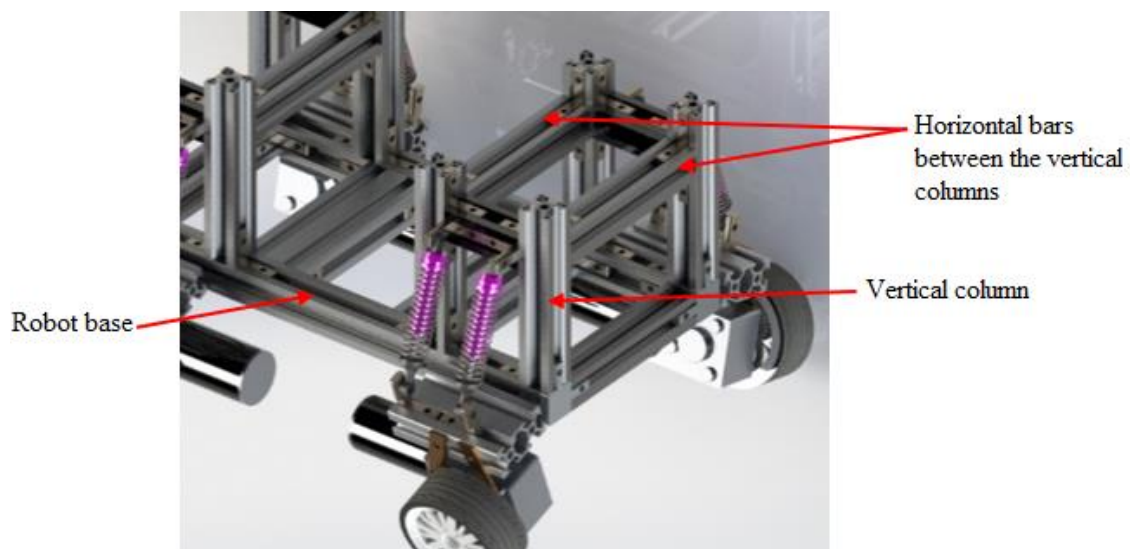
Figure 4.17 Horizontal supports for the vertical column

The robot is equipped with two arms for inspecting the wind turbine blades. These arms are designed with two degrees of freedom in the x-direction and y-direction. The design of the motion in each direction is based on a linear guide with linear bearing. An aluminium profile is fixed along the width of the robot over two fixation points on the vertical column. Then a linear guide is fixed with the aluminium profile with the linear bearing to provide the motion in x-direction as shown in Figure 4.18.
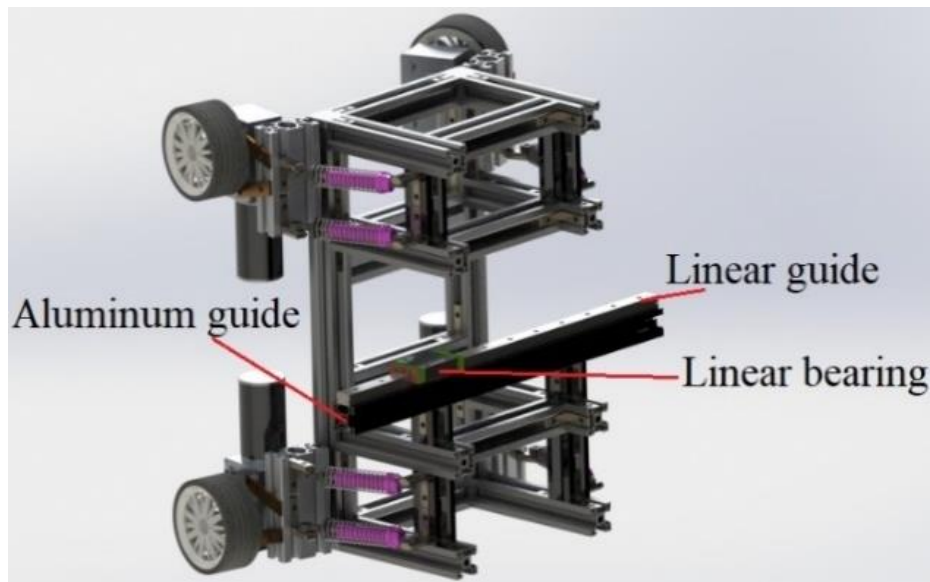
Figure 4.18 Linear guide with linear bearing to provide the motion in X-direction

The motion of the inspecting arm in the y-direction is provided with the same concept of the linear guide with linear bearing. The arm consists of two parts. One part is fixed on the linear bearing of the x-direction and another linear guide is fixed on top of this one to move the second part in the y-direction as shown in Figure 4.19.

In order to reduce the weight of the robot, the mechanism of the arm has been modified. Instead of the linear guide with linear bearing, two gantry plates were used with a belt to achieve the same motion and two degrees of freedom. The mechanism consists of a gantry plate, V-wheel with bearing and spacer to adjust the distance between the plate and the aluminium profile as shown in Figure 4.20. The motion is provided using a motor with GT2 pulley and timing belt. The timing belt is fixed between the GT2 pulley, the V-wheels and fixed along with the slot of the aluminium profile. Once the motor starts rotating the V-wheel moves along the aluminium profile bar.
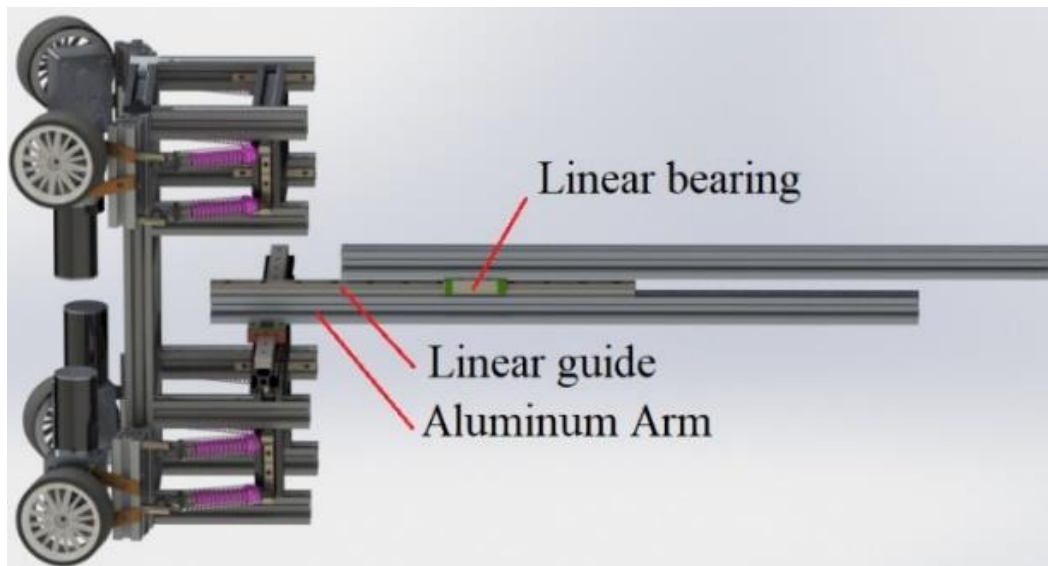
Figure 4.19 Linear guide with linear bearing to provide the motion in the y-direction
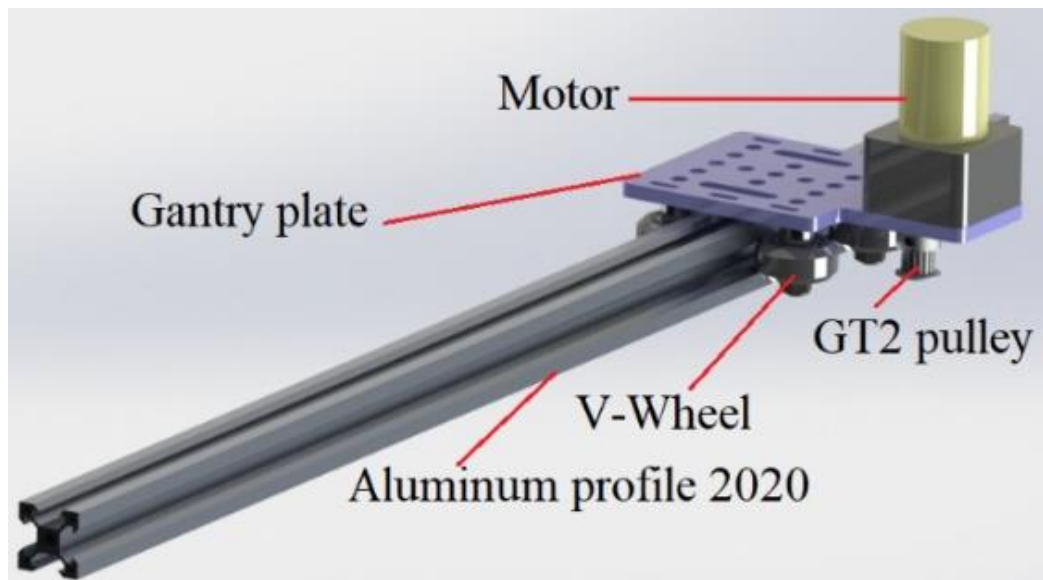
Figure 4.20 Gantry plate with V-wheels holding the motor with GT2 pulley to provide the motion by belt

The robot is equipped with two arms. Each arm consists of two parts and each part is of 500 mm length. The first part is carried on the gantry plate to move in the x-direction and the second part is carried on the other gantry plate to move in the y-direction. The movement in x-direction enables the arm to approach the blade for inspection when its leading edge is facing the tower while the movement in the y-direction is responsible for keeping the gripper with the inspection tool to follow the blade curvature as shown in Figure 4.21.
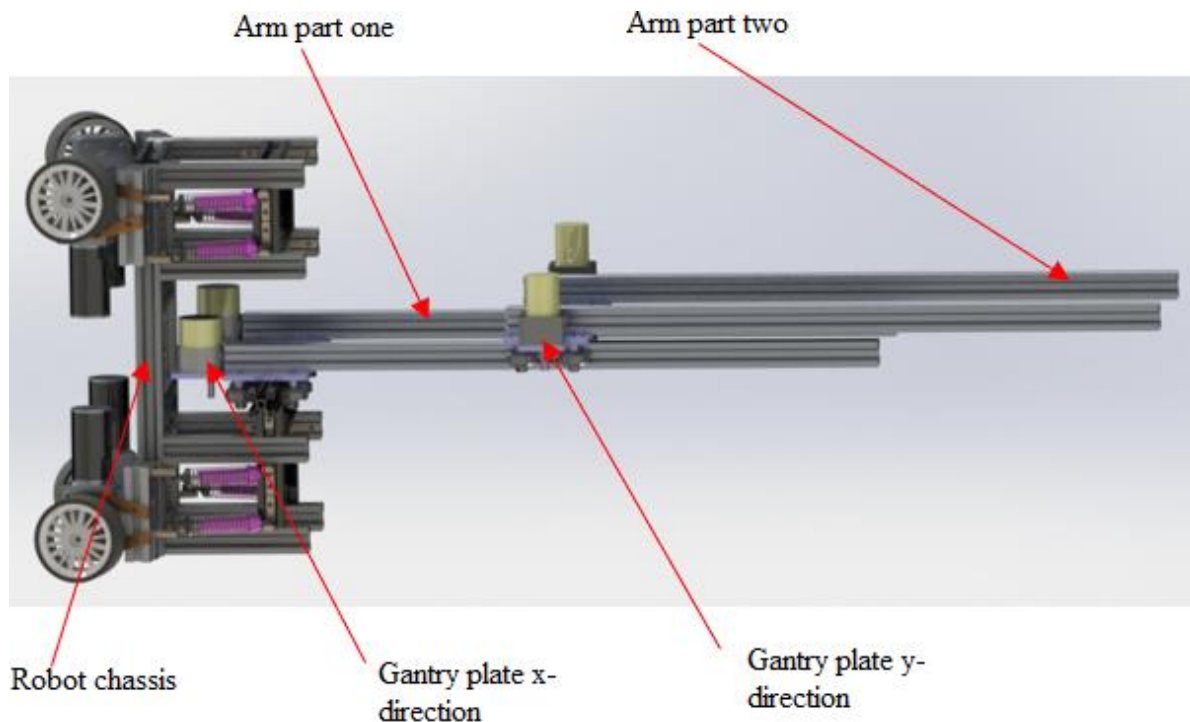
Figure 4.21 Each arm is equipped with two gantry plates for motion in X and Y directions

4.7. Testing of wall climbing robot

The final design of the robot has been tested experimentally and it was found that the arm bends when it is extended to its full length. As a result, the design of the robot has been modified with a supporting bar with a slider mechanism. The two lower aluminium profile bars of the robot have been changed with longer aluminium profile so that they can carry the slider mechanism which will support the motion in the x-direction. Two slider mechanisms were used, one for each arm. Over the slider mechanism, supporting bars from the same type of aluminium were used and fixed with the first part of the arm as shown in Figure 4.22. In order to examine the functionality of the wall climbing robot, a prototype of a wind turbine has been modelled.
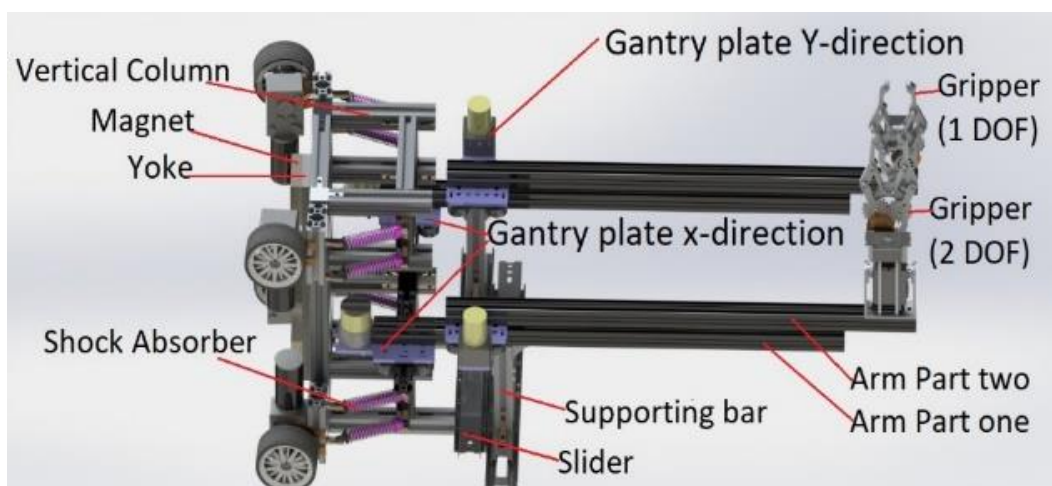
Figure 4.22 Final prototype robot assembly

4.8.   Wind turbine model Prototype

A model of the wind turbine was developed in SolidWorks including advanced part modelling, assembly and creating a drawing package for the turbine prototype. There are three main parts to model the wind turbine; which are the tower, section of the tower, a steel bar used instead of the nacelle to fix the blade at a certain distance from the tower and the blade. The purpose of the wind turbine model is to test the prototype climbing robot. Figure 4.23 illustrates the drawing of the wind turbine model with dimensions.
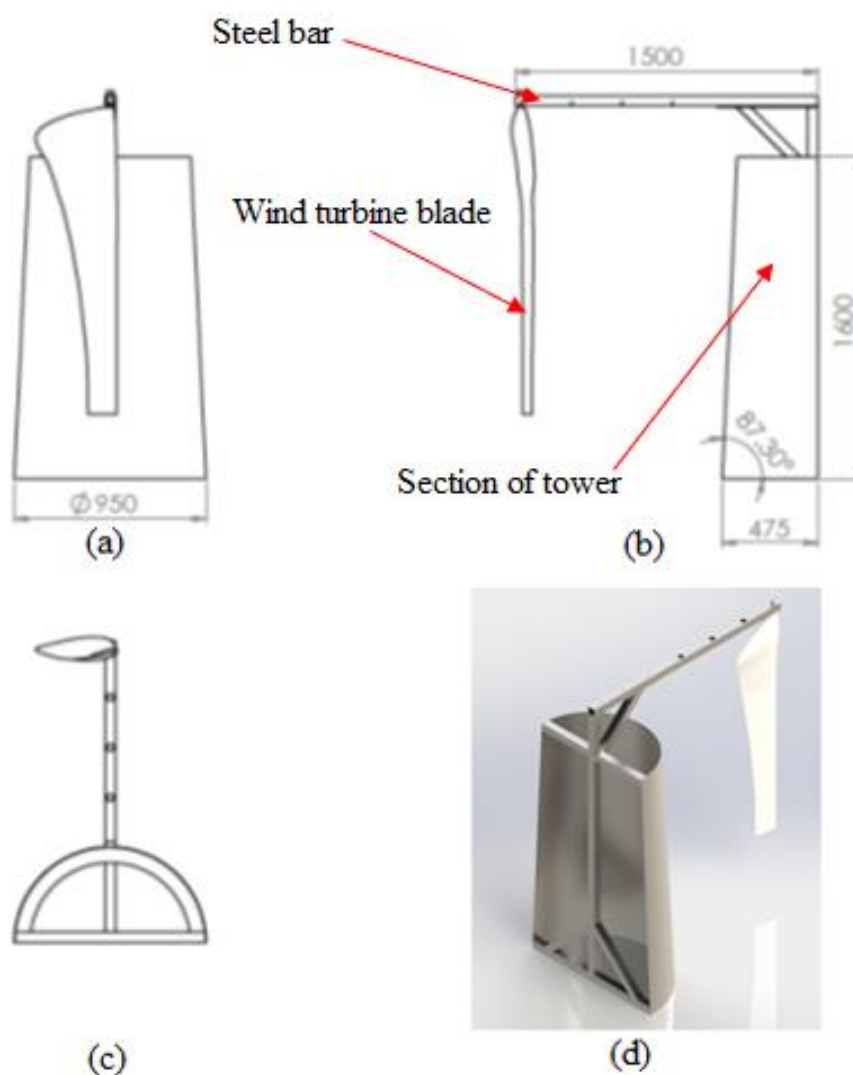
Figure 4.23 Wind turbine prototype model

4.8.1.   The tower section of the wind turbine prototype

The tower is made from a steel sheet with a thickness of 3 mm. The steel sheet has been rolled to form a conical shape with a height 1.6 m with angle 87.3º from horizontal axis and base diameter 0.95 m.as shown Figure 4.23.

4.8.2. The steel bar for holding the blade

A steel bar instead of the nacelle has been modelled to be used for holding the blade in front of the tower. The bar is modelled with several holes as shown in Figure 4.24 to be utilised for holding the blade at four different distances from the tower.
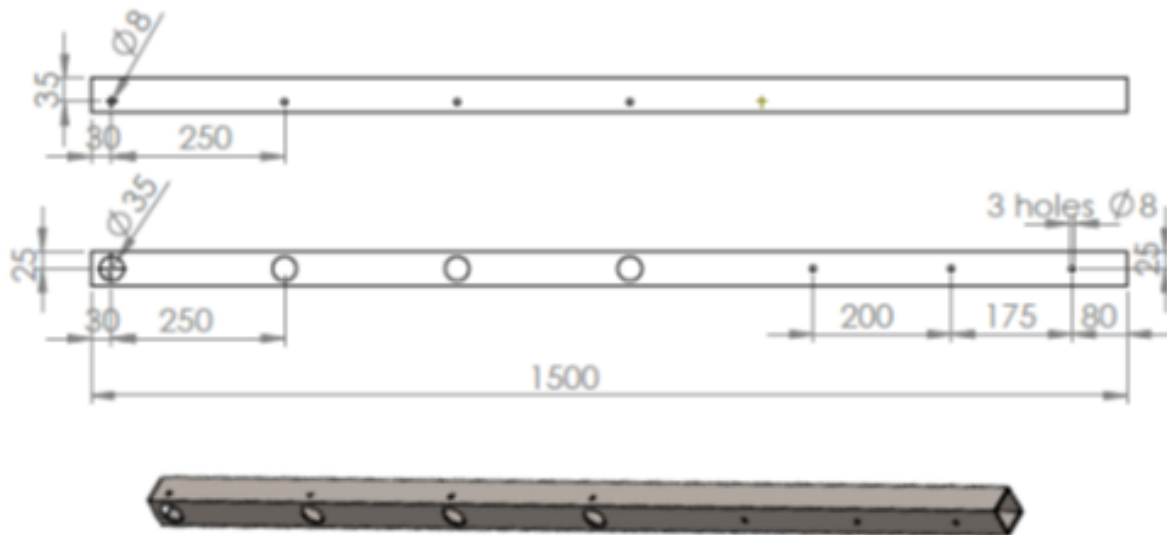
Figure 4.24 Steel bar

4.8.3. Wind turbine blade prototype

A prototype blade has been modelled with dimensions relative to the tower dimensions. The blade is 0.4 m width at the root and 0.145 m at the tip. Figure 4.25 illustrates the three views and a rendered image of the wind turbine blade prototype.
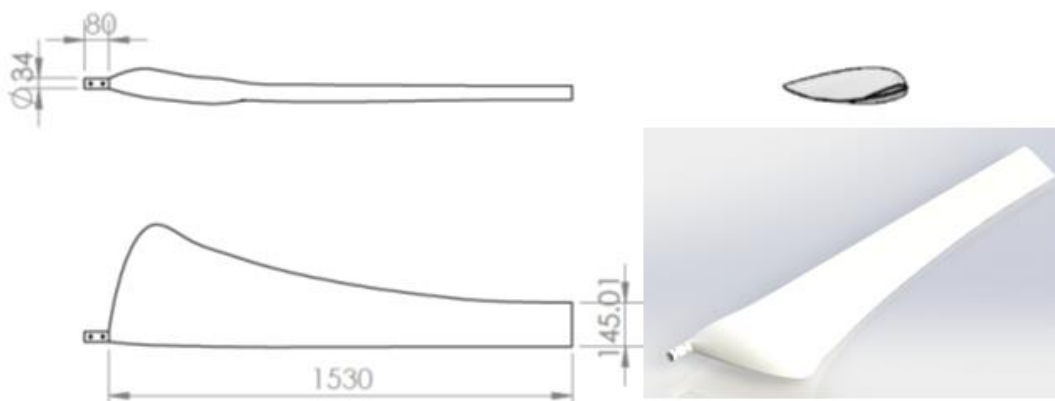
Figure 4.25 Three view and isometric of wind turbine blade prototype

4.9. Wind turbine prototype assembly with the prototype robot

In order to verify the compatibility of the wind turbine prototype model dimensions with the prototype climbing robot, an assembly process has taken place. The assembly is shown in Figure 4.26

84
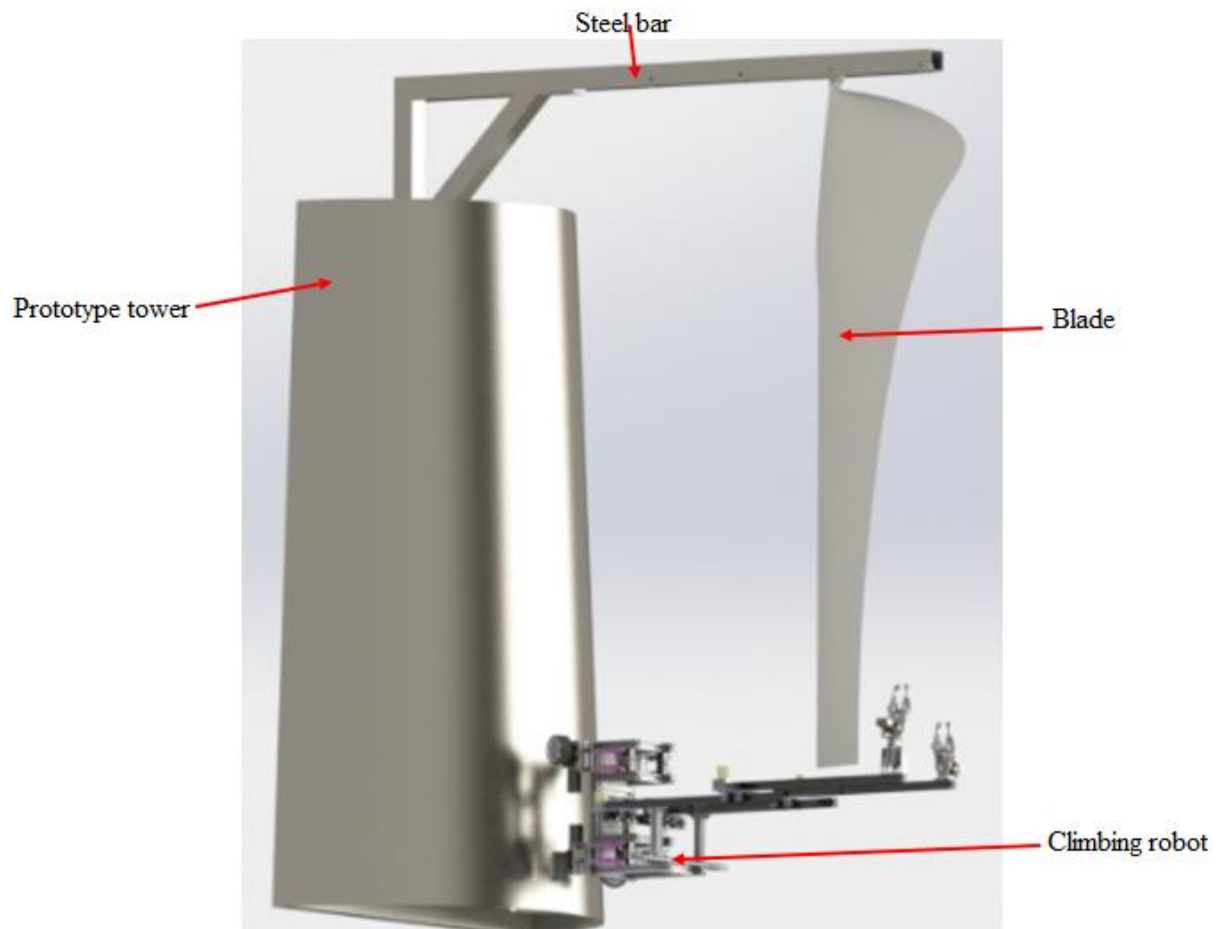
Figure 4.26 Assembly of wind turbine tower prototype and robot prototype

4.10. Implementation of wind turbine prototype and climbing robot prototype

The robot was implemented according to the model as illustrated in Figure 4.22 and tested on the wind turbine described in the previous section as shown in Figure 4.23. The robot climbing the prototype tower is shown in Figure 4.27 where the blade is between the two arms for inspection. The air gap between the magnets and the tower is 12 mm. The total weight of the robot is 10 kg. The magnetic adhesion force of the robot is measured using a test rig described in the previous chapter and it was 33 kg at an air gap of 12 mm.
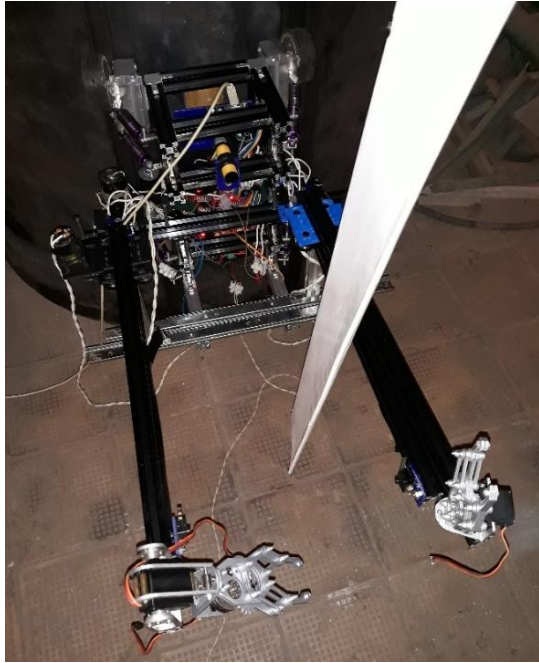
Figure 4.27 Prototype robot climbing the tower

Figure 4.28 Wind turbine tower and blade with the climbing robot

The robot is equipped with four motors for traction and four motors for the four gantry plates. Each motor is connected to H-bridge L298N to control the direction of rotation. Four H-bridges are used: two for the motion of the robot upward and downward and one H-bridge for each arm. One proximity sensor is used to detect the presence of the blade and eight limit switches are used for controlling the two arms. Each arm is controlled with four limit switches two for the x-axis direction and two for y-axis direction. Three servo motors are utilised to control the two grippers.

Each wheel of the robot is actuated with 12 V brushless DC Worm gear motor with 11 rpm for robot vertical motion on the WT tower. The speed of the robot during climbing is 0.037 m/s so the time taken to climb the tower without inspection is 40 seconds. Two brushless DC 12 V motors are used to control each arm.

During testing, it was observed that the wall climbing robot on the wind turbine was stable as the wheels were able to adjust to the curvature of the tower. The scanning arm had the ability to reach all parts of the blade easily.

The controller is Arduino Uno to which all motors and sensors are connected. The robot moves upward until the photoelectric proximity sensor detects the presence of the blade after which the two arms are extended so that the grippers with the inspection tool can reach the surface of

the blade. The sequence of the robot motion is shown in Figure 4.29 to Figure 4.31. The control algorithm used is a closed-loop no-off controller and the flowchart for the control process of the robot during the inspection is shown in Figure 4.32. The robot starts at the bottom of the wind turbine tower by checking that the arm is in the initial position. The two arms are retracted and opened. Then the robot starts to climb the tower until the proximity sensor detects the blade. The robot extends the two arms to the maximum length. The arms then move inward towards the blade to scan across the blade surface by retracting the arms. The robot then moves up the tower to the next inspection stop and the process is repeated until the robot reaches the top of the tower.
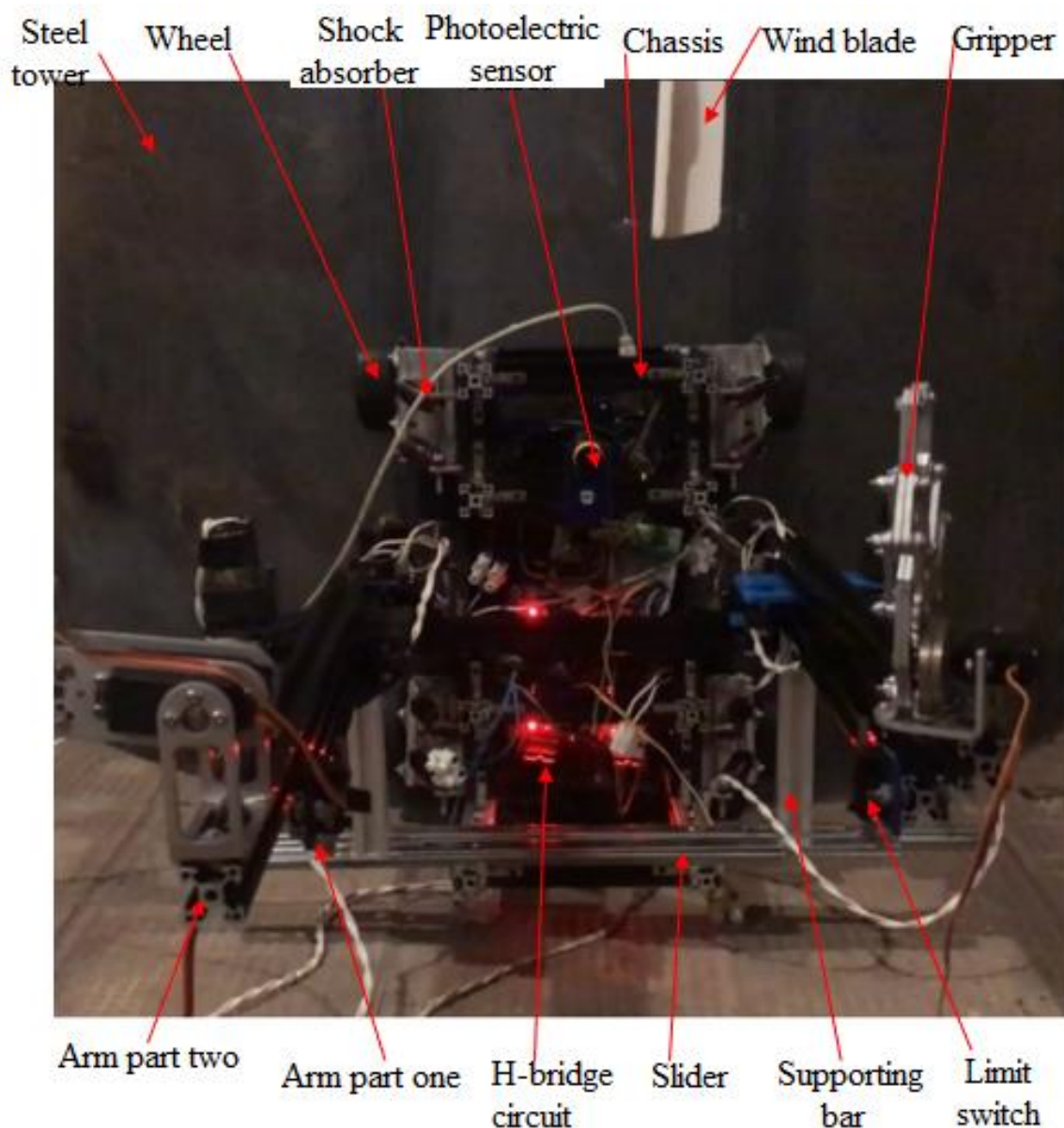
Figure 4.29 Climbing robot at the bottom of the tower
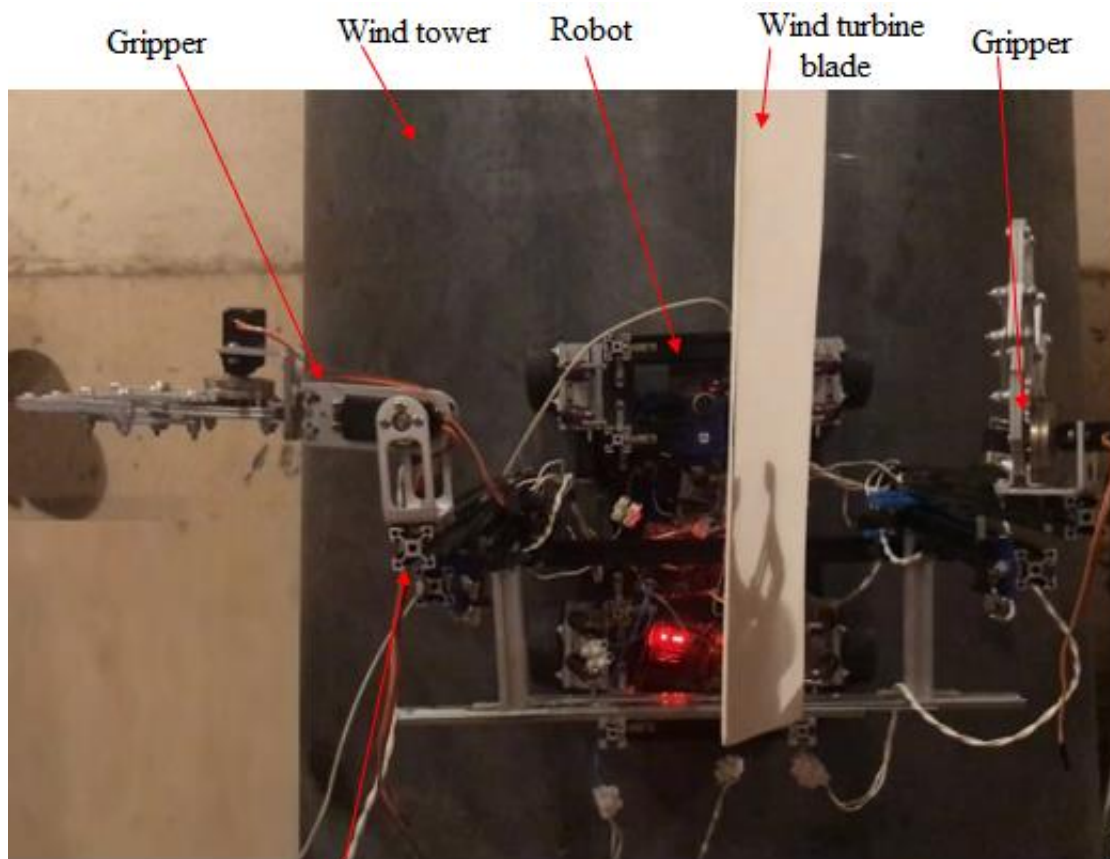
Figure 4.30 Climbing robot in front of the blade retracting its arms
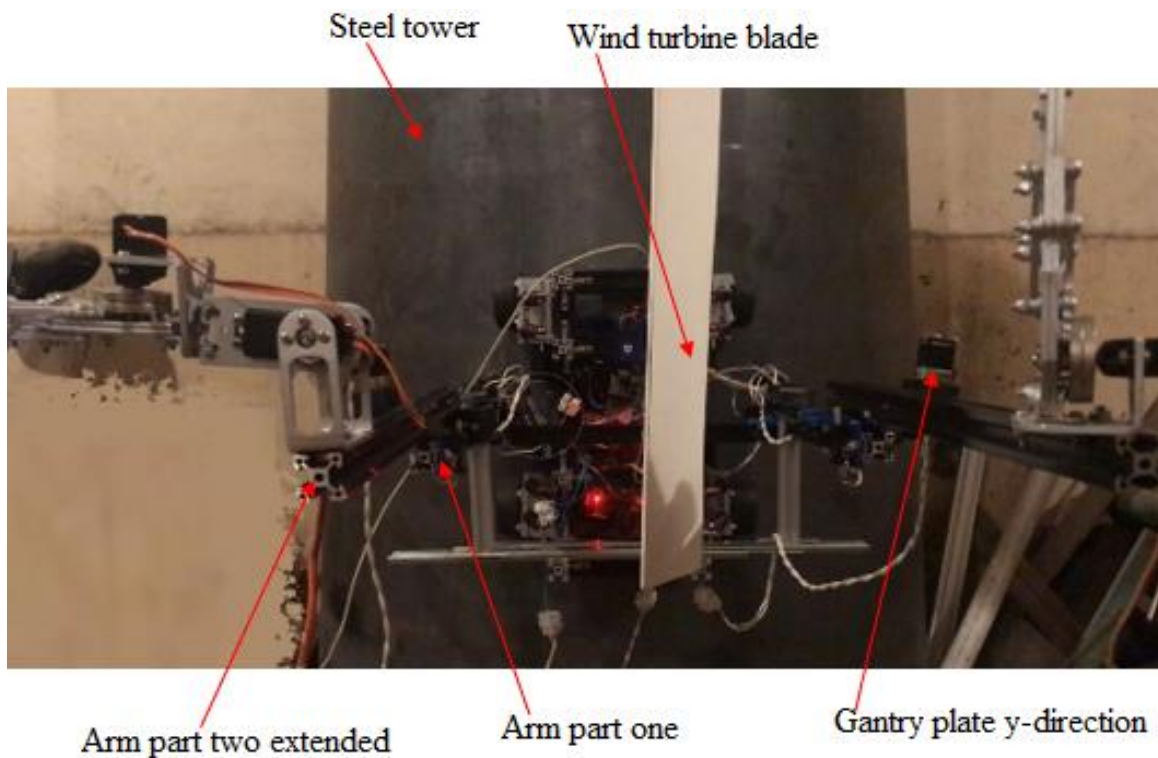
Figure 4.31 Climbing robot in front of the blade with arms extended
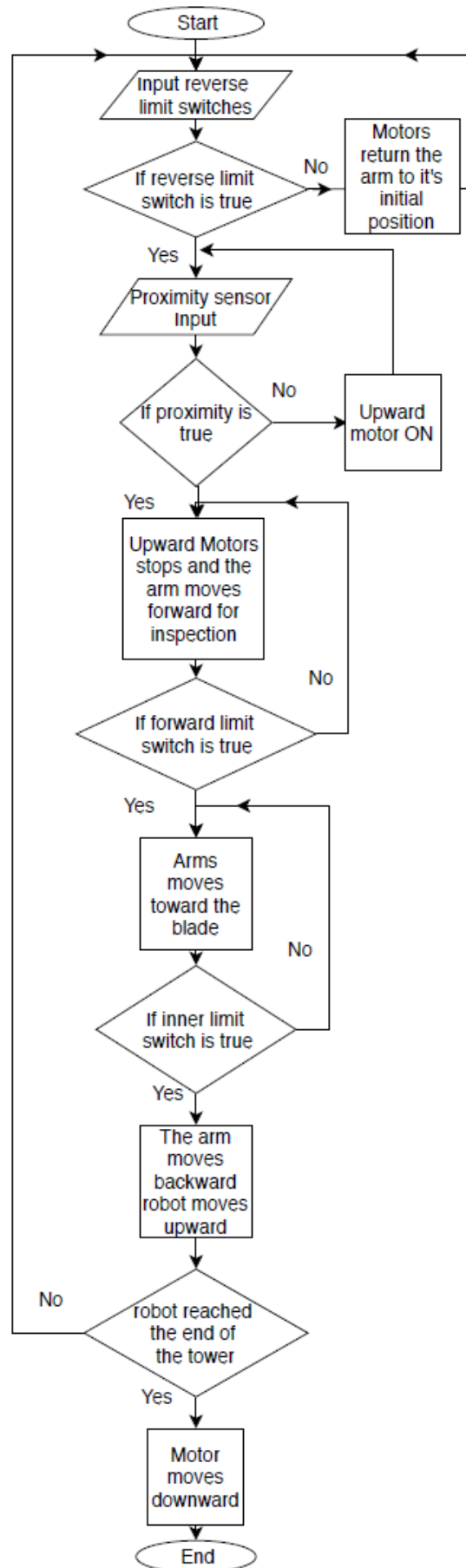
Figure 4.32 Robot control flowchart

4.11. Static force analysis

The forces acting on the robot are shown in the free-body diagram of Figure 4.33. These are the magnetic adhesion force F_m, the normal force N, the weight of the robot W_R, friction force R and the weight of the inspection tool W_L. Knowing the weight of the robot and the adhesion force, the equilibrium equations are used to calculate the maximum weight that the arm can carry. Equation (4.1) shows the summation of forces in the x-direction and equation (4.2) shows the summation of forces in the y-direction. Equation (4.3) shows the summation of the moment around the centre of gravity (CG) of the robot.
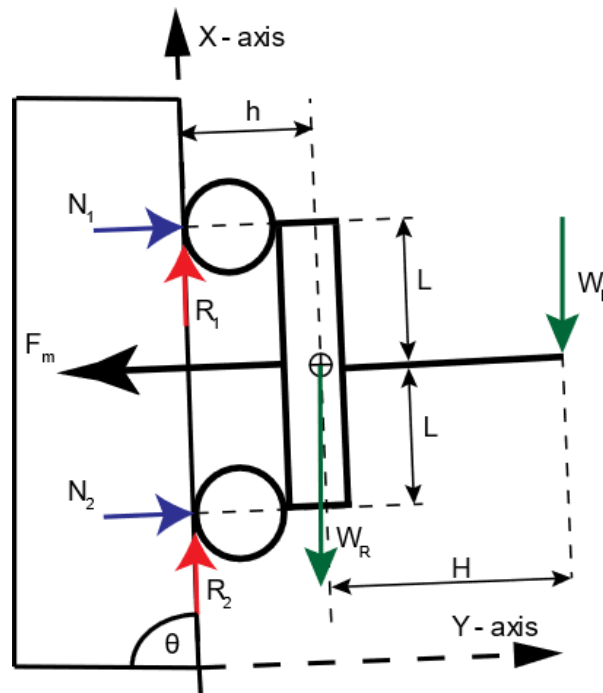
Figure 4.33 Free body diagram of the climbing robot

$$\sum F_x = 0 \qquad (4.1)$$

$$F_x = R_1 + R_2 - W_R \sin\theta - W_L \sin\theta$$

$$\sum F_y = 0 \qquad (4.2)$$

$$F_y = N_1 + N_2 - W_R \cos\theta - W_L \cos\theta - F_M$$

$$\sum M = 0 \qquad (4.3)$$

$$M_G = -(R_1 + R_2)(h) + (N_2 - N_1)(L) - W_L \sin\theta\,(H)$$

$$R = \mu N \qquad (4.4)$$

By solving the three equations (4.1 – 4.3) simultaneously and assuming the coefficient of friction μ=0.6 it is found that the maximum load that can be carried by the arm is equal to 2 kg.

4.12. Chapter summary

In this chapter, a small-scale robot prototype has been developed to test the feasibility of carrying long deployment arms and inspection sensors to wind turbine blades. Two different designs for the wall climbing robot have been presented, where the concerns on the preliminary design were taken into consideration in the final design. The prototype robot has been designed with two arms, each one meter long, with end effector for carrying the inspection tool. The two arms have two degrees of freedom so they can follow the aerodynamic shape of the blade during the inspection. The wheels of the robot have been installed using hinges and shock absorbers so that they adjust themselves to a tapered tower. The robot has been controlled using Arduino Uno to which all motors and sensors are connected. A prototype wind turbine tower model has been designed and implemented with a length of 1.8 m and diameter of 0.95 m. A small blade with a length of 1.5 m has been designed and installed on the tower using a steel bar. The steel bar is designed with several holes where the blade can be placed at a different distance in front of the tower from 0.25 m to 1 m. Finally, an inspection tool up to one kilogram in each arm can be added to inspect the WTB while keeping the climbing robot in static equilibrium.

Chapter 5

Scaled up climbing robot

5.1. Introduction

While a scaled-down design of WTB inspection robot proved to be capable of carrying the similarly scaled-down required payload, the next phase of this research considered whether it was feasible to develop a robot for the typical full-scale WTB (100 m tall tower with 76 m long blades). In this chapter, a wind turbine has been modelled with a real dimension to scale up the prototype robot based on its dimensions. A detailed procedure has been presented for the scaling up of the prototype climbing inspecting robot. Static stress analysis and flow simulation have been carried out to check the durability of the scaled-up robot while climbing the wind turbine tower.

5.2. Robot scale up

In order to scale up the robot, a model of a medium-sized wind turbine has been created to estimate the dimensions of the scaled-up robot.

5.3. Preliminary wind turbine modelling

A wind turbine model was implemented in SolidWorks to include advanced parts, their assembly and a drawing package for the turbine. There are four main parts to model the wind turbine. These are the tower, nacelle with the tail vane, a hub with nose cone and the blades. The purpose of the model is to get the dimensions required to build a robot capable of inspecting the wind turbine. Figure 5.1 illustrates the drawing of the wind turbine showing the approximate real dimension.
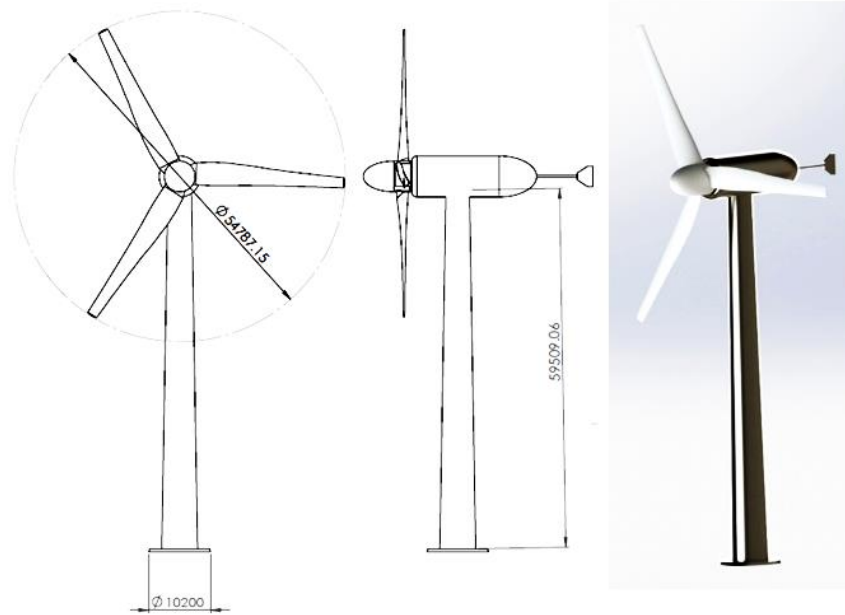
Figure 5.1 Wind turbine drawing and rendered image in SolidWorks

5.3.1. The tower

The tower consists of three parts. These are the support base, tower and upper base. The tower is engaged with the upper base with bearings. The lower base is circular in shape with diameter 10 m, taper angle 18 degrees, and height 5.1 m. The tower is 59.5 m high with a diameter at the base of 5.9 m and taper angle 2 degrees. Figure 5.2 depicts the drawing of the WT tower and its isometric view.
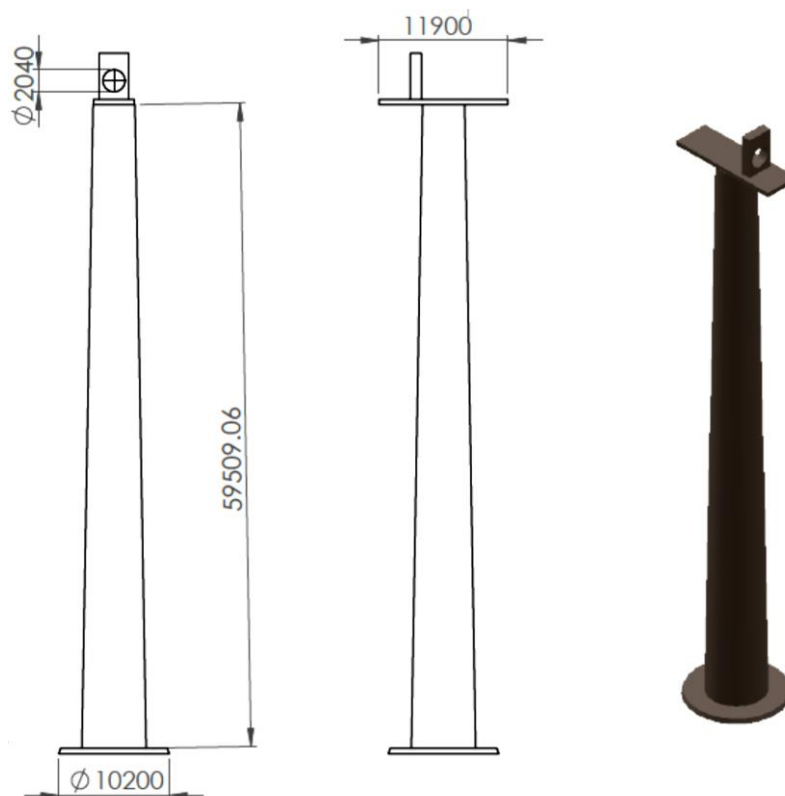
Figure 5.2 Drawing of the wind turbine tower

5.3.2.   The nacelle and tail vane

The nacelle is the housing for all mechanical and electrical components. The nacelle is circular with a diameter 6.8 m and length 20.6 m. At the end of the nacelle, the tail vane is connected. Figure 5.3 illustrates the drawing of the wind turbine nacelle and tail vane.
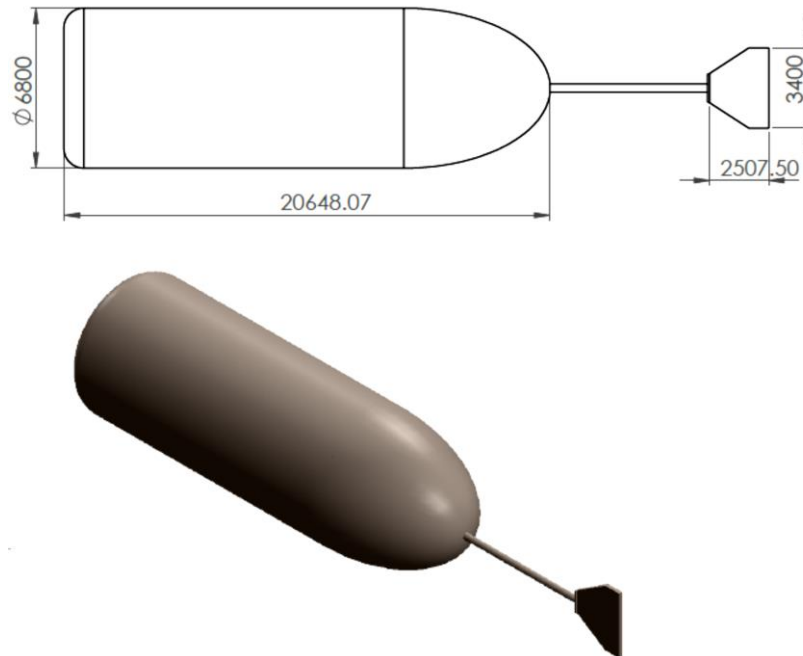
Figure 5.3 Drawing of the wind turbine nacelle and tail vane

5.3.3.   Hub with nose cone

The rotor hub is connected to the front face of the nacelle on the turbine axle. The main purpose of the hub is to hold the blades. The hub was designed with three slots for the root of the blade to be fitted into the hub as shown in Figure 5.4 (a). Furthermore, a nose cone is connected to the hub from the other side to provide an aerodynamic structure as shown in Figure 5.4 (b).

(a) Hub
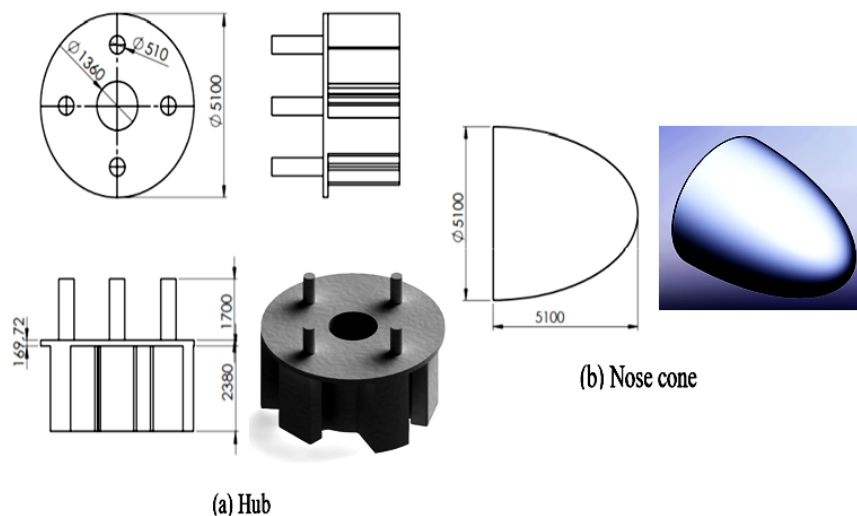
(b) Nose cone

Figure 5.4 Hub and nose cone

94

5.3.4. Blades

The blade is the part that is responsible for converting kinetic energy into mechanical energy. The wind turbine consists of three identical blades each of length 24 m. The blade width is 3.6 m at the root and 1.7 m at the tip. The blade is designed with several aerofoils where each aerofoil has a relative angle. The difference between the relative angle at the tip and the relative angle at the root is known as the twist angle, or the amount of twist on the blade. Figure 5.5 illustrates views, and rendered image showing the twist angle of the wind turbine blade.
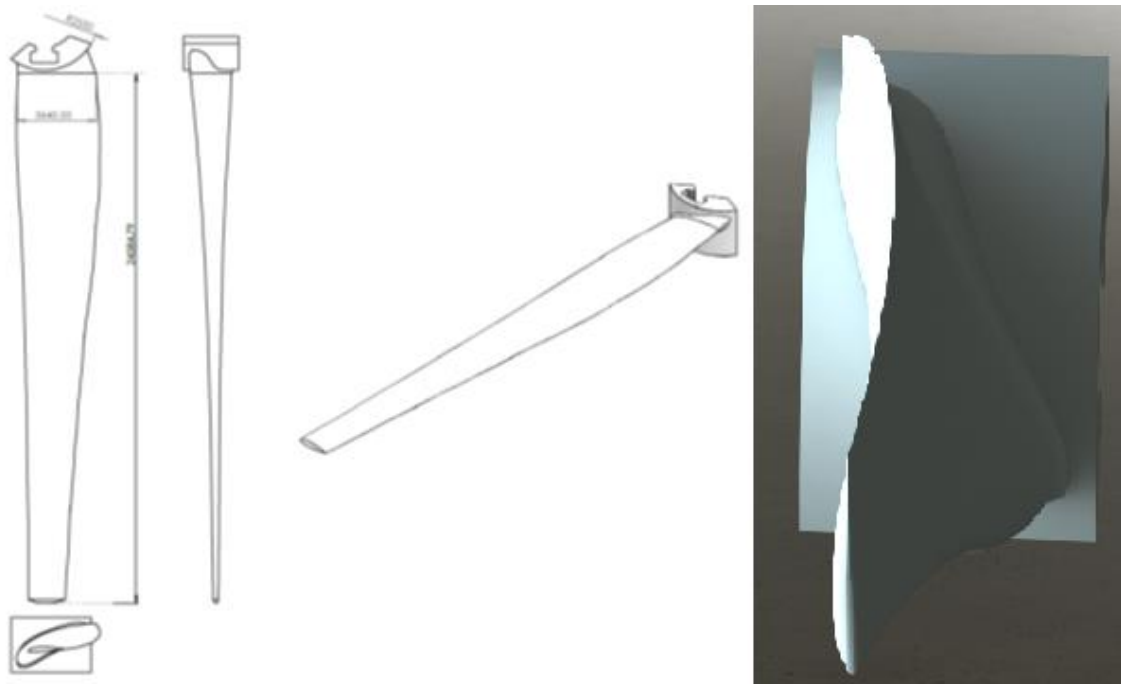
Figure 5.5 Three view and isometric of the wind turbine blade

5.4. Final wind turbine modelling

The components of an offshore wind turbine include the monopile, the transition piece, the tower, the rotor blades, the hub and the nacelle. The monopile is the foundation system and support structure for an offshore wind turbine. A new model of the wind turbine has been implemented in SolidWorks to match the real dimension and shape of the real offshore wind turbine. The model is built with respect to the dimensions of the Siemens offshore wind turbine SWT-6.0-154. The largest offshore wind turbine is 12MW [101]. So, the modelled offshore wind turbine is considered to be medium in size. The monopile is not modelled as it is under sea level and not part of an interest in the inspection process. The model includes advanced part modelling, assembly and creating a drawing package for the turbine prototype. There are four main parts to be modelled which are the transition piece, the tower, nacelle, a hub and the

blades. The purpose of the model is to get the dimensions required to build a full-scale robot capable of inspecting the wind turbine. Figure 5.6 illustrates the drawing of the wind turbine showing the approximate real dimensions.

Figure 5.6 Wind turbine drawing and rendered image, SolidWorks

5.4.1. The tower

The tower consists of the three parts the monopile, the transition piece, the tower. The tower is engaged with the nacelle with bearings. The tower is circular in shape with diameter 5.8 m at the base and tapered where the diameter at the top is 3 m and height 100 m. The transition piece is circular with diameter 6 m and height 10 m.

5.4.2. The nacelle with serpentine

The nacelle houses all mechanical and electrical components. The nacelle is circular with diameter 4 m and length 15 m. At the top of the nacelle, a serpentine is connected which is used for cooling. Figure 5.7 illustrates the wind turbine nacelle and serpentine. The internal housing of the nacelle is designed inclined with 6 degrees to match the real wind turbine.

5.4.3. Hub

The rotor hub is connected to the front face of the nacelle on the turbine axle. The main purpose of the hub is to hold the blades. The hub has been modelled circular in shape with three circular openings in the circumference of the hub to hold the three blades. The blades are installed with the hub at angle 3 degrees. The hub is illustrated in Figure 5.8.
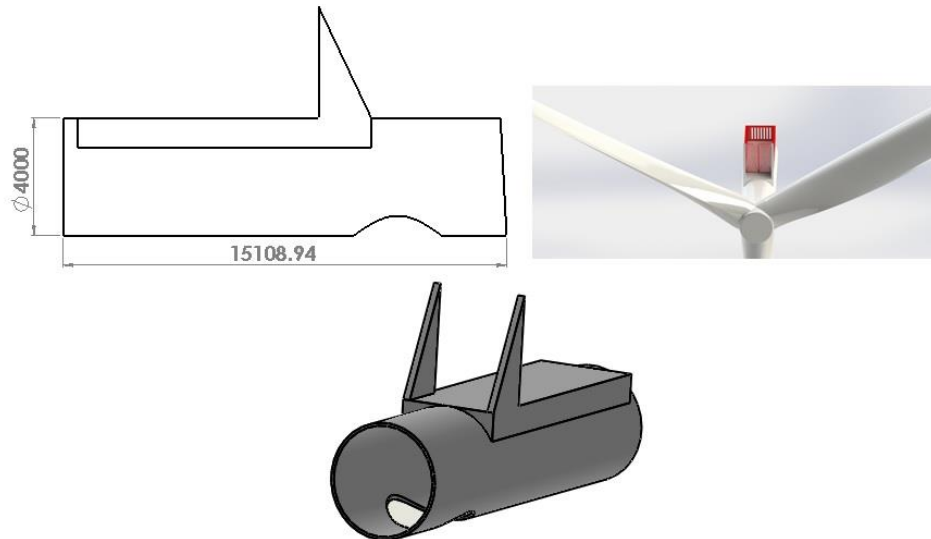
Figure 5.7 Drawing of the wind turbine nacelle and serpentine
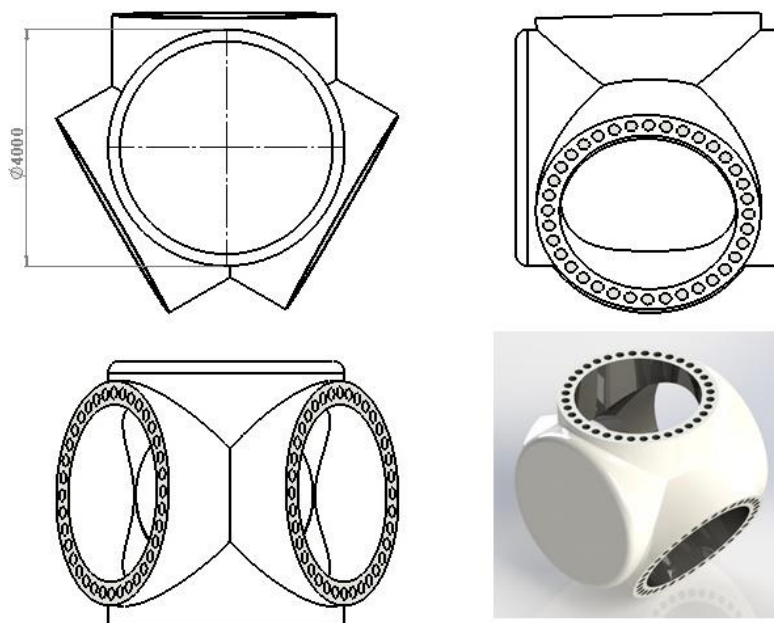
Figure 5.8 Hub

5.4.4. Blades

The wind turbine consists of three identical blades, each of length 76 m. The blade width is 3.6 m at the root. The blade is designed with several aerofoils where each aerofoil has a relative

angle. The difference between the relative angle at the tip and the relative angle at the root is known as the twist angle, or the amount of twist in the blade. Figure 5.9 illustrates a rendered image showing the twist angle of the wind turbine blade.
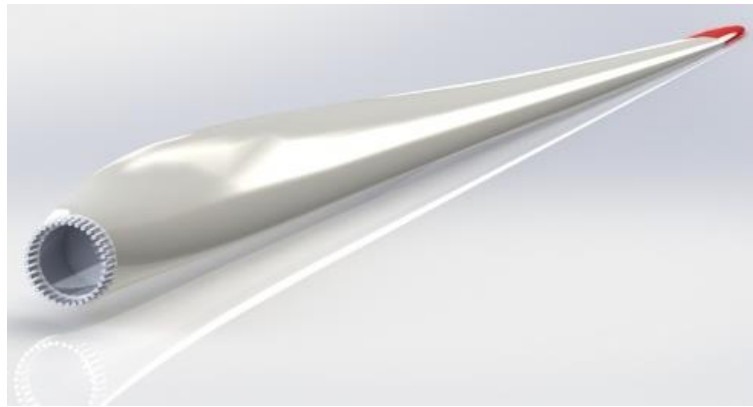
Figure 5.9 Three view and isometric of the wind turbine blade

5.5.   Scaling up procedures of the climbing robot

The scaling process of the robot is based on the dimension of the wind turbine model described in the previous section 5.4. Before explaining the scaling process, the inspection mechanism of the wind turbine blade should be taken into consideration. The inspection process will be carried out while the turbine is out of service and the blades will be inspected one by one. The blade to be inspected will be in front of the tower and it's leading-edge will be facing the tower. Then the robot will start climbing the tower and once it reaches the blade the inspection process will start using the two arms of the robot. Each arm consists of two parts of equal length. The first part is carried on the gantry plate to move in the x-direction and the second part is carried on the other gantry plate to move in the y-direction. The movement in x-direction enables the arm to approach the blade for inspection when its leading edge is facing the tower while the movement in the y-direction is responsible for keeping the gripper with the inspection tool to follow the blade curvature.

As a result, the inspection process is based mainly on the length of the arm. The arm should be long enough to reach the blade for inspection. So, all the dimensions of the robot are scaled up based on the length of the arm. Consequently, the cross-section of the arm should be scaled up.

5.5.1.   Cross-section scale up

The first prototype robot was designed from aluminium bars called aluminium profile 2020. The twenty is referring to the width and height of the aluminium bar. The cross-section of the

aluminium bar is modelled as shown in Figure 5.10 with all its details. The scaling up has been assumed to be linear and accordingly, a linear equation has been formulated. Each length has been multiplied by a scale factor named "X". The scale factor "X" has been given an initial value equal to 20 mm which is the initial width of the aluminium bar. Each length is multiplied by "X" and divided by 20 to keep its initial value as it is if the value of "X" = 20 mm. The dimensions are named from D1 to D16 as shown in Table 5.1.
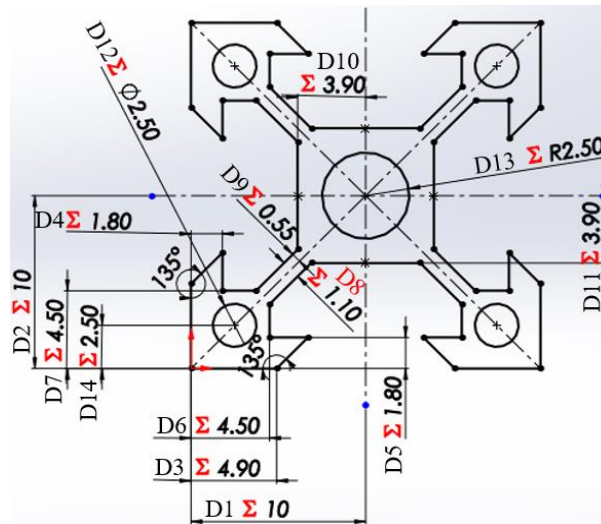
Figure 5.10 Dimensions of the aluminium profile bar

Table 5.1 Cross-section scale-up equations

Length	Equation
D1	"X" * 10/20
D2	"X" * 10/20
D3	"X" * 4.9/20
D4	"X" * 1.8/20
D5	"X" * 1.8/20
D6	"X" * 4.5/20
D7	"X" * 4.5/20
D8	"X" * 1.1/20
D9	"X" * 0.55/20
D10	"X" * 3.9/20
D11	"X" * 3.9/20
D12	"X" * 2.5/20
D13	"X" * 2.5/20
D14	"X" * 2.5/20

5.5.2. Length of each component in the robot

The scale up of the robot regarding the length of each bar is based on the length of the arm. The length of the arm is named as "L" and each component in the robot is multiplied by "L". Using this formula, the ratio between all components will remain the same and will not change. Every single part of the robot has been given a name for the equation, as shown in Figure 5.11 and examples of the equations are shown in Table 5.2.
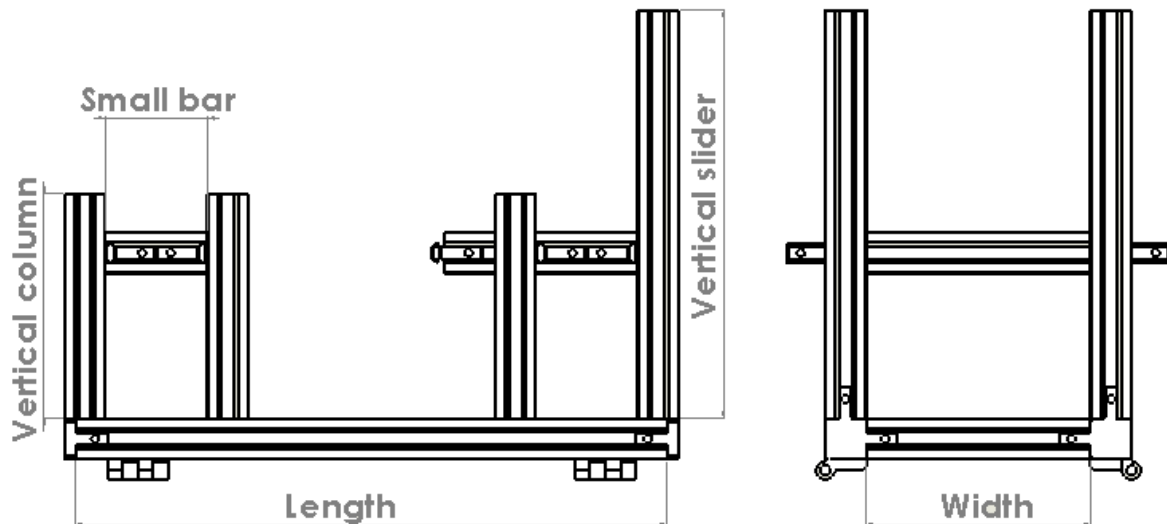
Figure 5.11 Length scale-up of the robot

Table 5.2 Length scale-up equations

Length	"L" * 0.29
width	"L" * 0.11
Vertical column	"L" * 0.11
vertical slider	"L" * 0.2
small bar	"L" * 0.05
support bar	("L" * 0.075) + ("X" * 1.9325)
wheel chassis	"L" * 0.073

5.6. Robot specifications and evaluation

5.6.1. Robot specification

Based on the wind turbine model described in the previous section, it was found that the distance between the tower and blade, while the blade is standing in front of the tower and the leading edge is facing the tower, is 10 m. Accordingly, the robot has been scaled so that the length of the arm becomes 10 m and the cross-section has been multiplied by ten. Where "L"

is set to be 10,000 mm and "X" is set to be 200 mm. This means that the robot dimensions have been changed where the length becomes 3 m long and the width is 1.1 m.

5.6.2. Evaluation

After scaling up the robot, the robot has been subjected to the evaluation process regarding the constancy of the dimension of all components and the total weight of the robot. As it was a linear scale it was found that the dimension has revealed the same aspect ratio as the prototype as was expected. While upon evaluating the overall weight of the robot, the total weight has been found to be 48,942 N without the inspection tools. This was found to be a very high weight regarding the achievement of a very high magnetic adhesion force required to attach the robot to the tower and the deployment of the robot on the wind turbine tower. As a result, the scaling-up process of the robot was entered into another iteration to reduce the total weight of the robot. As the distance between the blade and the tower cannot be changed, it was found that the easiest solution for reducing the weight is to reduce the cross-section of the aluminium bars. Consequently, the cross-section has been reduced by setting the value of "X" to 110 mm after checking that this value will not affect the functionality of the robot and the weight has been reduced to 11,130 N.

5.7. Stress analysis

Static stress analysis is carried out on the scaled-up design of the inspection robot to calculate displacements, reaction forces, strains, stresses, failure criterion and factor of safety. Static studies provide tools for the linear stress analysis of parts and assemblies loaded by static loads. The following sections describe in detail all the process of stress analysis procedures starting with parts and assembly, creating suitable meshing and element type, defining the proper materials and boundary conditions.

5.7.1. Model parts and assembly

The robot assembly has two hundred and three components: the chassis, hinges, internal joints, external joint, gantry plates, V-wheels, motors, motor bracket, motor coupler, shock absorber, wheels, grippers and GT2 pulley and sliders. Figure 5.12 shows the assembly components in exploded view.
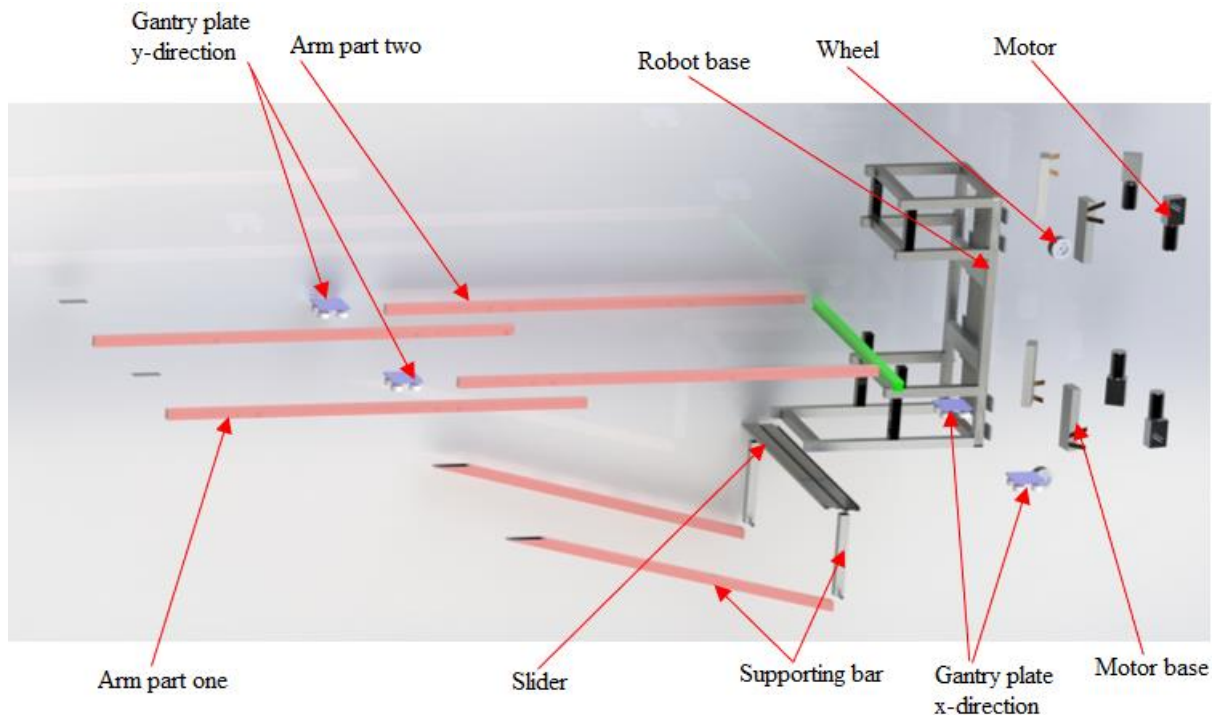
Figure 5.12 Robot exploded view

5.7.2. Meshing and element type

Meshing divides the model into smaller pieces called elements. Based on the geometrical dimensions of the model, SolidWorks simulation suggests a default element size which in this case was 44.4 mm and it can be changed as needed. The mesh parameter was chosen as a curvature-based mesh. The total number of elements were 34194. Figure 5.13 shows the meshing.
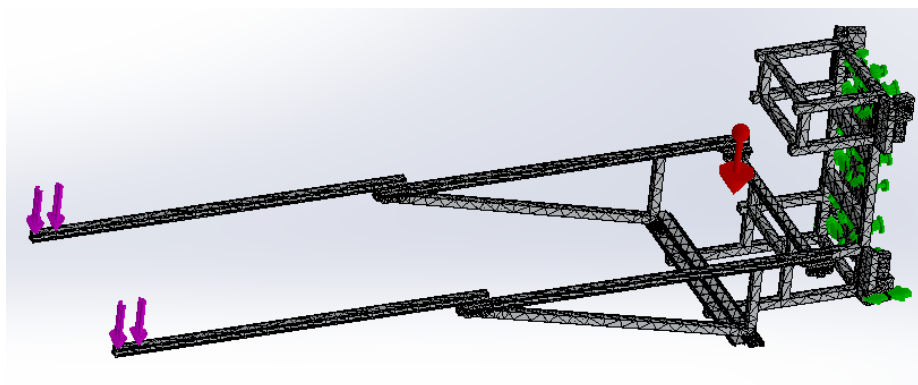
Figure 5.13 Meshed model

5.7.3. Material model

Aluminium 6063-T5 is the material assigned to all components of the robot, which is the same material used in the prototype except for the hinges. Alloy steel is assigned to them instead.

The mechanical properties of aluminium 6063-T5 are listed in Table 5.3 and the mechanical properties of the alloy steel are listed in Table 5.4.

Table 5.3 Aluminium 6063-T5 properties

Property of Aluminum 6060-T5	Value
Yield strength:	$1.45e+008$ N/m^2
Tensile strength:	$1.85e+008$ N/m^2
Elastic modulus:	$6.9e+010$ N/m^2
Poisson's ratio:	0.33
Mass density:	2700 kg/m^3
Shear modulus:	$2.58e+010$ N/m^2
Thermal expansion coefficient:	$2.34e-005$ /Kelvin

Table 5.4 Alloy steel properties

Property of Alloy steel	Value
Yield strength:	$6.20422e+008$ N/m^2
Tensile strength:	$7.23826e+008$ N/m^2
Elastic modulus:	$2.1e+011$ N/m^2
Poisson's ratio:	0.28
Mass density:	7700 kg/m^3
Shear modulus:	$7.9e+010$ N/m^2
Thermal expansion coefficient:	$1.3e-005$ /Kelvin

5.7.4. Contact formulation

The contact type used is the global contact. There are three options for global contact which are the bonded, no penetration, and allow penetration. The difference between the three options is that the bonded treats the parts as if they are welded together and they act as one part. The no penetration option prevents interference between the parts while allowing penetration under loading allows the parts to interfere together. So, in this study since all parts are connected using internal and external joints, the bonded option has been selected.

5.7.5. Applying restraints

In order to perform a realistic simulation of the magnetic adhesion force of the neodymium magnet, a fixed restraint is applied on the magnet surface where all three translations and three rotations are set to zero. In accordance with Figure 5.14, the selected faces, where fixed

restraint boundary condition is applied, are indicated by green arrows. In addition, the two bottom wheels, which will be in direct contact with the tower, are assigned to have their motion restraint along the direction of reaction force due to the contact with the tower.
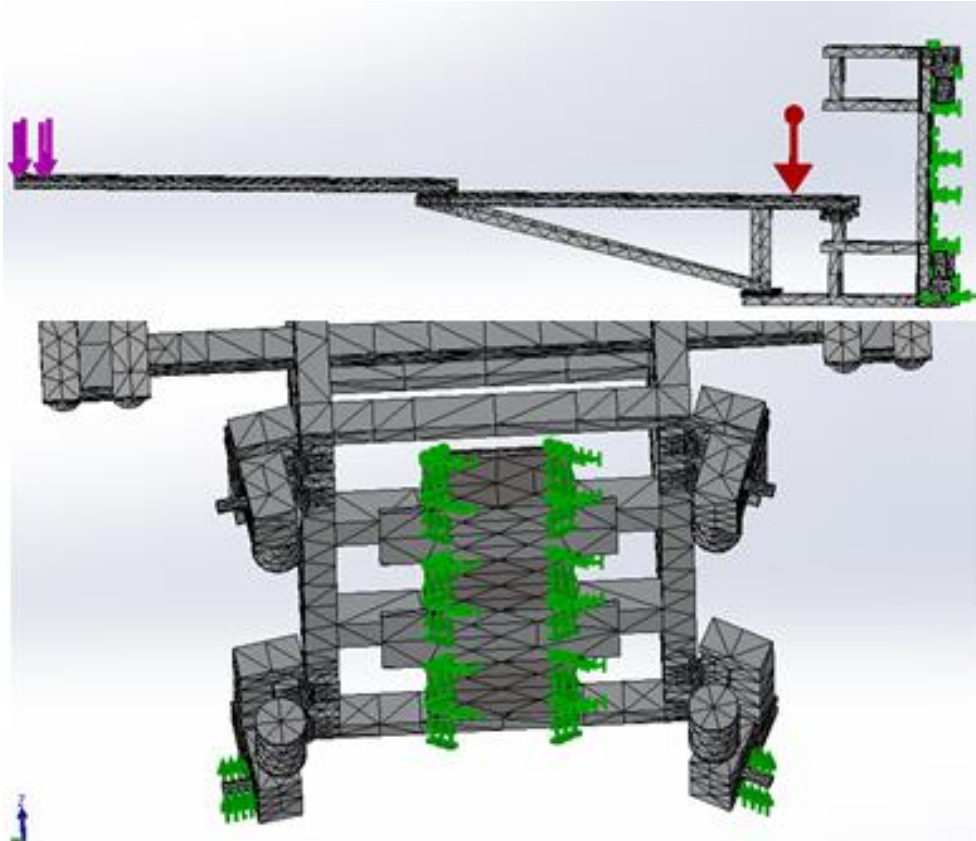
Figure 5.14 Fixed restraint at the magnets, bottom wheels, the applied load at the end of the arm and gravitational force (red arrow).

5.7.6. Applying loads

There is a wide range of mechanical loads that can be applied to points, curves, surfaces, and volumes. The type of mechanical loading applied to the robot is a force (Resultant force of 500 N) at the end of each arm representing the weight of the inspection tool. It is illustrated in pink colour as shown in Figure 5.14. Another type of load is applied to the robot which is the gravity force and is illustrated in red colour in Figure 5.14. The gravitational force is applied against the direction of the climbing motion of the robot on the tower.

5.7.7. Run of the study

In order to run the study, a solver should be chosen in SolidWorks software. There are three direct solvers and one iterative solver for the solution of the set of equations.

In the finite element analysis, a problem is represented by a set of algebraic equations that must be solved simultaneously. There are two classes of solution methods: direct and iterative.

Direct methods solve the equations using exact numerical techniques. Iterative methods solve the equations using approximate techniques. In each iteration, a solution is assumed, and the associated errors are evaluated. The iterations continue until the errors become acceptable.

5.8. Study results

5.8.1. von Mises stress

The maximum von Mises stress obtained was approximately 361 MPa which occurred at the hinge of the bottom wheel as shown in Figure 5.15. This value has been found to be below the yield strength of the hinge material which is alloy steel with yield value 620 MPa.

Figure 5.15 von Mises stress

5.8.2. Resultant displacement

The maximum resultant displacement obtained was 122.5 mm which occurred at the end of the arm as shown in Figure 5.16. Where this value has been found to be negligible since the length of the arm is 10 m.

Model name:Robot aluminum profile test 4
Study name:Static 1(-Default-)
Plot type: Static displacement Displacement1
Deformation scale: 1

URES (mm)
1.225e+002
1.123e+002
1.021e+002
9.185e+001
8.164e+001
7.144e+001
6.123e+001
5.103e+001
4.082e+001
3.062e+001
2.041e+001
1.021e+001
1.000e-030
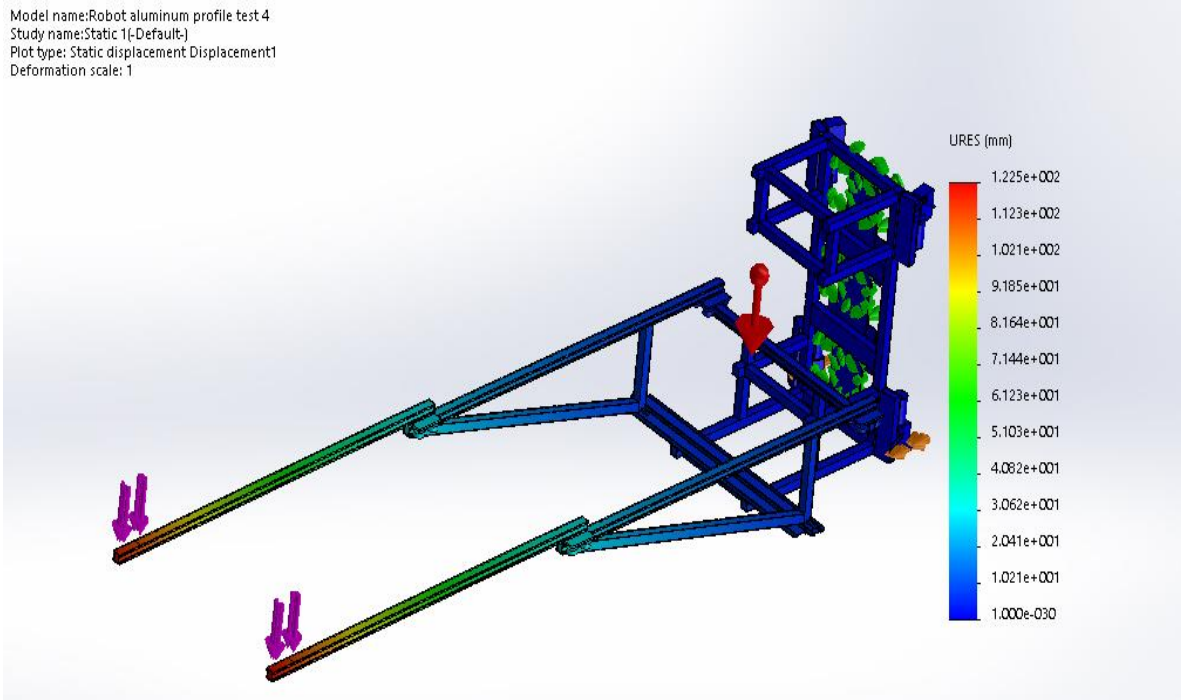
Figure 5.16 Resultant displacement

5.8.3. Factor of safety

The minimum factor of safety has been found to be of 1.48 as shown in Figure 5.17 which indicated the reliability and the integrity of the robot against static loading.

Model name:Robot aluminum profile test 4
Study name:Static 1(-Default-)
Plot type: Factor of Safety Factor of Safety1
Criterion : Automatic
Red < FOS = 1 < Blue
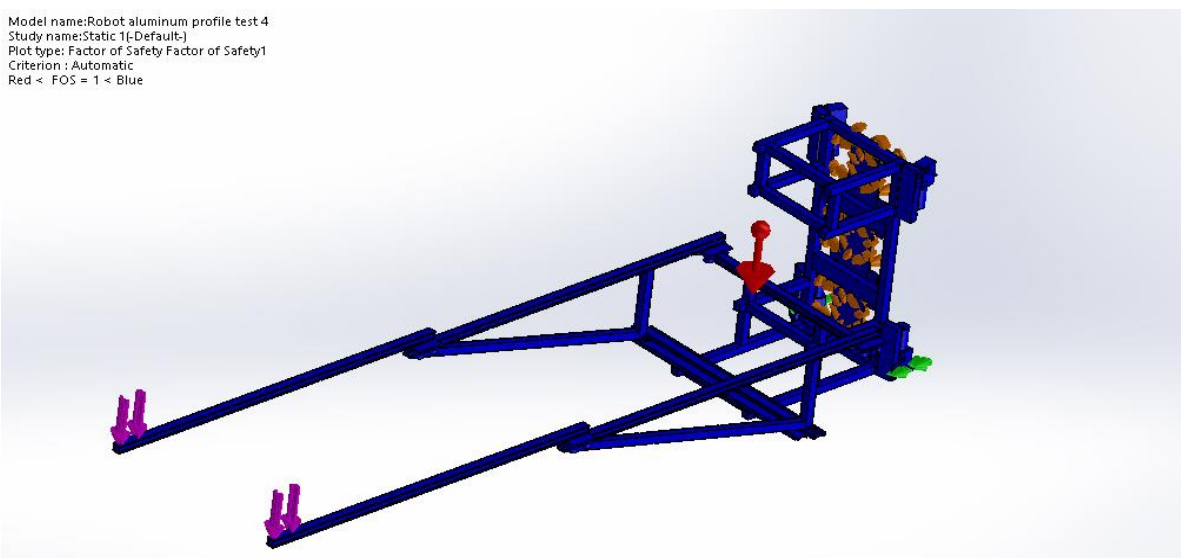
Figure 5.17 Factor of safety

5.9.   Flow simulation

A flow simulation has been carried out to study the effect of wind speed on the climbing robot when climbing the wind turbine tower while inspecting the blades. There are two types of flow

simulation studies. These are external flow and internal flow studies. The external flow studies are concerned about the flows while not bounded by outer surfaces; it concerns itself only with the fluid domain boundaries. In this case, the solid part is surrounded by the flow. It is related to the studies of aerodynamics. Internal flow studies concern themselves with the flow bounded by outer solid surfaces. In this case, the fluid is circulating inside a part such as a pipe or a valve. External flow studies have been chosen to simulate the working environment of the climbing robot.

In order to carry out the external flow simulation, a 3D computational domain has been created around the robot as shown in Figure 5.18. The fluid chosen for the simulation is air and the flow types are laminar to turbulent. Also, from the physics features, the gravitational force has been chosen in the x-direction as shown in Figure 5.14. The velocity direction of the air has been chosen to be a side wind (y-direction as shown in Figure 5.18) acting on the robot. It is the most effective wind on the robot while climbing and acts as a flow trajectory as shown in Figure 5.19.
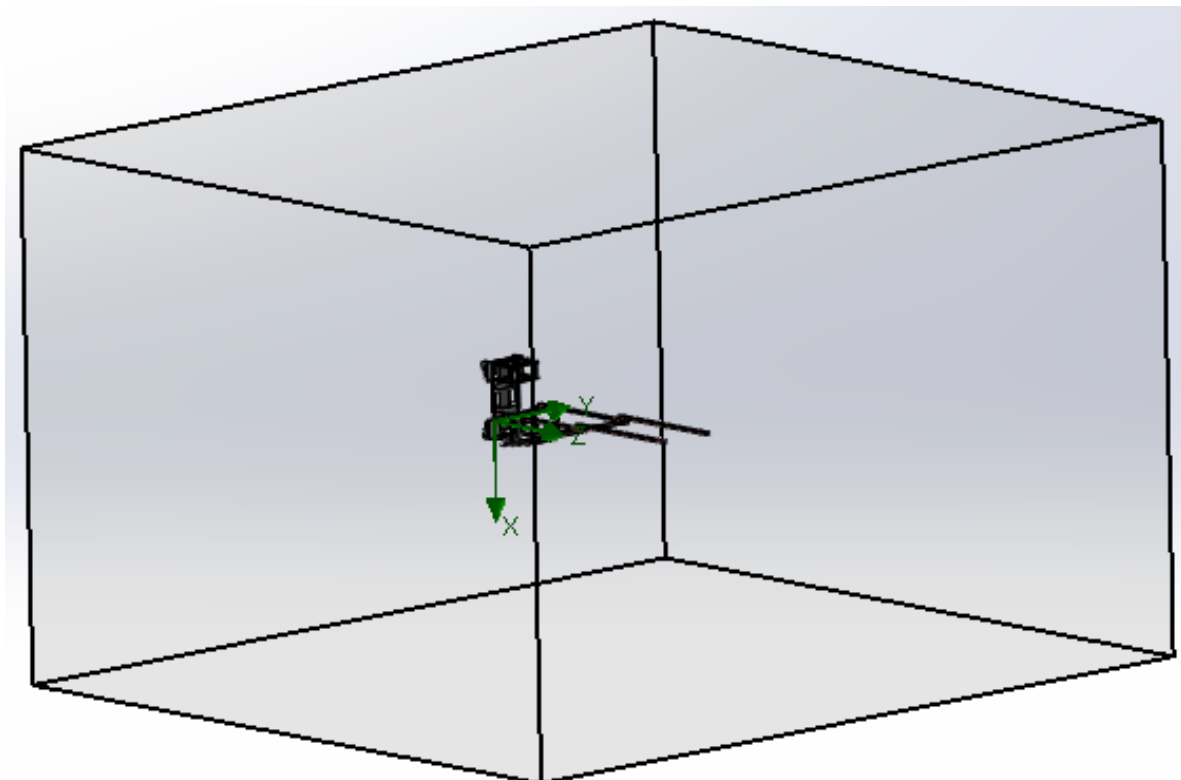
Figure 5.18 3D computational domain
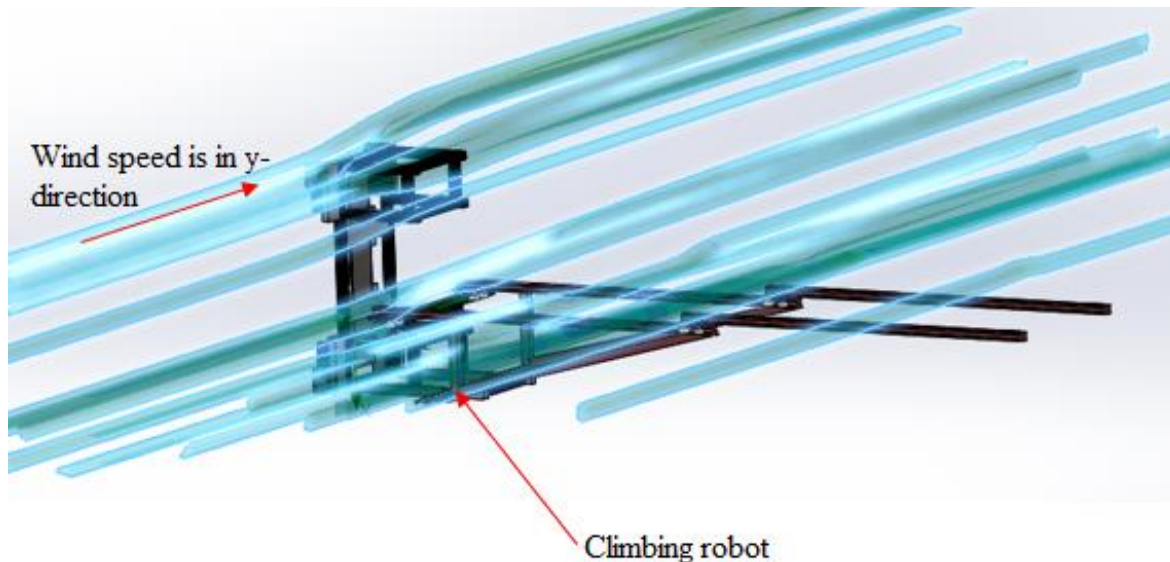
Figure 5.19 Wind flow trajectory

A parametric study was carried out to study the effect of wind on the robot at two different temperatures, namely 20 and 30 ºC and four different wind speed, namely 20 m/s, 22 m/s, 24 m/s and 26 m/s. The temperature was selected based on the average UK temperature [102]. The wind speed was selected based on the maximum wind speed value found in European wind atlas and taking relevant safety factors into account to test the extreme conditions that the robot might be subjected to during the inspection process [103]. Eight design points have been created based on the two degrees of temperature and four wind speeds as shown in Table 5.5 and Table 5.6. The highest dynamic pressure has been calculated to be 405.7 Pa which resulted in design point 4.

The flow simulation results of design point 4 have been combined with the stress analysis simulation where the flow simulation is applied as an initial state.

Table 5.5 Flow simulation results under different wind velocities at 20 degrees Celsius

	Design Point 1	Design Point 2	Design Point 3	Design Point 4
Temperature [°C]	20	20	20	20
Velocity in Y direction [m/s]	20	22	24	26
Dynamic Pressure [Pa]	240.1	290.5	345.7	405.7

Table 5.6 Flow simulation results under different wind velocities at 30 degrees Celsius

	Design Point 5	Design Point 6	Design Point 7	Design Point 8
Temperature [°C]	30	30	30	30
Velocity in Y direction [m/s]	20	22	24	26
Dynamic Pressure [Pa]	232.2	280.9	334.3	392.3

5.10. Combined static and flow study loading

5.10.1. von Mises Stress

The maximum von Mises stress obtained was approximately 3.73 MPa which occurred at the hinge of the bottom wheel as shown in Figure 5.20. This value has been found to be below the yield strength of the hinge material which is alloy steel with yield value 620 MPa.
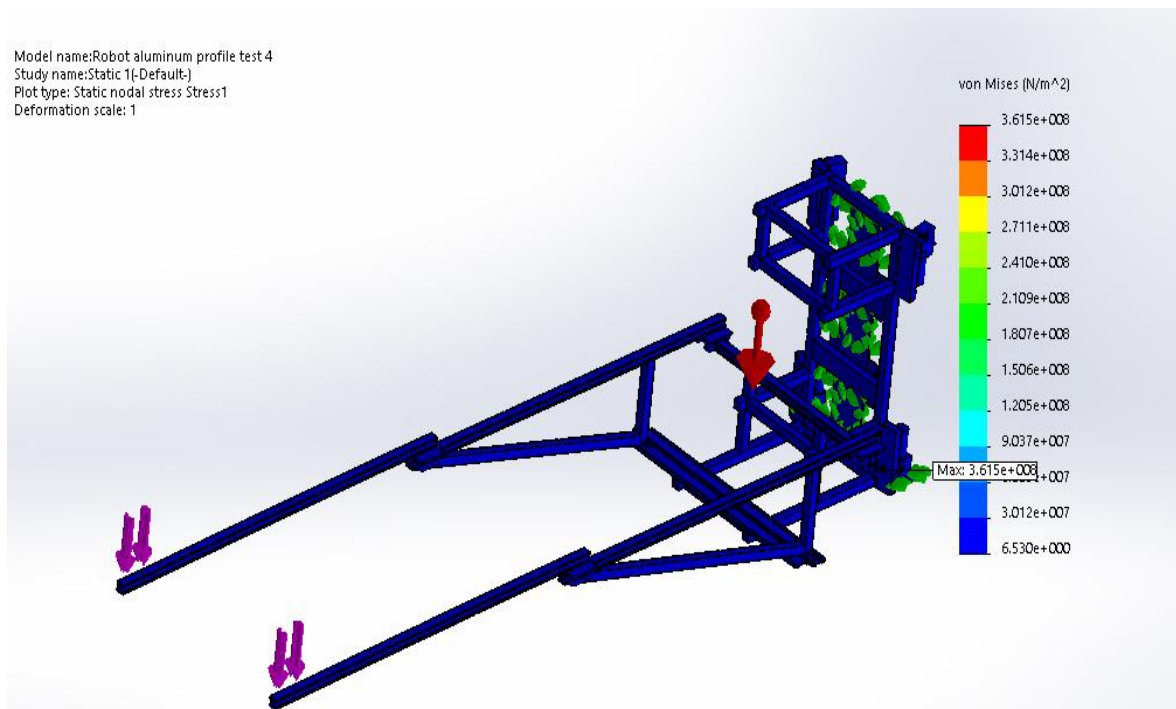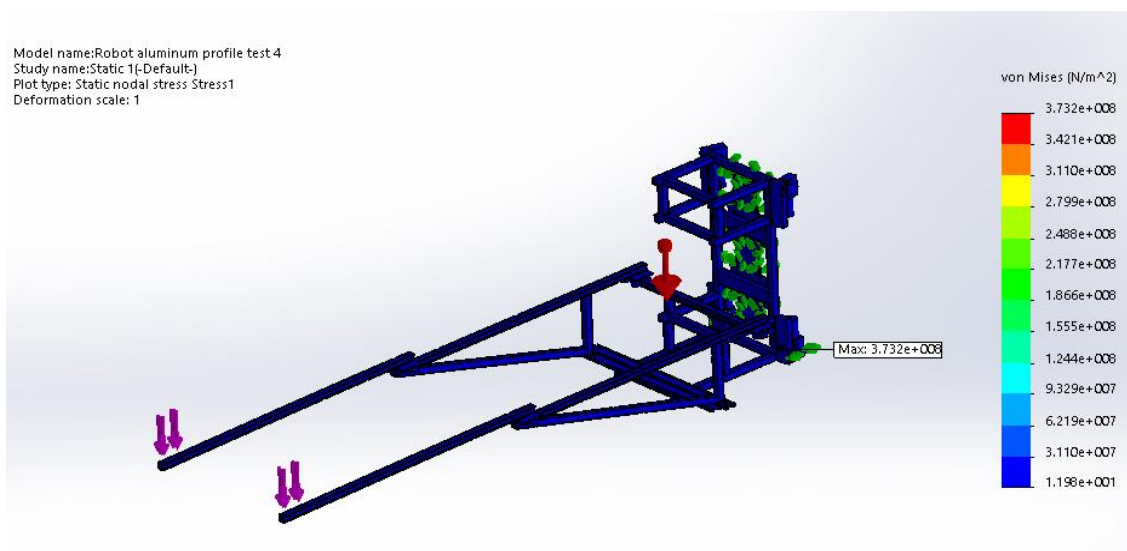

Figure 5.20 von Mises stresses under combined static and flow study

5.10.2. Resultant displacement

The maximum resultant displacement obtained was 123.4 mm which occurred at the end of the arm as shown in Figure 5.21. The pressure of the wind does not affect the resultant displacement, where it increases by only 1 mm compared to the static study and this value has been found to be negligible since the length of the arm is 10 m.
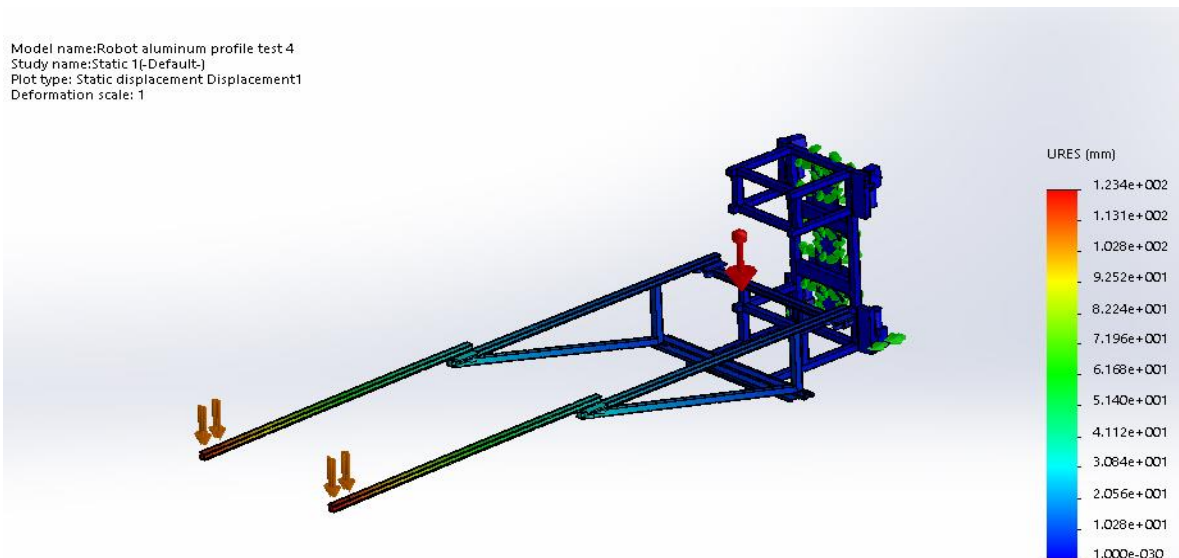
Figure 5.21 Resultant displacement under combined static and flow study

5.10.3. Resultant displacement in wind direction

The maximum resultant displacement obtained was 1.922 mm as shown in Figure 5.22. This value has been found to be negligible since the length of the arm is 10 m.
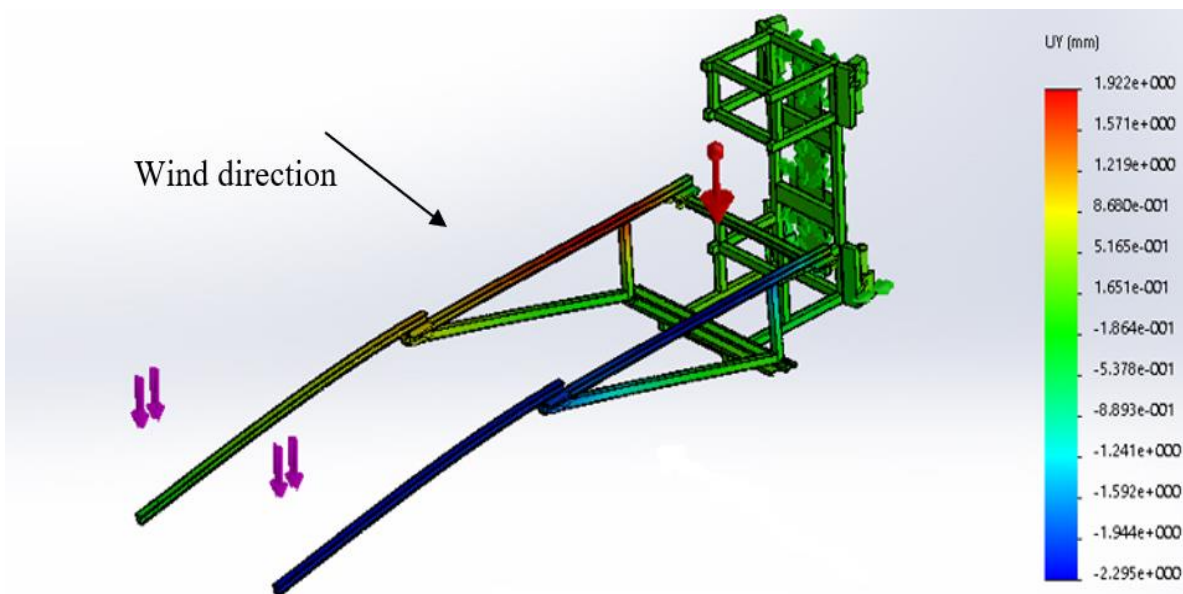
Figure 5.22 Resultant displacement in wind direction

5.10.4. Factor of safety

The safety factor expresses how much stronger a system is than it needs to be for an intended load. The minimum factor of safety has been found to be of 1.439 at the hinge as shown in Figure 5.23 which indicated the reliability and the integrity of the robot against combined static and flow study static loading.

Model name:Robot aluminum profile test 4
Study name:Static 1(-Default-)
Plot type: Factor of Safety Factor of Safety1
Criterion : Automatic
Red < FOS = 1 < Blue

Min: 1.439e+000
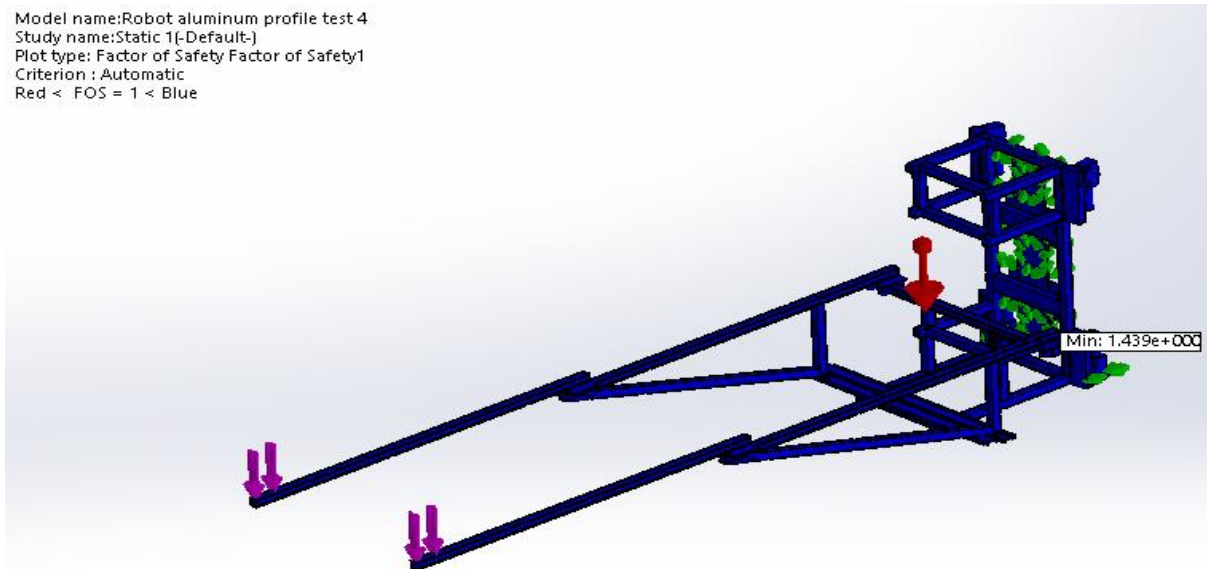
Figure 5.23 Factor of safety

5.11. Scale-up of the adhesion system

5.11.1. Results of the reaction force of the robot

Scaling up the magnetic adhesion system was based on the reaction force required to carry the robot with the inspection tools. This reaction force has been calculated using SolidWorks and is based on the previous stress analysis with flow simulation where the reaction forces required to achieve equilibrium are listed in Table 5.7.

Table 5.7 Reaction force required to achieve equilibrium to the climbing robot

Components	X	Y	Z	Resultant
Reaction force(N)	-14767.4	-145.311	-30359.4	33760.8

The reaction force in the x-direction is the direction of climbing the wind turbine tower as shown in Figure 5.24 where the reaction value is negative as it is against the gravity direction. While the y-direction is the direction of the wind and the z-direction is in the horizontal direction.
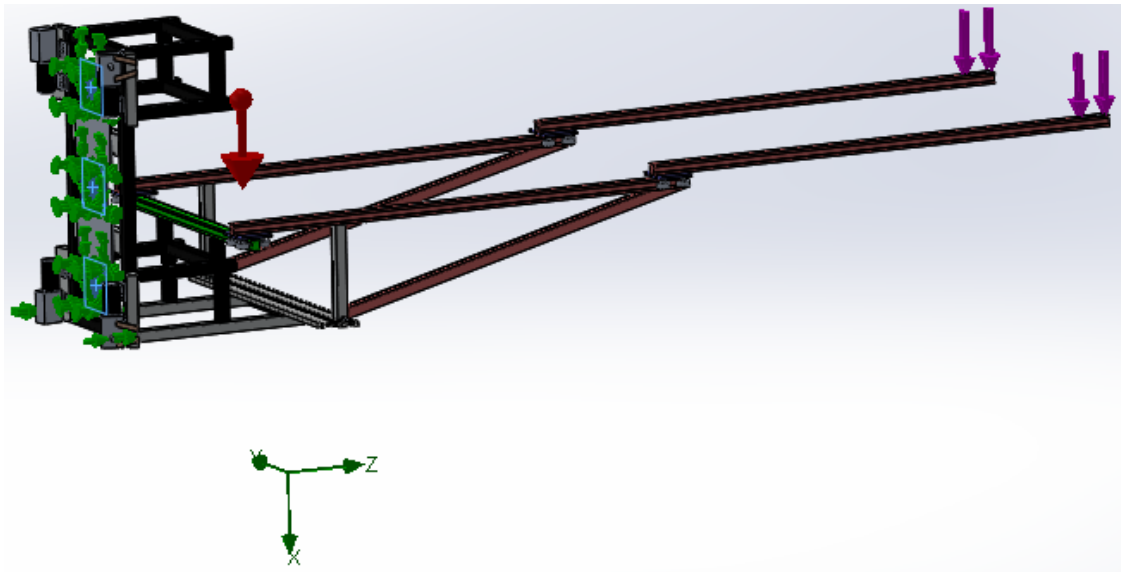
Figure 5.24 Reaction forces in the direction of climbing X-direction

5.11.2. Magnetic adhesion scale-up system

5.11.2.1. Model geometry

The scale-up magnetic adhesion system of the wall climbing robot model is based on the model described previously in chapter 3 where it consists of three parts. The first part is the wind turbine tower which is modelled with dimension 5.8 m in diameter and 5 m height as shown in Figure 5.25. The dimension of the tower is modelled based on the tower modelled previously described in this chapter. The other two parts are the neodymium magnets N52 with dimension $50 \times 50 \times 12.5$ mm and a yoke with length 2450 mm, width 250 mm and thickness 10 mm. The magnets are arranged in the form of a matrix 5×25 as shown in Figure 5.26. The distance (air gap) between the tower and the magnets is 10 mm in the middle. The model is enclosed by a simulation box volume where the dimensions are chosen large enough, with respect to the model volume. The dimension of the box is $20 \times 20 \times 15$ m as shown in Figure 5.27.
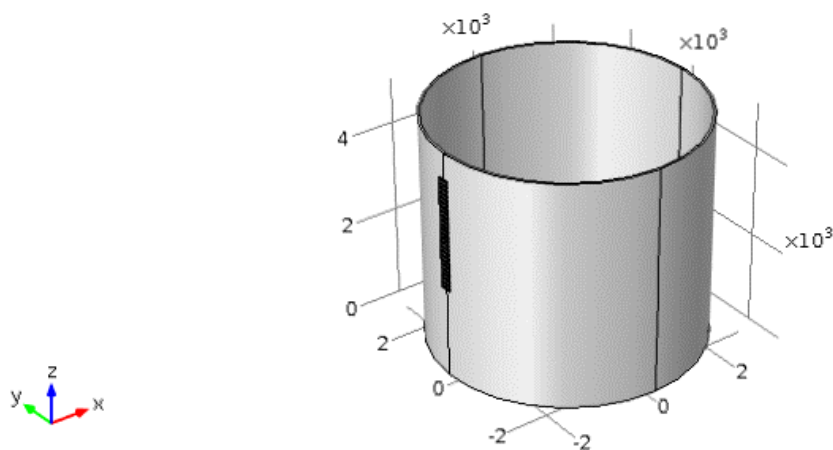
Figure 5.25 COMSOL scale-up model
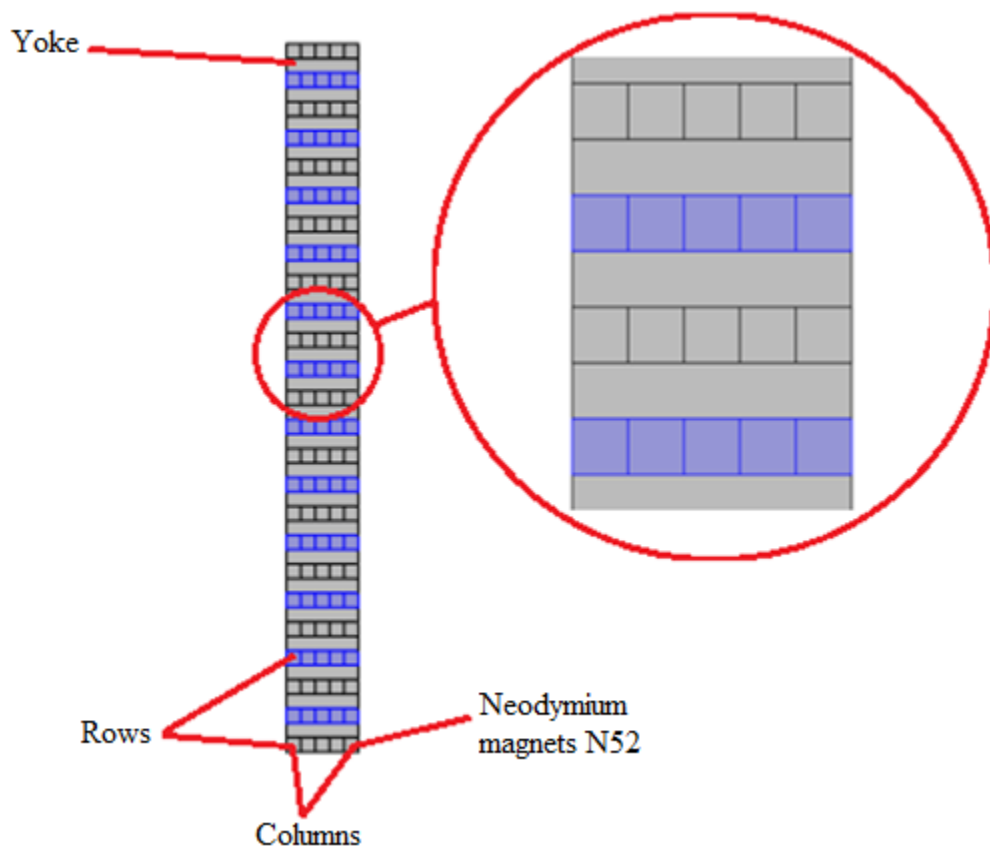
Figure 5.26 Magnets arrangements
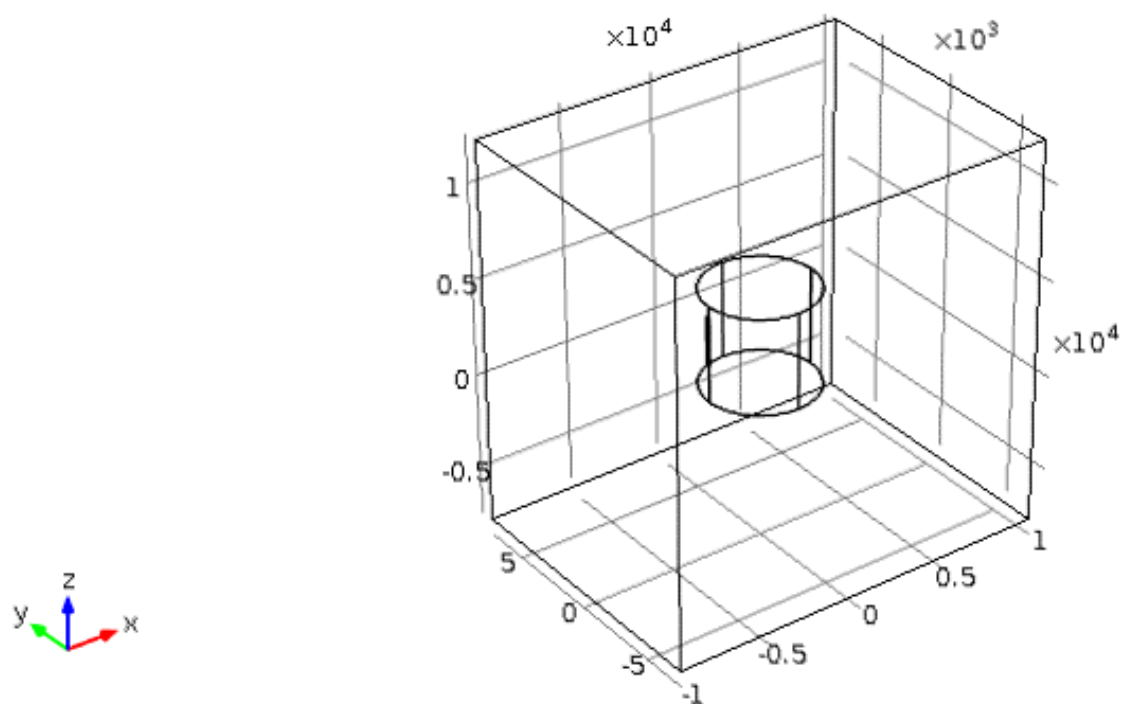
Figure 5.27 Simulation box volume

5.11.2.2. Defining the material for the geometry

The material assigned to the tower and the yoke is iron and the material assigned to the simulation volume is air.

5.11.2.3. Applying physics

A magnetic flux conversion has been applied to the three rectangular part attached to the yoke representing the magnets as shown in Figure 5.26. Where the Residual Flux Density (**Br**) is given by:

$$B_r = \mu_0 \mu_r M \qquad\qquad (5.1)$$

Where μ_r is the relative permeability of the neodymium magnet which is equal to 1.05. The (**B$_r$**) is assigned in the x-direction with the values listed in Table 5.8.

Table 5.8 Residual flux density across the 3 axes

Residual Flux Density (B$_r$) [T]	Direction
1.43	X
0	Y
0	Z

The polarity of the neodymium magnet is chosen to be alternating by rows through assigning a positive and negative residual flux density respectively. Reflecting this on the current model the middle magnet, shown in Figure 5.26, has been assigned a different polarity, negative residual flux density, with respect to the other two magnets. The magnetic adhesion force achieved from the scaled-up model is 50,017 N which exceeds the reaction force concluded form the static and flow simulation. This means that the scale-up adhesion mechanism is capable of carrying the robot with its inspection tools.

5.12. Chapter summary

This chapter presents the methodology of scaling up all the components of the climbing robot taking into consideration the dimension of a real wind turbine. An offshore wind turbine has been modelled with a height of 100 m where its dimensions are used for scaling up the prototype robot. A compensation has been made between the length and cross-section of the robot chassis to obtain a reasonable weight of the robot which is 1135 kg. Static stress analysis

and a flow simulation have been performed to check the durability and the stability of the robot frame especially of the two arms for carrying the inspection tool. The maximum resultant displacement obtained was 123.4 mm at a load of 50 kg on each arm. The resultant force obtained from the stress analysis and flow simulation required to keep the robot in static equilibrium was 33760.8 N. Accordingly, the magnetic adhesion system has been scaled up to achieve robot equilibrium where an adhesion force of 50,017 N has been achieved with COMSOL Multiphysics analysis.

Chapter 6
Conclusions and future work

6.1.   Summary and conclusions

The aim of this study was to optimise the payload carrying capacity of a wall climbing robot designed for wind blade inspection. Consequently, a literature review on the wall climbing robots has been carried out followed by a review of the NDT techniques used for inspecting wind turbine blades. A scaled-down robot prototype has been developed to test the feasibility of carrying long deployment arms and inspection sensors to wind turbine blades while adhering to steel towers using permanent magnets. The study aimed to optimise the payload carrying capability of the robot by using permanent magnet adhesion to attach to the wind turbine tower. Based on the numerical finite element method model, it has been observed that a 12 mm air gap is needed to remain attached to the tower. Furthermore, an inspection tool of up to one kilogram in each arm can be added to inspect the wind turbine blade while keeping the climbing robot in stable equilibrium.

RSM has been used to optimise the magnetic adhesion force for the wall climbing robot prototype. A quadratic polynomial model has been obtained for the magnetic adhesion force function in all factors affect the magnetic adhesion force. Optimum conditions have been concluded from the quadratic polynomial model for adhesion force of 235.4 N at 21.7 mm distance between magnets, 18 mm air gap and 7.79 mm for yoke thickness. Experimental and statistical validation has been applied for the predicted model resulting in a high agreement in the results. The average relative error between the tested experimental values and predicted values using the quadratic polynomial model is 0.95%.

Experiments with the scaled-down robot prototype were performed to validate the numerical model.

 A scaled-up robot has been presented with the capability of carrying payload up to 500 N on each arm. A static and flow simulation has been carried out resulting in maximum von Mises stress 3.73 MPa which occurred at the hinge of the wheel where this value has been found to be below the yield strength of the hinge material which is alloy steel with yield value 620 MPa. The maximum deflection of the arm under the payload and wind effect has been found to be 123 mm. The minimum factor of safety for the robot has been found to be 1.439.

In a conclusion, the main findings of this work could be summarised as follows:

- By surveying the different types of wall climbing robots, it was observed that the magnetic adhesion principle is the most appropriate technique for the case study under test.

- A comprehensive study of various nondestructive techniques has been carried out in this study showing that X-ray and ultrasonic inspection are recommended for blade inspection. However, ultrasonic inspection is more suitable than X-ray regarding the inspection tool weight.

- A polynomial regression model based on the experimental results has been developed representing the response variable, magnetic adhesion force, as a function of different independent variables such as air gap, the distance between magnets and yoke thickness.

- The developed RSM model has been validated using ANOVA which resulted in a high statistical significance to the experimental data.

- Numerical optimisation has been performed for maximising the adhesion force while minimising the process variables.

- A scaled-down robot prototype has been developed as a test and verification platform for the developed NDT approach.

- The climbing robot has been equipped with two arms with two degrees of freedom to trace the wind turbine blade profile during the inspection.

- A wind turbine has been modelled with typical medium-size dimensions (Siemens SWT-6-154) to assess the scaled-up robot.

- The first robot design has been scaled up to determine the size, weight, materials and adhesion force required to remain stable while operating on a medium-size WT. Static stress and flow analysis has been performed on this design to study the effect of wind (20-26m/s), temperature (20-30°C), a 50 kg load acting at the end of each robot arm, materials of construction (aluminium), and the bending of the two ten metre long arms. The design will be able to remain stable with maximum displacement at the tip of the 10 m long of 123 mm while carrying a maximum load of 50 kg at the end of each arm. The robot will require an adhesion force of 33,760 N which is easily exceeded by the proposed magnetic system which generates a force of 50, 017 N.

6.2. Recommendations for future work

By observing the simulation and the experimental results the following points are considered as future work:

- Different materials could be investigated with the same yield strength of aluminium or higher and less density in order to reduce the total weight of the robot.
- The shape of the bars used in the chassis of the robot can be modified to reduce the effect of air resistance on the robot.
- The vibration in 3 dimensions of a stopped blade has not been considered in this study. Due to the vibration of the blade, the arm of the robot should be modified with a compliant mechanism to grab the blade with both arms and let passive compliance move the inspection sensor (e.g. X-ray source/detector) along with the blade while our robot on the tower remains stationary.
- Since ultimately, the purpose of developing a robot that climbs wind towers is to perform NDT of WTBs, an appropriate inspection tool should be added to the proposed climbing robot to study the effectiveness of robotic NDT in detecting the various types of cracks in wind turbine blades.
- Implementing a real model of the full-scale climbing robot and testing with a real wind turbine. The feasibility of the real climbing robot could be compared with the simulation study for the future development of the inspecting climbing robot.
- The robot can carry out the inspection process, however, there are numerous improvements required for the current system regarding the intelligence of the control algorithm. A machine learning algorithm can be added to speed up the process of inspection in which the robot can learn from the previous inspections.
- A localisation algorithm could be investigated with 3D mapping for the blade so the inspecting arm can locate the defects in the WTB during the inspection. These data can be used by the inspectors for conditional assessment of the WTB. Moreover, it might be useful for the repairing plan process in the future.
- As the WTs are working in harsh environments the blades are affected with dirt and dust. This dirt and dust might be misleading in the images taken during the inspection so cleaning system could be equipped with the inspection system.
- In spite of the robot's capability in inspecting the WTB it is not a replacement for the highly skilled workers required for the maintenance process of the WTB. Accordingly,

to protect the workers from the risk that they might face during the maintenance of WTB; more research is required on the maintenance tools and how it could be integrated with the robot.

References

1. Lal, R., *Feeding 11 billion on 0.5 billion hectare of area under cereal crops.* Food and Energy Security, 2016. **5**(4): p. 239-251.

2. Sadorsky, P., *The impact of financial development on energy consumption in emerging economies.* Energy policy, 2010. **38**(5): p. 2528-2535.

3. Berardi, U., *A cross-country comparison of the building energy consumptions and their trends.* Resources, Conservation and Recycling, 2017. **123**: p. 230-241.

4. McKendry, P., *Energy production from biomass (part 1): overview of biomass.* Bioresource technology, 2002. **83**(1): p. 37-46.

5. Yüksel, I., *Hydropower for sustainable water and energy development.* Renewable and Sustainable Energy Reviews, 2010. **14**(1): p. 462-469.

6. Singh, G.K., *Solar power generation by PV (photovoltaic) technology: A review.* Energy, 2013. **53**: p. 1-13.

7. Mellit, A. and S.A. Kalogirou, *Artificial intelligence techniques for photovoltaic applications: A review.* Progress in energy and combustion science, 2008. **34**(5): p. 574-632.

8. Müller-Steinhagen, H. and F. Trieb, *Concentrating solar power.* A review of the technology. Ingenia Inform QR Acad Eng, 2004. **18**: p. 43-50.

9. Kaygusuz, K., *Wind power for a clean and sustainable energy future.* Energy Sources, Part B, 2009. **4**(1): p. 122-133.

10. Sunak, Y. and R. Madlener, *Local impacts of wind farms on property values: a spatial difference-in-differences analysis.* 2014.

11. Márquez, F.P.G., et al., *Condition monitoring of wind turbines: Techniques and methods.* Renewable Energy, 2012. **46**: p. 169-178.

12. Newman, M., *Operations and maintenance in offshore wind: key issues for 2015/16.* 2015.

13. Leung, D.Y. and Y. Yang, *Wind energy development and its environmental impact: A review.* Renewable and sustainable energy reviews, 2012. **16**(1): p. 1031-1039.

14. Jüngert, A., *Damage Detection in wind turbine blades using two different acoustic techniques.* The NDT Database & Journal (NDT), 2008.

15. Lattanzi, D. and G. Miller, *Review of robotic infrastructure inspection systems.* Journal of Infrastructure Systems, 2017. **23**(3): p. 04017004.

16. Indri, M., A. Grau, and M. Ruderman, *Guest editorial special section on recent trends and developments in industry 4.0 motivated robotic solutions.* IEEE Transactions on Industrial Informatics, 2018. **14**(4): p. 1677-1680.

17. Mineo, C., et al. *Enabling robotic adaptive behaviour capabilities for new industry 4.0 automated quality inspection paradigms.* in *57th Annual British Conference on Non-Destructive Testing.* 2018.

18. Chu, B., et al., *A survey of climbing robots: Locomotion and adhesion.* International journal of precision engineering and manufacturing, 2010. **11**(4): p. 633-647.

19. Sattar, T.P., H. Leon Rodriguez, and B. Bridge, *Climbing ring robot for inspection of offshore wind turbines.* Industrial Robot: An International Journal, 2009. **36**(4): p. 326-330.

20. Elkmann, N., T. Felsch, and T. Förster, *Robot for rotor blade inspection*, in *1st International Conference on Applied Robotics for the Power Industry.* 2010, IEEE. p. 1-5.

21. Lim, S., et al., *The inchworm type blade inspection robot system*, in *9th International Conference on 9th International Conference on Ubiquitous Robots and Ambient Intelligence (URAI).* 2012, IEEE. p. 604-607.

22. Lee, D.G., S. Oh, and H.I. Son, *Maintenance robot for 5-MW offshore wind turbines and its control.* IEEE/ASME Transactions on Mechatronics, 2016. **21**(5): p. 2272-2283.

23. Jung, S., et al., *Mechanism and system design of MAV (Micro Aerial Vehicle)-type wall-climbing robot for inspection of wind blades and non-flat surfaces*, in *15th International Conference on Control, Automation and Systems (ICCAS).* 2015, IEEE. p. 1757-1761.

24. Grieco, J.C., et al. *A six-legged climbing robot for high payloads.* in *Control Applications, 1998. Proceedings of the 1998 IEEE International Conference on.* 1998. IEEE.

25. Hong, Q., et al. *Wall climbing robot enabled by a novel and robust vibration suction technology.* in *2009 IEEE International Conference on Automation and Logistics.* 2009. IEEE.

26. Sintov, A., T. Avramovich, and A. Shapiro, *Design and motion planning of an autonomous climbing robot with claws.* Robotics and Autonomous Systems, 2011. **59**(11): p. 1008-1019.

27. Fernández, R., et al. *A wall climbing robot for tank inspection. An autonomous prototype*. in *IECON 2010-36th Annual Conference on IEEE Industrial Electronics Society*. 2010. IEEE.

28. Tavakoli, M., et al., *OmniClimbers: Omni-directional magnetic wheeled climbing robots for inspection of ferromagnetic structures*. Robotics and Autonomous Systems, 2013. **61**(9): p. 997-1007.

29. Tavakoli, M., et al., *The hybrid OmniClimber robot: Wheel based climbing, arm based plane transition, and switchable magnet adhesion*. Mechatronics, 2016.

30. Zhang, H., W. Wang, and J. Zhang. *High stiffness pneumatic actuating scheme and improved position control strategy realization of a pneumatic climbing robot*. in *Robotics and Biomimetics, 2008. ROBIO 2008. IEEE International Conference on*. 2009. IEEE.

31. Madsen, O., et al., *Design of a climbing robot for inspecting aircraft wings and fuselage*. Industrial Robot: An International Journal, 2007. **34**(6): p. 495-502.

32. Faina, A., et al. *Development of a climbing robot for grit blasting operations in shipyards*. in *Robotics and Automation, 2009. ICRA'09. IEEE International Conference on*. 2009. IEEE.

33. Netland, Ø. and A. Skavhaug. *Prototyping and evaluation of a telerobot for remote inspection of offshore wind farms*. in *Applied Robotics for the Power Industry (CARPI), 2012 2nd International Conference on*. 2012. IEEE.

34. Elkmann, N., et al., *Kinematics, sensors and control of the fully automated facade-cleaning robot SIRIUSc for the Fraunhofer headquarters building, Munich*. Industrial Robot: An International Journal, 2008. **35**(3): p. 224-227.

35. Wang, W., et al., *Robotic cleaning system for glass facade of high-rise airport control tower*. Industrial Robot: An International Journal, 2010. **37**(5): p. 469-478.

36. Kawasaki, S. and K. Kikuchi. *Development of a small legged wall climbing robot with passive suction cups*. in *Proceedings of the 3rd International conference on design engineering and science–ICDES*. 2014.

37. Ge, D., et al., *Quantitative study on the attachment and detachment of a passive suction cup*. Vacuum, 2015. **116**: p. 13-20.

38. Bahr, B., Y. Li, and M. Najafi, *Design and suction cup analysis of a wall climbing robot*. Computers & electrical engineering, 1996. **22**(3): p. 193-209.

39. Wang, W., et al., *Principle and experiment of vibrating suction method for wall-climbing robot.* Vacuum, 2010. **85**(1): p. 107-112.

40. Lee, G., et al., *MultiTrack: A multi-linked track robot with suction adhesion for climbing and transition.* Robotics and Autonomous Systems, 2015. **72**: p. 207-216.

41. Cui, D., et al. *Design and analysis of climbing robot based on construction surface inspection*. in *Control and Decision Conference (CCDC), 2016 Chinese*. 2016. IEEE.

42. La Rosa, G., et al., *A low-cost lightweight climbing robot for the inspection of vertical surfaces.* Mechatronics, 2002. **12**(1): p. 71-96.

43. Longo, D. and G. Muscato, *A modular approach for the design of the Alicia3 climbing robot for industrial inspection.* Industrial Robot: An International Journal, 2004. **31**(2): p. 148-158.

44. Koo, I.M., et al., *Development of wall climbing robot system by using impeller type adhesion mechanism.* Journal of Intelligent & Robotic Systems, 2013. **72**(1): p. 57-72.

45. Haynes, G.C., et al., *Rapid pole climbing with a quadrupedal robot*, in *IEEE International Conference on Robotics and Automation, ICRA'09.* . 2009, IEEE. p. 2767-2772.

46. Tavakoli, M. and L. Marques, *3DCLIMBER: Climbing and manipulation over 3D structures.* Mechatronics, 2011. **21**(1): p. 48-62.

47. Provancher, W.R., S.I. Jensen-Segal, and M.A. Fehlberg, *ROCR: An energy-efficient dynamic wall-climbing robot.* IEEE/ASME Transactions on Mechatronics, 2011. **16**(5): p. 897-906.

48. Liu, R., et al., *Wall climbing robot using electrostatic adhesion force generated by flexible interdigital electrodes.* International Journal of advanced robotic systems, 2013. **10**.

49. Chen, R., et al. *A gecko inspired wall-climbing robot based on electrostatic adhesion mechanism*. in *Robotics and Biomimetics (ROBIO), 2013 IEEE International Conference on*. 2013. IEEE.

50. Seo, T. and M. Sitti. *Under-actuated tank-like climbing robot with various transitioning capabilities*. in *Robotics and Automation (ICRA), 2011 IEEE International Conference on*. 2011. IEEE.

51. Bridge, B., et al., *Development of a climbing robot for inspection of long weld lines.* Industrial Robot: An International Journal, 2008. **35**(3): p. 217-223.

52. SATTAR, T.P., P. HILTON, and O.F. HOWLADER, *Deployment of laser cutting head with wall climbing robot for nuclear decommissioning*, in *Advances in Cooperative Robotics*. 2017, World Scientific. p. 725-732.

53. Peters, G., et al. *A prototype climbing robot for inspection of complex ferrous structures*. in *13th International Conference on Climbing and Walking Robots and the Support Technologies for Mobile Machines (CLAWAR2010), Nagoya, Japan, Aug.* 2010.

54. MAEMPEL, J., et al., *Inspirat–Towards a biologically inspired climbing robot for the inspection of linear structures*, in *Advances in Mobile Robotics*. 2008, World Scientific. p. 206-213.

55. Bevly, D.M., S. Farritor, and S. Dubowsky. *Action module planning and its application to an experimental climbing robot*. in *Robotics and Automation, 2000. Proceedings. ICRA'00. IEEE International Conference on*. 2000. IEEE.

56. Spenko, M.J., et al., *Biologically inspired climbing with a hexapedal robot.* Journal of Field Robotics, 2008. **25**(4-5): p. 223-242.

57. Kim, S., et al. *SpinybotII: climbing hard walls with compliant microspines*. in *Advanced Robotics, 2005. ICAR'05. Proceedings., 12th International Conference on*. 2005. IEEE.

58. Birkmeyer, P., A.G. Gillies, and R.S. Fearing. *Dynamic climbing of near-vertical smooth surfaces*. in *Intelligent Robots and Systems (IROS), 2012 IEEE/RSJ International Conference on*. 2012. IEEE.

59. Cepolina, F., et al., *Roboclimber versus landslides: design and realization of a heavy-duty robot for teleoperated consolidation of rocky walls.* IEEE robotics & automation magazine, 2006. **13**(1): p. 23-31.

60. Nejadfard, A., H. Moradi, and M.N. Ahmadabadi. *A multi-robot system for dome inspection and maintenance: Concept and stability analysis*. in *Robotics and Biomimetics (ROBIO), 2011 IEEE International Conference on*. 2011. IEEE.

61. Chung, W.K., et al. *A novel design of movable gripper for non-enclosable truss climbing*. in *Robotics and Automation (ICRA), 2011 IEEE International Conference on*. 2011. IEEE.

62. Fauroux, J.-C. and J. MORILLON, *Design of a climbing robot for cylindro-conic poles based on rolling self-locking*, in *Mobile Robotics: Solutions and Challenges*. 2010, World Scientific. p. 447-454.

63.   Baghani, A., M.N. Ahmadabadi, and A. Harati. *Kinematics modeling of a wheel-based pole climbing robot (UT-PCR)*. in *Robotics and Automation, 2005. ICRA 2005. Proceedings of the 2005 IEEE International Conference on*. 2005. IEEE.

64.   Prahlad, H., et al. *Electroadhesive robots—wall climbing robots enabled by a novel, robust, and electrically controllable adhesion technology*. in *Robotics and Automation, 2008. ICRA 2008. IEEE International Conference on*. 2008. IEEE.

65.   Unver, O. and M. Sitti. *A miniature ceiling walking robot with flat tacky elastomeric footpads*. in *Robotics and Automation, 2009. ICRA'09. IEEE International Conference on*. 2009. IEEE.

66.   Daltorio, K.A., et al. *A small wall-walking robot with compliant, adhesive feet*. in *Intelligent Robots and Systems, 2005.(IROS 2005). 2005 IEEE/RSJ International Conference on*. 2005. IEEE.

67.   DashWin. *DashWin*. 2018, July 16; Available from: http://www.dashwin.eu/.

68.   WIspector. *WIspector project*. 2016; Available from: http://www.winspector.eu/.

69.   (RADBLAD), I.-s.X.-r.r.o.o.w.b. *RADBLAD*. 2019 24 July 2019; Available from: https://gtr.ukri.org/projects?ref=104076.

70.   Adaramola, M., *Wind turbine technology: Principles and design*. 2014: CRC Press.

71.   Barr, S.M. and J.W. Jaworski, *Optimization of tow-steered composite wind turbine blades for static aeroelastic performance.* Renewable energy, 2019. **139**: p. 859-872.

72.   Schubel, P.J. and R.J. Crossley, *Wind turbine blade design.* Energies, 2012. **5**(9): p. 3425-3449.

73.   Lamraoui, F., et al., *Atmospheric icing impact on wind turbine production.* Cold Regions Science and Technology, 2014. **100**: p. 36-49.

74.   Hancock, M., et al., *Rotor blade for a wind turbine and a method for making the same*. 2015, U.S. Patent No. 9,068,559.

75.   Bendel, U., et al., *Method for manufacturing a rotor blade of a wind power plant, rotor blade and wind power plant*. 2016, U.S. Patent Application 15/254,956.

76.   SANGUESA, M.Y., A.M. Babiano, and O.G. Miguel, *Ice-resistant paint for wind turbine blades, procedure for its preparation, use and wind turbine blade coated with the ice-resistant paint*. 2016, U.S. Patent Application 14/790,195.

77.   Jasinien, E., et al., *NDT of wind turbine blades using adapted ultrasonic and radiographic techniques.* Insight-Non-Destructive Testing and Condition Monitoring, 2009. **51**(9): p. 477-483.

78. Fiore, G., G.E. Fujiwara, and M.S. Selig. *A Damage Assessment for Wind Turbine Blades from Heavy Atmospheric Particles*. in *53rd AIAA Aerospace Sciences Meeting*. 2015.

79. Sareen, A., C.A. Sapre, and M.S. Selig, *Effects of leading edge erosion on wind turbine blade performance*. Wind Energy, 2014. **17**(10): p. 1531-1542.

80. Zhou, H., et al., *A review of full-scale structural testing of wind turbine blades*. Renewable and Sustainable Energy Reviews, 2014. **33**: p. 177-187.

81. Hornfeck, C., et al., *Comparative study of state of the art nondestructive testing methods with the local acoustic resonance spectroscopy to detect damages in GFRP*. Journal of Nondestructive Evaluation, 2015. **34**(2): p. 10.

82. Aly, F. and C.E. Semler, *Prediction of refractory strength using nondestructive sonic measurements*. AM. CERAM. SOC. BULL. Am. Ceram. Soc. Bull., 1985. **64**(12): p. 1555.

83. Tiwari, K.A., R. Raisutis, and V. Samaitis, *Signal processing methods to improve the Signal-to-noise ratio (SNR) in ultrasonic non-destructive testing of wind turbine blade*. Procedia Structural Integrity, 2017. **5**: p. 1184-1191.

84. Steinchen, W., et al., *Application of shearography to quality assurance*. Journal of materials processing technology, 1995. **52**(1): p. 141-150.

85. Zhu, Y.-K., et al., *A review of optical NDT technologies*. Sensors, 2011. **11**(8): p. 7773-7798.

86. Gieske, J., et al. *Nondestructive evaluation (NDE) of composite/metal bond interface of a wind turbine blade uskng an acousto-ultrasonic technique*. in *35th Aerospace Sciences Meeting and Exhibit*. 1997.

87. Gan, T.-H., et al., *An Automated Ultrasonic NDT System for In-Situ Inspection of Wind Turbine Blades*. Journal of Mechanics Engineering and Automation, 2014. **4**(10).

88. Raišutis, R., E. Jasiūnienė, and E. Žukauskas, *Ultrasonic NDT of wind turbine blades using guided waves*. Ultrasound. ISSN1392-2114. Kaunas: Technologija, 2008. **63**(1): p. 7-11.

89. Anne JUENGERT, C.U.G. *Inspection techniques for wind turbine blades using ultrasound and sound waves*. in *The International Symposium on Nondestructive Testing in Civil Engineering*. 2009. Nantes, France.

90. Raišutis, R., et al., *The review of non-destructive testing techniques suitable for inspection of the wind turbine blades*. Ultragarsas (ultrasound), 2008. **63**(1): p. 26-30.

91. Jasiūnienė, E., et al., *Ultrasonic NDT of wind turbine blades using contact pulse-echo immersion testing with moving water container.* Ultrasound, 2008. **63**(3).

92. Amenabar, I., et al., *Comparison and analysis of non-destructive testing techniques suitable for delamination inspection in wind turbine blades.* Composites Part B: Engineering, 2011. **42**(5): p. 1298-1305.

93. Qi, G., et al. *Laser Shearography Testing for Aircraft Composite and Honeycomb Components*. in *Proceedings of the First Symposium on Aviation Maintenance and Management-Volume I*. 2014. Springer.

94. Gryzagoridis, J. and D. Findeis, *Impact damage detection on composites using optical NDT techniques.* Insight-Non-Destructive Testing and Condition Monitoring, 2010. **52**(5): p. 248-251.

95. Multiphysics, C. *Permanent magnet*. 2019 [cited 2019; Available from: https://www.comsol.com/model/permanent-magnet-78.

96. Pyrhonen, J., T. Jokinen, and V. Hrabovcova, *Design of rotating electrical machines*. 2013: John Wiley & Sons.

97. Materials, T.P.a.C.P.o.S.M.

98. Ferreira, S.C., et al., *Box-Behnken design: an alternative for the optimization of analytical methods.* Analytica chimica acta, 2007. **597**(2): p. 179-186.

99. Kempthorne, O., *The design and analysis of experiments.* 1952.

100. Einav, S. and M. O'Connor, *P-values and significance: The null hypothesis that they are not related is correct.* Journal of critical care, 2019. **54**: p. 159-162.

101. Energy, G.R. *GE Renewable Energy*. 2019; Available from: https://www.ge.com/renewableenergy/wind-energy/offshore-wind/haliade-x-offshore-turbine.

102. *UK beats winter temperature record again*. 26 February 2019; Available from: https://www.bbc.co.uk/news/uk-47374936.

103. Troen, I. and E.L. Petersen, *European wind atlas*. 1989: Risø National Laboratory.